Buoyancy driven flows in heterogeneous porous media

by

Bharath S. P. Kattemalalawadi

A thesis submitted in partial fulfillment of the requirements for the degree of

Doctor of Philosophy

Department of Mechanical Engineering
University of Alberta

Abstract

To improve the confidence of subsurface storage of fluids such as carbon-dioxide, acid-gas and hydrogen at various geological sites, a proper fluid dynamic understanding of flow phenomena occurring because of injecting these source fluids into a porous medium is necessary. While many advancements have been made in predicting the fluid flows in a uniform porous medium, the flow dynamics inside a non-uniform porous media remains less well understood. In this Thesis, we use theory, numerical simulations and experiments to clarify the fluid mechanics of injecting a source fluid into a saturated, multi-layered porous media in which each of the adjacent layers are separated by a sharp permeability jump. Throughout this study, we have considered small density differences between the source and ambient fluids (satisfying the Boussinesq approximation) and both these fluids are completely miscible with each other. The goal of the study is to inform three practical questions.

The first research component is to predict the early-time spreading dynamics of plume fluid striking an inclined permeability jump, within porous media having upper- and lower-layers of comparable thicknesses. The plume fluid, upon striking a permeability jump, results in a pair of oppositely directed gravity currents propagating along slope in the up- and downdip directions. To address the flow dynamics along an inclined permeable boundary, we develop a theoretical model in which we derive coupled non-linear partial differential equations describing gravity currents propagating along slope and their draining into the lower layer. The model predicts flow dynamics at both transient- and steady-state conditions. We further validate this model with similitude laboratory experiments. Experimental images show that the interface of the flow front is blurred due to hydrodynamics dispersion, and hence is not especially sharp. The implications of this observation vis-à-vis theoretical model assumptions are discussed.

The second research component is to study the effect of impermeable bottom and sidewall boundaries on the dynamics of the injected fluid. For this, we construct a two-layered porous medium inside a rectangular box and conduct experiments for various combinations of the source condition, permeability jump angle and layer depth. The experiments reveal the formation of two pairs of gravity currents, one in the upper layer (propagating along the permeability jump), and the second in the lower layer (propagating along the bottom boundary of the box). The dynamical influence of one gravity current upon the other, such as the occurrence of runout-override and remobilization from a state of runout, is investigated. At later instants in time, the gravity current flows are impeded due to the vertical sidewall boundaries which allows us to distinguish between two qualitatively different filling regimes, i.e. sequential vs. simultaneous filling of the upper- and lower-layers. Furthermore, parameter combinations conducive to one or the other filling regime are also identified.

The third research component regards to the flow pattern inside a more complicated multi-layered porous medium, i.e. consisting of up to five layers. For this we derive steady analytical solutions for the gravity currents formed along each of the permeability jump boundaries. The model predicts the outer envelope of the flow pattern corresponding to steady flow conditions. Finite-element based COMSOL simulations are also performed for different combinations of layer permeabilities and also by changing the permeability jump angles. The comparison of outer envelope with the theory shows good agreement. Also, the impact of adding intermediate layers of different permeabilities on the maximum span of runout and storage areas are investigated.

Preface

This thesis is an original work by Bharath S. Kattemalalawadi. The mathematical formulations of Chapters 2 and 4 are derived by myself, with the assistance of Prof. M. R. Flynn. Moreover, the experimental setups presented in Chapters 2 and 3 were designed by myself, with the assistance of Prof. M. R. Flynn, Dr. C. K. Sahu and University of Alberta, Department of Mechanical Engineering Technical Resources Group.

Chapter 2 of this thesis has been published as K. S. Bharath, C. K. Sahu and M. R. Flynn, "Isolated buoyant convection in a two-layered porous medium with an inclined permeability jump", Journal of Fluid Mechanics, vol. 902, 2020, A22-1 to A22-31. Chapter 3 of this thesis has been published as K. S. Bharath and M. R. Flynn, "Buoyant convection in heterogeneous porous media with an inclined permeability jump: an experimental investigation of filling box-type flows", Journal of Fluid Mechanics, vol. 924, 2021, A35-1 to A35-31. Chapter 4 is included only as the thesis chapter of this report and preparation of the manuscript for submitting it to a journal is currently underway. I was responsible for theoretical developments, data collection and analysis as well as the manuscript writing. Dr. M. R. Flynn was the supervisory author and was involved with concept formations and manuscript revisions.

Acknowledgements

I am deeply grateful to my family, friends, and mentors who have all contributed, in one way or another, to this work. Thank you to:

- my advisor, Dr. Morris Flynn, for hiring me with confidence and giving me an opportunity to pursue my PhD. His dedication to research and commitments as a supervisor have been continuous sources of inspiration and motivation for my research work. After years of working with him, I am proud to call him my mentor and an "Academic father".
- my thesis comittee, Dr. Vakhtang Putkaradze, Dr. Petr Nikrityuk and Dr. Mohtada Sadrzadeh, for their constructive feedbacks for making research progress and planning appropriate timeline for my PhD program through our committee meetings.
- Dr. Bruce Sutherland, for generously offering his laboratory space to conduct my experiments.
- my mom and dad, for absolutely everything. You deserved more than a line in this Acknowledgements.
- my sister (Asha) and brother-in-law (Sunil), for their moral support.
- the members of Morris research group for giving constructive feedback during our group meeting.
- and, last but not the least, all my friends and fellow students at the University of Alberta with whom I have shared this big adventure.

Table of Contents

List of Tables

List of Figures

Chapter 1

Introduction and overview

1.1 Fundamental forces for porous media flow

The two-phase flow in porous media is primarily influenced by a combination of viscous, gravitational, and capillary forces. The importance of the capillary force relative to the other two forces, i.e. viscous and gravity, is realised by comparing their magnitudes. The dimensionless numbers used to quantify these forces are

$$\text{Capillary number, Ca} = \frac{\mu U d_o^2}{\gamma k} \tag{1.1a}$$

$$\text{Bond number, Bo} = \frac{\Delta\rho g d_o^2}{\gamma} \tag{1.1b}$$

where μ is the absolute dynamic viscosity of the wetting fluid, U is a characteristic velocity, d_o is the mean grain diameter or the pore size, γ is the surface tension, k is the permeability, $\Delta\rho$ is the density difference between the two fluids and g is the acceleration due to gravity. The magnitudes of capillary and Bond numbers leads to various interfacial effects. When $\text{Ca} \ll 1$, capillary forces dominate and local variations in the pore throat size dictate the flow path, whereas, for $\text{Ca} \gg 1$, viscous forces dominate the capillary force leading to viscous fingering effects, also termed as Saffman-Taylor instability (Saffman & Taylor, 1958). Similarly, when $\text{Bo} \ll 1$, capillary forces dominate relative to the gravity force, whereas, for $\text{Bo} \gg 1$, the gravity dominates and acts as a mechanism to stabilize the viscous instability or capillary fluctuations at the flow front. For fluids forming a miscible interface, the viscous

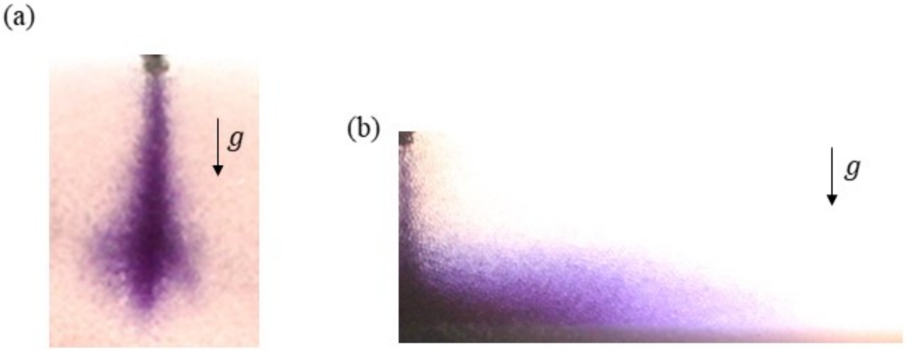

Figure 1.1: (a) Plume, and (b) Gravity current

fingers are dictated largely by mixing, such as by diffusion and/or hydrodynamic dispersion (Perkins & Johnston, 1963; Perkins *et al.*, 1965).

1.2 Primary flows in a porous medium

When a denser or lighter fluid is injected into a porous medium previously saturated with ambient fluid, a variety of flow patterns are possible up to and including the two end members of buoyancy induced or density driven flows, namely, plume vs. gravity current flow, as shown in figures 1.1 a and b, respectively. In the case of plumes, the flow occurs parallel to the acceleration due to gravity, whereas the gravity current flow is primarily horizontal and propagates along an impermeable or semi-permeable boundary. For a miscible system, be the flow more plume like or gravity current like, it can be categorized based on two dimensionless numbers, namely

$$\text{Reynolds number, Re} = \frac{U d_o}{\nu} \tag{1.2a}$$

$$\text{Péclet number, Pe} = \frac{U d_o}{D_m} \tag{1.2b}$$

where ν is the kinematic viscosity, D_m is the molecular diffusion coefficient and τ is the tortuosity constant[1]. When Re $\lesssim O(10)$, viscous forces dominate the inertial force and the flow is Darcy, whereas for Re $> O(10)$, inertial force remains dominant,

---

[1] The equation for tortuosity as a function of porosity, $\tau = 1 - A\ln(\phi)$, was proposed by Comiti & Renaud (1989), where A depends on the shape of particles and their mean orientation in the porous media.

such flows are categorized as non-Darcy. The Péclet number determines whether the flows are dominated by diffusion or dispersion. When Pe $\lesssim O(1)$ dispersion plays a subordinate role compared to the diffusion, whereas, for Pe $\gg O(1)$ dispersion plays a non-subordinate role.

1.3 Literature survey

1.3.1 Plume

For Darcy flows, as described earlier, the relative importance of dispersion to diffusion is characterized by the Péclet number, Pe. Using the boundary layer approximation, the quantitative details of the plume flow were derived for Péclet numbers of different orders. For diffusion dominant flows characterized by Pe $\lesssim \mathcal{O}(1)$, Wooding (1963) derived the equation for the plume volume flux considering a rectilinear two-dimensional geometry, which reads

$$\text{Volume flux, } Q = \left(\frac{36 D_m \phi F_0 k \Lambda^2 Z}{\nu}\right)^{1/3} \tag{1.3}$$

Here, ϕ is the porosity, F_0 is the source buoyancy flux, k is the permeability and Λ is the source width normal to this paper. Z points vertically downwards to the virtual origin.

In a similar spirit and again considering a rectilinear two-dimensional geometry, Sahu & Flynn (2015) derived the equations for volume flux and mean reduced gravity by considering Pe $\gg \mathcal{O}(1)$, implying that the flow remains dispersion dominant, and the relations for plume volume flux and reduced gravity respectively read as

$$\text{Volume flux, } Q = \left[\left(\frac{16 F_0 k \Lambda}{\pi \nu}\right)^2 \phi \alpha Z\right]^{1/4} \tag{1.4a}$$

$$\text{Reduced gravity, } g' = \left[\left(\frac{\pi F_0 \nu}{16 k \Lambda}\right)^2 \frac{1}{\phi \alpha Z}\right]^{1/4} \tag{1.4b}$$

Here, α is the transverse dispersivity.

1.3.2 Gravity current

1.3.2.1 Flow along an impermeable base

The earliest investigation of gravity current flow in porous media was conducted by Huppert & Woods (1995) for a two-dimensional rectilinear geometry. These authors examined from first principles the early-time spreading behaviour of a gravity current along an impermeable boundary having an arbitrary slope angle, θ. Assuming the pressure distribution within the gravity current is hydrostatic, Huppert & Woods (1995) derived a non-linear advection equation describing the time evolution of gravity current height, h, which reads

$$\phi\frac{\partial h}{\partial t} = \frac{kg'}{\nu}\left[\frac{\partial}{\partial x}\left(h\frac{\partial h}{\partial x}\right)\cos\theta - \frac{\partial h}{\partial x}\sin\theta\right] \tag{1.5}$$

where $g' = g\Delta\rho/\rho$ is the reduced gravity, x is the length measured in the direction of flow and t is time. In this model, Huppert & Woods (1995) considered the boundary separating the source fluid and its ambient as *sharp* and well-defined, compared to the overall scale of the flow. Later, Lyle *et al.* (2005) extended the analysis for an axisymmetric gravity current. In their respective studies, they showed that for a constant volume influx condition the length of the gravity current varies as $t^{2/3}$ for a rectilinear geometry and as $t^{1/2}$ for an axisymmetric case.

1.3.2.2 Flow along a permeable base

In contrast to an impermeable boundary, making the bottom boundary permeable introduces leakage or draining. The volume influx to the gravity current is now balanced between the along slope flow and the draining across the base of the gravity current. Previously, leakages were modeled as a sink or fissure (Neufeld *et al.*, 2009, 2011; Vella *et al.*, 2011), fracture (Farcas & Woods, 2013), edge drainage (Hesse & Woods, 2010; Rayward-Smith & Woods, 2011; Zheng *et al.*, 2013) and distributed leakage (Pritchard *et al.*, 2001; Neufeld & Huppert, 2009; Woods & Farcas, 2009;

Farcas & Woods, 2009; Yu *et al.*, 2017). In such case, (1.5) modifies to

$$\phi\frac{\partial h}{\partial t} = \frac{kg'}{\nu}\left[\frac{\partial}{\partial x}\left(h\frac{\partial h}{\partial x}\right)\cos\theta - \frac{\partial h}{\partial x}\sin\theta\right] - w_{\text{drain}} \tag{1.6}$$

where w_{drain} is draining flux term across the bottom boundary. Although various authors have modeled the draining term based on the type of leakage across the draining boundary, in the interest of the current study, we limit our focus to distributed leakage. Earlier, Pritchard *et al.* (2001) modeled the draining term considering distributed leakage along a horizontal permeable boundary (also referred to as the permeability jump), i.e. when $\theta = 0°$ where θ is measured with the horizontal. They also considered the permeability of the draining layer to be very small compared to the host layer, i.e. $k_2/k_1 \ll 1$ where k_1 and k_2 are the permeabilities of the host and draining layers, respectively, and the thickness of the draining layer is considered to be small. Then the vertical draining flux term was expressed as

$$w_{\text{drain}} = \frac{k_2 g'}{\nu}\left(\frac{h}{b}\right) \tag{1.7}$$

where b is the thickness of the draining layer. Their results indicate that the gravity current reaches a steady-state by traveling a finite distance along slope in a finite time, which they termed as the *runout* distance. At runout, the influx to the gravity current matches the basal draining occurring from underneath the gravity current. Later, Goda & Sato (2011) extend this draining model to a deep draining layer (of semi-infinite thickness) and derived the equation for draining flux, expressed as

$$w_{\text{drain}} = \frac{k_2 g'}{\nu}\left(1 + \frac{h}{l}\right) \tag{1.8}$$

where l is the time dependent length of the draining fluid. Goda & Sato (2011) also considered a horizontal permeability jump ($\theta = 0°$) in their study. Similar to the prediction made by Pritchard *et al.* (2001), results of Goda & Sato (2011) also predicted that the gravity current propagating along slope reaches a runout and thereby attains a steady-state. In studies conducted by Pritchard *et al.* (2001) and

Goda & Sato (2011), they considered no entrainment of ambient fluid into the draining fluid, and therefore assumed the value of g' in (1.7) and (1.8) is the same as that within the gravity current. Later, Sahu & Flynn (2017) through their experiments investigated the effect of ambient fluid entrainment on the density of the draining fluid.

Table 1.1 shows the summary of the gravity current analysis performed under different settings of the bottom boundary.

Table 1.1: Summary of gravity current analysis

Orientation of bottom boundary	Type	Depth of draining layer	Key citations
Horizontal	Impermeable	-	Huppert & Woods (1995); Lyle *et al.* (2005)
Horizontal	Permeable	Thin	Pritchard *et al.* (2001); Neufeld *et al.* (2009); Hesse & Woods (2010); Farcas & Woods (2013)
Horizontal	Permeable	Deep (semi-infinte thickness)	Goda & Sato (2011)
Horizontal	Permeable	Deep (intermediate thickness)	Sahu & Flynn (2017)
Inclined	Impermeable	-	Huppert & Woods (1995); Vella & Huppert (2006*a*); De Loubens & Ramakrishnan (2011)
Inclined	Permeable	Thin	Woods & Farcas (2009); Farcas & Woods (2009)
Inclined	Permeable	Deep (semi-infinte thickness)	Bharath *et al.* (2020) [reported here]
Horizontal / Inclined	Permeable	Deep (intermediate thickness)	Bharath & Flynn (2021) [reported here]

1.3.3 Porous media settings

1.3.3.1 Layering in porous media

Buoyancy-driven flow, leading to gravity current(s), within a porous medium of uniform permeability has been studied previously by a number of authors (Lyle *et al.*, 2005; Vella & Huppert, 2006*b*; Sahu & Neufeld, 2020). However, adding either thin or thick layers of different permeabilities provides a generic form of large-scale heterogeneities, which, in the real geological context typically extend a vertical distance of 1 to 10 m (Cowton *et al.*, 2016). Indeed layers are particularly widespread feature of sedimentary formations (examples are cited below in section 1.4). Already, we have described the study by Pritchard *et al.* (2001) who investigated the dynamical influence of a thin, low permeability horizontal layer added below the layer through which the gravity current primarily flows. Since the publication of Pritchard *et al.* (2001)'s work numerous studies have been performed by introducing only a thin layer to create heterogeneity within the porous medium (Woods & Farcas, 2009; Neufeld & Huppert, 2009; Hewitt *et al.*, 2014; Yu *et al.*, 2017; Hewitt *et al.*, 2020). An alternative form of layering was envisioned by Hesse & Woods (2010) and Rayward-Smith & Woods (2011), who analysed the spreading of buoyant fluid rising through a series of layers. Woods and his colleagues characterized the resulting dynamics in terms of an effective dispersion, which accounts for spreading owing to flow past the thin-layered structures or baffles. In contrast to thin layering induced heterogeneity, the effect of adding layers of deep or intermediate thickness on the spreading dynamics is far less explored. In the studies carried out to date, Goda & Sato (2011) and Sahu & Flynn (2017) investigated the gravity current(s) dynamics along a permeability jump by introducing a thick, low permeability region as a secondary (i.e. draining) layer. In all these various cases explored so far and depending on the type of heterogeneities considered, the flow patterns were predicted or observed to be unique in each of the cases.

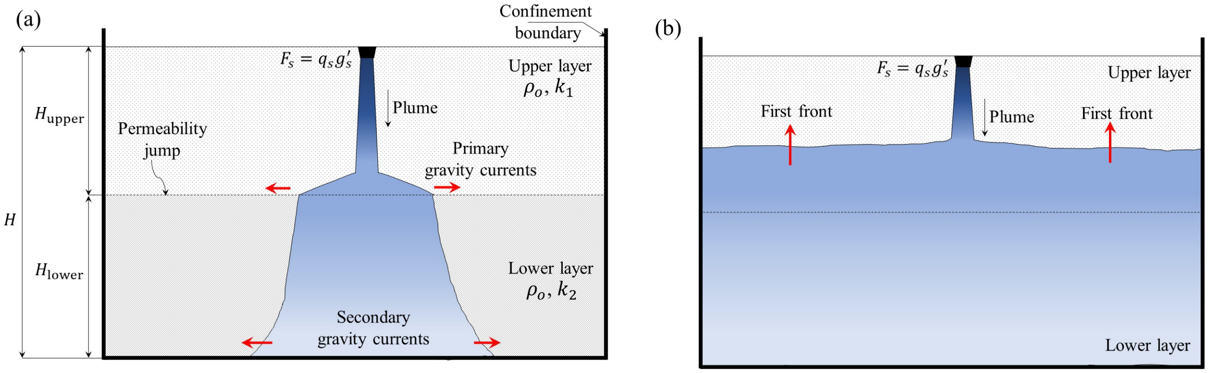

Figure 1.2: Filling box flows: (a) plume and gravity currents, and (b) advection of first front towards the source.

1.3.3.2 Convection in a confined porous medium

Examples of porous media buoyancy-driven flows, namely that of a plume and gravity current, have been investigated independently by various authors. However, in real-world situations both these end members can co-exist. For example, a gravity current may be fed by a vertically ascending or descending plume during carbon-dioxide sequestration (discussed below). At later times, the injected fluid propagating along horizontal or vertical directions reach their dead-end, which impedes their motion, such as those encountered during the acid-gas injection process (discussed below). Therefore, it is equally important to consider these flow impediments in our study and to predict their influence on the flow dynamics of the injected fluid.

In the light of the above details, investigations involving the two end members of buoyancy-driven flows, have closely followed the analysis within a "filling box" environment. A "filling box" can be defined as the buoyant convection that arises in a closed or ventilated control volume where the convection is driven by a localized source situated on the boundary that produces an ascending or descending plume. Filling box flows were originally studied in the context of free turbulent plumes by Baines & Turner (1969), Sahu & Flynn (2015) adopted this methodology to an ambient consisting of a homogeneous porous medium. They later extended their study to a two-layered porous medium where the upper layer was alternatively more or less permeable than the lower layer (Sahu & Flynn, 2017). However, their investigation focused only on horizontal permeability jump interface. Figure 1.2 shows filling box flows for the case of a two-layer rectilinear porous medium where $k_2/k_1 \ll 1$. Filling box flows primarily consist of three flow components: (i) a negatively-buoyant plume originating from a discrete source, (ii) gravity currents consisting of discharged plume fluid that form in the upper and lower layers and move horizontally towards the sidewalls, and (iii) a first front that moves vertically upwards towards the plume source. All three flow components were identified in the experimental study by Sahu & Flynn (2017).

1.4 Applications

The model predictions and laboratory observations summarized in the previous sections attempt to mimic the occurrence of buoyant convection in several industrial and environmental scenarios. Some of the notable examples discussed below are during underground hydrogen storage (UHS), carbon-dioxide sequestration, acid-gas sequestration, groundwater contamination and aquifer thermal energy storage.

1.4.1 Underground hydrogen storage

In order to balance the fluctuating energy demand from renewable sources, it becomes necessary to develop pragmatic strategies for energy storage, whether storage timescales are measured in days, weeks or months. One promising solution is to use electrolysis to convert electricity into hydrogen (H_2), which is later injected into underground formations, referred to as underground hydrogen storage (UHS). Hydrogen can be stored using either salt caverns, depleted hydrocarbon reservoir and/or deep saline aquifers (European Commission, 2015). The key parameters to consider in the context of UHS are the volume of cushion gas (typically carbon-dioxide or methane), the volume of working gas (hydrogen), injection rates and withdrawal rates. The cushion gas refers to the gas permanently stored in the underground structure during the lifetime of the site. Its main function is to maintain the conditions required for adequate storage operation, such as pressure range, flow rate and avoidance of withdrawal contamination. In this regard, the interface formed between the cushion gas and hydrogen is free from surface-tension, i.e. Ca, Bo $\rightarrow \infty$, and therefore, the phenomenon of viscous fingering is dominated by hydrodynamic dispersion (Paterson, 1983). During the storage operation, hydrogen is injected into a cushion gas ambient contained within anticline layers of sandstone which are highly porous and permeable. The sandstone layers are separated by tight clay layers, as indicated in figure 3 of Feldmann *et al.* (2016). The low permeability clay layers, and their associated high interfacial forces, may in theory prevent upward migration of hydrogen. However, the buoyancy forces of hydrogen is approximately three times greater than those associated with carbon dioxide, another gas that is often injected into the subsurface (Heinemann *et al.*, 2021). Therefore, even hydrogen columns of relatively moderate height could lead to very high buoyancy force which in turn can open pathways for migration through the clay layers.

1.4.2 Geological sequestration of carbon-dioxide

Carbon-dioxide (CO_2) is a greenhouse gas which gets released from a variety of physical and chemical processes. It is identified as the primary contributor to global warming. To mitigate CO_2 emission, CO_2 is captured from the flue gas emitted by power plants and factories, compressed into supercritical fluid (sc-CO_2) and injected underground into deep saline formations (aquifers) or oil reservoirs, for long-time storage (Metz *et al.*, 2005; Lackner, 2003). This method is well known as Carbon Capture and Storage (CCS). The storage facilities selected are typically one to three kilometers deep, ten to five hundred meters thick, and hundreds of kilometers long. They usually consist of a layer of cemented sediments covered by a low-permeability layer, called the caprock, that retards the upward flow of CO_2 back to the surface, as shown in the figure 1.3 a. As depicted in the same figure, to reduce the risk of

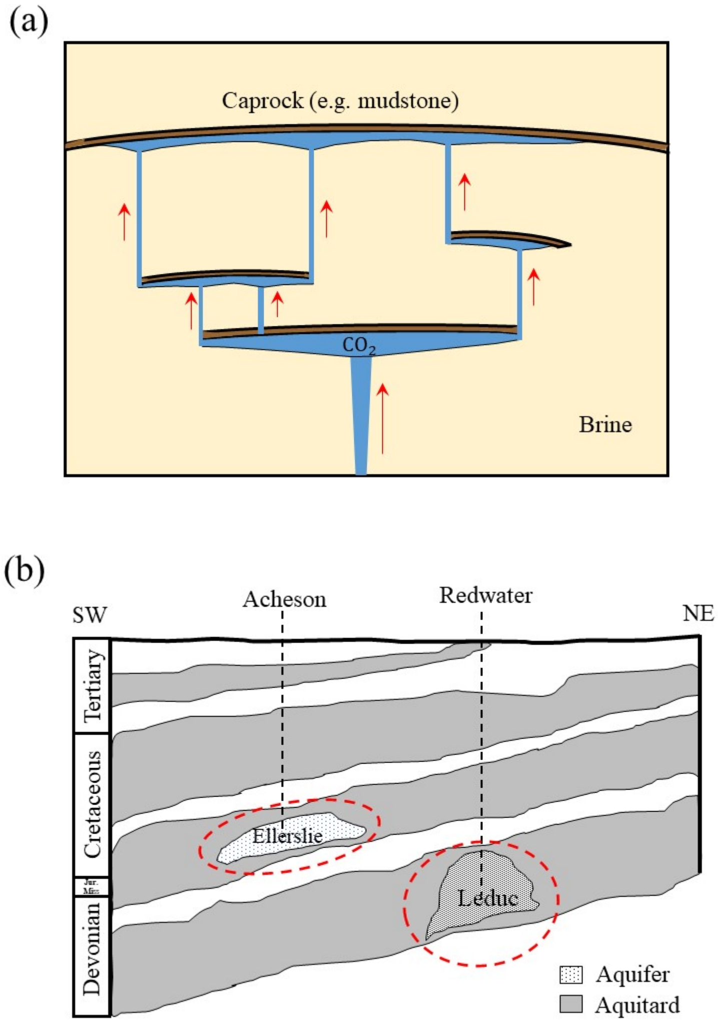

Figure 1.3: (a) The gravity currents are fed by vertically ascending plumes during geological storage of carbon-dioxide (image is inspired from Huppert & Neufeld (2014)), and (b) Shows the dip cross-section in western Canada where acid-gas injection takes place along the various injection points (image is inspired from Bachu *et al.* (2008*a*)). The red circles indicate the regions where the aquifers are laterally confined.

leakage from the storage facilities, the injection source is situated at the bottom of the storage horizon. This is strategy is termed as “Inject-low-and-let-rise” (Bryant *et al.*, 2008). In such a case, the gravity current formed beneath the low-permeability barriers is fed by a vertically rising plume. Furthermore, the total volume of sc-CO$_2$ that can be injected into the storage space is dependent on the storage capacity of the aquifer/reservoir. The storage capacity as defined by Szulczewski (2013), is the maximum amount of CO_2 that could be safely injected and securely stored under geological constraints, such as the aquifer/reservoir size and the integrity of its caprock. The role of CCS to mitigate global warming remains unclear partly due to the fact that there exists uncertainty in predicting the storage capacity. This uncertainty is again attributed to difficulty and total cost to map out geological structures (National Energy Technology Laboratory, 2010).

1.4.3 Geological sequestration of acid-gas

Acid-gas, consisting primarily of hydrogen-sulphide (H_2S) and carbon-dioxide (CO_2), are generated as a by-product of the gas sweetening process used to bring producer gases and solution gases up to market specifications for sales and transport. As an alternative to conventional methods for disposing of acid-gas, such as flaring (Emam, 2015) or the Claus process (Kohl & Nielsen, 1997), both of which carry environmental concerns, geological sequestration is being adopted. The potential geological injection sites include depleted hydrocarbon reservoirs and deep saline aquifers. For example, the injection takes places within the land-locked regions located on sedimentary basins, such the Beaverhill Lake - Mannville sedimentary succession in the Edmonton area (Bachu *et al.*, 2008*a*). As a matter of fact, the world's first acid-gas injection facility was started in Western Canada in 1989 on the outskirts of Edmonton, Alberta (Bachu & Gunter, 2004). Although the main purpose of acid-gas injection operations is to dispose of H_2S, significant fractions of CO_2 are being injected at the same time, because it is costly to separate the two gases (Bachu & Gunter, 2004). Therefore, acid-gas injection represents an analogue to the geo-storage of sc-CO_2. When the acid-gas mixture is injected into an aquifer, the degree to which it forms a plume and migrates from the injection point depends on various factors, including pressure and temperature, solubility, interplay between driving forces like buoyancy and aquifer hydrodynamics, and aquifer heterogeneity, which controls gravity override and viscous fingering. In the instance when the plume fluid strikes an inclined bedding plane having a dip angle, as shown in figure 1.3 b, buoyancy will distort the plume, which will advance faster updip and slower downdip. As a result, the plume will become elongated asymmetrically along up- and downdip sides. Furthermore, in the presence of lateral and vertical confinements (e.g. see the aquifers circled in red in figure 1.3 b), the trajectory of the along slope plume fluid is altered, which has a consequence of filling up the aquifer space. Predicting the filling time within aquifers or reservoirs having a complicated geometry remains a challenge, partly due to the lack of numerical models (Bachu *et al.*, 2008*b*).

1.4.4 DNAPL leakages contaminating groundwater

Dense non-aqueous-phase liquids (DNAPL), such as mercury, coal tar and creosote, are denser than water, and therefore, termed as "sinkers" (Fitts, 2013). DNAPL migrates through the granular aquifer and forms a pool over the bedrock surface. Later, they migrate further downward through the fractures in the rock and mix with water beneath, rendering this previously potable water unfit for our use. This was evident when large quantities of organic chemical wastes were buried in the site located in Niagara Falls, New York, between 1953 and 1975 (Cohen & Mercer, 1993). The wastes were observed to migrate to a depth of at least 30 m into the porous bed and spread horizontal distance of approximately 450 m from the source. Since DNAPLs are generally immiscible in water (Huling & Weaver, 1991), their downward migration through the pore structure is a function of pore size. In general, for high capillary numbers, DNAPL saturation also increases and therefore the large pores fill before their smaller counterparts. Further to the capillarity barrier, the bedrock also exhibits hydraulic conductivity contrasts in the form of layers of different permeability, and the permeability jumps across each layers dictates the distance that the liquid propagates along slope (Huling & Weaver, 1991; Steelman *et al.*, 2020).

1.4.5 Aquifer thermal energy storage

For larger scale seasonal underground thermal energy storage, Aquifer Thermal Energy Storage (ATES) offers the highest storage capacity (Lee, 2013). Deep and confined aquifers are used as storage facilities, such as those deployed in the Pacific Agricultural Research Center (PARC), situated in Agassiz, B.C. in Canada (Bridger & Allen, 2010). In general, a simple storage system consists of two sperate aquifers which are separated by an aquitard (very low permeability barrier). During summer months, cool groundwater from one aquifer is extracted and supplied to cool the building, and later the resulting high temperature water is pumped back into the second aquifer. This flow is reversed during the winter months to heat the building (Ibrahim & Rosen, 2010). The geothermal heating system used in PARC contains four such aquifers, which are located 60 m deep and spaced 90 m apart. The average storage temperature varied in the range of 2.5° C to 18.4° C. The thermal recovery efficiency of such systems depends on the properties of the fluid and solid phases. In addition, each of the aquifers can have heterogeneity that can have impact of the rate of filling and time taken to fill the complete volume.

1.5 Knowledge gaps

The nature of porous media in most of the geological formations is normally unknown and monitoring the flow is very expensive. Therefore, scientists and engineers rely heavily on mathematical and statistical methods to understand and predicts the flow behaviour inside these formations. Despite the advances made by various researchers, some of which are summarized in section 1.3, there still remains tremendous potential for improving our ability to predict the patterns in buoyancy-driven flows in relation to various applications described in section 1.4. In particular, as compared to numerous studies carried out in a homogeneous porous medium, the fluid dynamics inside a heterogeneous porous medium is far less explored. Therefore, we aim to investigate some of the non-trivial flow dynamics (both short- and long-term) that can occur in a porous media having layered heterogeneities. In this regard we identify the following knowledge gaps:

i. Most previous studies related to gravity current flows (Huppert & Woods, 1995; Pritchard *et al.*, 2001; Lyle *et al.*, 2005; Goda & Sato, 2011; Sahu & Neufeld, 2020) were analysed by considering the volume source located at the bottom boundary. However, in practical applications and as depicted in figure 1.3 a, the injection point is at a certain vertical distance from the boundary. In other words, the source is not always located at the boundary, and in such cases, the gravity currents are fed by a vertically ascending or descending plumes. Therefore, to predict the flow behaviour within a given porous medium accurately, it is necessary to consider the spatial evolution of the plume fluid and the subsequent formation, from discharged plume fluid, of along-dip gravity currents. This is because the plume during its ascent or descent experience entrainment from its ambient fluid due to which the volume flux and density within the plume fluid changes with vertical distance, as described by the plume equations in section 1.3.1, which in turn changes the volume and density influx to the gravity current at the inlet. This consequently affects the size and the rate at which the gravity current propagates along-dip and also its steady-state solutions, such as the runout length.

ii. The equation for the gravity current is derived based on the fundamental assumption that a sharp interface exists between the source and ambient. However, there exist numerous cases in real-world flows where the interface is strongly influenced by hydrodynamic dispersion, both in the transverse and longitudinal directions, which tend to make the theory predictions to become less versatile and less robust. Therefore, further investigation is needed to determine the source conditions and porous media settings under which dispersion plays a non-subordinate role.

iii. In geological settings, the orientation of the layers of sediment are largely decided by the topography of the landscape and may be inclined at an angle, as seen in figure 1.3 b. In the limiting case studies, Goda & Sato (2011) and Sahu & Flynn (2017) considered the orientation of the permeability jump separating the two layers as horizontal. This preserves the flow symmetry on the left and right sides of the source. However, having an inclined permeability jump boundary breaks this symmetry and the associated non-trivial dynamics has not yet been explored.

iv. In the filling box experiments conducted by Sahu & Flynn (2017), the authors considered the effect of a horizontal permeability jump on the dynamics of the descending plume. The experimental images in figure 5 of their work shows that the draining fluid upon striking the bottom impermeable boundary give rise to the formation of a pair of secondary gravity currents in the lower layer. However, no further detailed investigation was made to understand the dynamic influence of these secondary gravity currents on the primary gravity currents in the upper layer. Furthermore, each of these gravity currents upon reaching the sidewall, starts to fill the two layers independently. The details of the filling box dynamics, such as the impact of source conditions and porous media configurations on the sequence of filling of the layers, which may in turn, impact the filling box time, is left unexplored.

v. In the context of multi-layered porous media configuration, in real-world cases there exists numerous settings, wherein, distributed draining occurs across sedimentary layers. To the best of our knowledge, in the existing literature available to date, there has been no analytical study made to predict the pattern of buoyancy-driven flow in a porous media having multi-layers with different permeability jumps.

1.6 Thesis scope and outline

In this Thesis, we use theory, CFD simulations and experiments to clarify the knowledge gaps identified in section 1.5. The objectives of this thesis are threefold: (i) to predict the early-time dynamics of the gravity currents, travelling up- and downdip, along an inclined permeability jump boundary, (ii) to investigate the late-time dynamics of the plume fluid inside a two-layered porous media confined within impermeable boundaries, and (iii) to predict the flow patterns in a multi-layered porous media having layers of different permeabilities. In the spirit of addressing these objectives, each of these goals is framed as a separate chapter, i.e. Chapter 2, Chapter 3 and Chapter 4, which are further outlined below.

In Chapter 2, we derive an integrated theoretical model, by considering the volume influx to the gravity current(s) fed from a vertically descending plume, and predict both transient- and steady-state responses as the gravity current(s) propagate along an inclined permeability jump boundary. In the spirit of corroborating theory with experiments, we perform laboratory experiments and compare the flow patterns. In the process, we also emphasize the importance of flow dispersions, that are being neglected as a results of making sharp interface assumption in our theoretical model, as-well-as, by many other authors (Huppert & Woods, 1995; Pritchard *et al.*, 2001; Lyle *et al.*, 2005; Goda & Sato, 2011). We also quantify the dispersion as a function of source conditions and porous media configuration from our experiments. This chapter addresses the open questions raised in (i) and (ii) of section 1.5.

In Chapter 3, by making use of the "filling box" model, a comprehensive study is performed on the long-term fate of injecting the source fluid in a two-layered porous media confined between the bottom and sidewall boundaries. The key aspects such as (i) the influence of intermediate depth of the lower layer on the "primary" gravity current in the upper layer, (ii) priority of filling between the upper and lower layers, and the filling box time(s) as a function of source conditions and permeability jump angle, and (iii) deflection in plume trajectory caused due to asymmetric filling of the box on either side of the source position (which has not been observed before in context to porous media flows), are the highlights of this chapter. This chapter addresses (iii) of section 1.5.

We extend our study beyond two-layers and predict the flow patterns formed in a multi-layered porous media configuration in Chapter 4. For this we seek steady-state form of equations from the theory derived in Chapter 2, and later extend it to multiple layers. Further to compare theory predictions, we perform simulation using finite-element based multiphysics simulator COMSOL, and later compare the results obtained at steady-state. Through this study, we investigate the impact of adding multiple layers of intermediate permeabilities between the upper and lower layers on the extent of lateral spreading of the source fluid and the storage area. The flow patterns observed in multi-layered porous media form a key observation of this study and provides answers to (iv) of section 1.5.

As a final chapter, key conclusion (future topics) obtained from (related to) the present analyses are summarized in Chapter 5.

Several parts of this thesis have published or presented in conferences/symposia, as summarized below in tables 1.2 and 1.3, respectively.

Table 1.2: Scientific contribution arising from the present thesis.

Chapter	Journals	Status	Co-author(s)
2	*J. Fluid Mech.*	Published	M. R. Flynn, C. K. Sahu
3	*J. Fluid Mech.*	Published	M. R. Flynn

Table 1.3: List of scientific meetings where parts of this thesis work have been presented by the author. Abbreviations are as follows: APS - DFD: American Physical Society - Division of Fluid Dynamics, IGR: Institute of Geophysical Research, CAWQ: Canadian Association on Water Quality. Moreover, Interpore is an annual conference organized by the International Society of Porous Media.

Chapter(s)	Conference/Symposium	Location	Month and Year
2	APS - DFD	Atlanta, USA	Nov. 2018
2	APS - DFD	Seattle, USA	Nov. 2019
2, 3	APS - DFD	Chicago, USA *(Virtual event)*	Nov. 2020
4	APS - DFD	Phoenix, USA	Nov. 2021
2	12th Interpore	*(Virtual event)*	Aug - Sept. 2020
3	13th Interpore	*(Virtual event)*	May - June. 2020
2	11th Western CAWQ Symposia	Univ. of Alberta	May. 2019
2,3,4	IGR Symposia	Univ. of Alberta	Oct. 2017, Oct. 2018, April & Nov. 2019, Nov. 2020, April. 2021

Chapter 2

Isolated buoyant convection in a two-layered porous medium with an inclined permeability jump[1]

2.1 Abstract

The migration of dense fluid through a saturated, layered porous medium leads to two end-member examples of buoyancy-driven flow, namely plumes and gravity currents. Herein we develop an integrated theoretical model to study this scenario for the special case where the boundary between the permeable layers, in a two-layered porous medium, is inclined at an angle to the horizontal. Far from being a routine detail, the inclination of the permeability jump leads to a symmetry-breaking: up- and downdip flows have different volume fluxes and travel (possibly substantially) different distances, before becoming arrested at the point where plume inflow balances basal draining. Our model predicts these associated runout lengths and the transient approach thereto. Predictions are validated with measurements from similitude laboratory experiments, in which the upper and lower layers are comprised of glass beads of different diameters. Experiments are conducted for a range of inclination angles and also a range of plume source conditions. The experimental data suggest a complicated structure for the gravity currents, whose boundaries are blurred by

---

[1] Bharath, K. S., Sahu, C. K. & Flynn, M. R. 2020 Isolated buoyant convection in a two-layered porous medium with an inclined permeability jump. *J. Fluid Mech.* **902**, 1–31.

dispersion in a manner not captured by our (sharp interface) model. This observation has particular significance in predicting the lateral spread of contaminated fluid through real geological formations, particularly in instances where e.g. groundwater contamination is of particular concern.

2.2 Introduction

Geological strata represent a valuable resource, not only in terms of the mineral wealth that they may contain, but also in terms of their ability to (seasonally) store internal energy (MacKay, 2009) and to (permanently) store anthropogenic pollutants. In this latter capacity, much attention has been paid to the sequestration of supercritical carbon-dioxide (CO_2) in various locales e.g. China, Canada, Norway, Australia, the United States and the United Kingdom (Tang *et al.*, 2014). Less thoroughly studied in the academic literature, though still important, is the disposal of acid-gas in depleted oil and gas reservoirs or deep saline aquifers. Acid-gas injection often occurs in land-locked regions located on sedimentary basins, such as Labarge, Wyoming, USA (Parker *et al.*, 2011) and in the Alberta Basin in Western Canada (Bachu *et al.*, 2008*a*). In either case, acid-gas injection operations are often thought to represent a small-scale analogue of CO_2 sequestration. To this end, and for both acid-gas and CO_2 sequestration, concerns persist related to the long-term confinement of fluid injected deep underground. Such concerns are exacerbated by the difficulty and expense of monitoring injectate migration and the uncertainties inherent with forward-simulating numerical models (Bachu *et al.*, 2008*b*). Thus, there is an ongoing need for comparatively simple analytical models that provide qualitative and quantitative insights into the nature of buoyancy-driven flow in porous media. When a light or dense fluid is injected into a porous medium, its subsequent migration depends on various factors, such as pressure and temperature, solubility, the interplay between hydrodynamic and buoyancy forces and the heterogeneity of the medium. When, as is typical, density differences arise, the injectate may migrate in the form

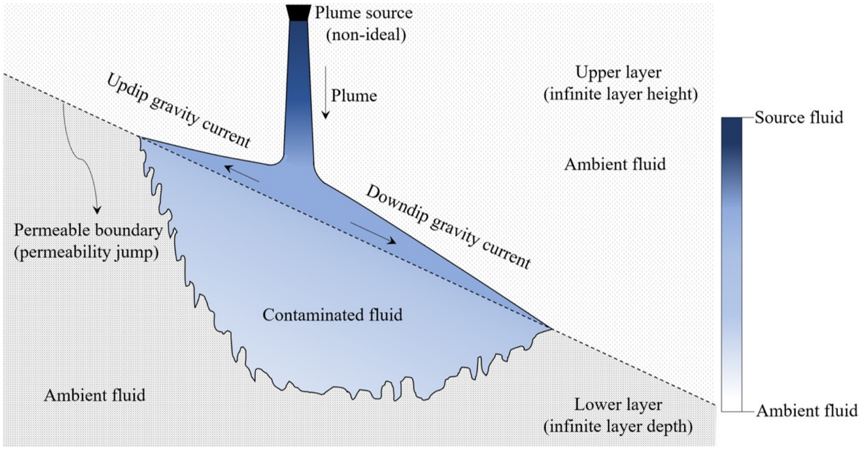

Figure 2.1: [Color] Schematic of discharged plume fluid propagating as a pair of leaky gravity currents along an inclined permeability jump. The colorbar on the right indicates the variation in density as the source fluid migrates within the porous medium.

of a vertical plume or in the form of horizontal or sloping gravity current(s). Indeed, one may feed the other as when a plume strikes a impermeable boundary (Sahu & Flynn, 2015) or permeability jump (Sahu & Flynn, 2017) or when a gravity current drains from the edge of an impermeable lens (Hesse & Woods, 2010, and see also figures 10.10 and 10.11 of Woods (2014)).

Gravity currents in porous media have been studied widely in the past decades both experimentally and theoretically. One of the earliest investigations was conducted by Huppert & Woods (1995), who examined the short- and long-term spreading behavior of gravity currents along both horizontal and inclined impermeable boundaries. Since the publication of this pioneering work, numerous follow-up studies have been conducted to explore the effect of e.g. a time-varying source (Vella & Huppert, 2006*a*), density stratification within the gravity current (Pegler *et al.*, 2016), and vertical confinement (Nordbotten & Celia, 2006; Zheng *et al.*, 2015). Also, and although it is theoretically and experimentally expedient to assume the boundaries confining the gravity current to be impermeable, there are numerous practical situations wherein leakage may occur through large faults or high-permeability zones in caprock (Fitts & Peters, 2013; Espinoza & Santamarina, 2017); in such cases drainage must be considered. To this end, studies have focused on the case of an isolated (Vella *et al.*, 2011) vs. a distributed sink. In the latter case, Pritchard *et al.* (2001), Neufeld & Huppert (2009) and Farcas & Woods (2009) studied the flow of a gravity current over a thin permeable layer. The extension to the thick lower layer case has been explored by Goda & Sato (2011) and Sahu & Flynn (2017) among others. Whatever the lower layer thickness, the draining flow from the underside of the gravity current has been modeled by considering the flow to be driven by the hydrostatic head of the overlying gravity current (Acton *et al.*, 2001; Pritchard *et al.*, 2001; Goda & Sato, 2011). In case of a thick lower layer, the source fluid is pulled both along and across the interface between the two layers, which we call the permeability jump, and the gravity current ultimately reaches a terminal or runout length. As suggested by the name, the runout length is the horizontal distance at which the volume of fluid supplied to the gravity current is just balanced by that draining from underneath. Whereas the case of a horizontal permeability jump has been studied by Goda & Sato (2011) and Sahu & Flynn (2017), there are numerous geological examples where the permeability jump makes a non-trivial angle to the horizontal. These examples include the Wabamun groups (Bachu *et al.*, 2008*b*) in Western Canada, which are used as repositories for acid-gas, the Entrada and Weber formations in the United States Rocky Mountain region (McPherson & Matthews, 2013) and China's Shiqianfeng group in the Ordos Basin (Jing *et al.*, 2019) all of which are used as repositories for supercritical CO_2. For the examples just cited, the regional dip angles vary from as little as 0.4° to as much as 20°.

In light of the above examples, it is surprising that more attention has not been paid to the (asymmetric) problem of gravity current propagation along a sloping, permeable boundary. Adding to the flow complexity is the possibility that the up- and downdip gravity currents are fed by a plume rather than by an isolated source located along the permeability jump itself. A schematic of this flow is illustrated in figure 2.1. Here, and consistent with the laboratory experiments to be described later, we consider a source of dense fluid located significantly above the permeability jump that leads to the formation of a descending plume in the upper layer. On the other hand, such details of orientation (uprising or downmoving) are irrelevant provided that density differences are modest so that the flow is Boussinesq. Note also from figure 2.1 that the plume and gravity currents feed back upon each other, and the composite problem is therefore more nuanced than either constituent part.

Addressing the above described open problem is the primary objective of the present study. Precise goals include (i) characterizing the relative up- vs. downdip flow as a function of θ, the permeability jump angle, and, (ii) resolving the time-dependent advance of the up- and downdip gravity currents until the respective runout lengths are reached. As part of the analysis, key differences with the horizontal permeability jump case will be highlighted. Complementing the above analysis, our study also includes similitude laboratory experiments. Although their ostensible purpose is to provide data to corroborate the theoretical model, we shall see that the experimental images reveal behaviour that highlights the limitations of considering a sharp interface in the gravity current model.

The rest of the manuscript is organized as follows. In section 2.3, we derive a theoretical model for the flow in question and discuss some of the key model predictions in section 2.4. section 2.5 describes the laboratory experiments and the techniques used to analyze experimental images along with a qualitative comparison with the theory. Quantitative comparisons are reserved for section 2.6. section 2.7 presents an overarching summary in which ideas for future study are briefly outlined.

2.3 Theoretical modeling

2.3.1 Problem description

To model the flow described in figure 2.1, we consider a two-layer porous medium usual notations as illustrated schematically in figure 2.2. The permeability and porosity in

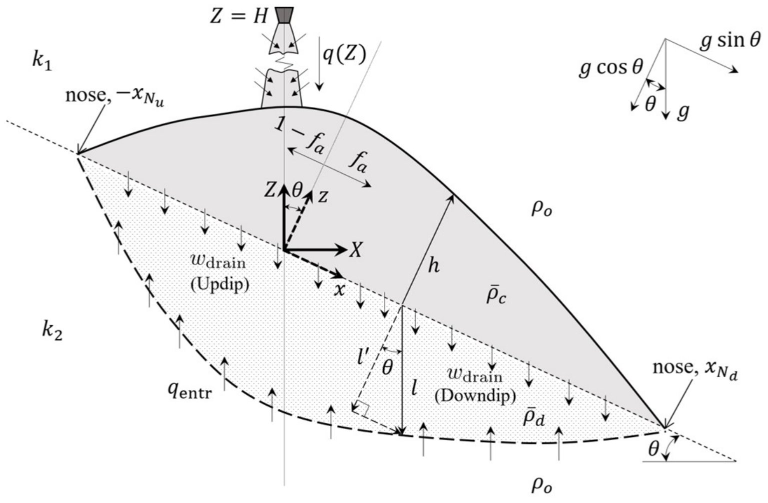

Figure 2.2: Definition schematic showing the propagation of discharged plume fluid in the up- and downdip directions along the inclined permeability jump. Draining into the lower layer is also indicated.

the upper layer are, respectively, k_1 and ϕ_1, while the corresponding values in the lower layer are, respectively, k_2 and ϕ_2. The permeability jump makes a constant angle θ with the horizontal. The natural coordinate system in 2D space is represented by (X,Z), where the vertical Z-axis is aligned anti-parallel to gravitational acceleration g. For reference, note that the coordinate system (x,z) associated with the along- and cross-jump directions is obtained from (X,Z) by a clockwise rotation of θ about the Y-axis, Y being the direction normal to the page. Coordinate rotation can be expressed mathematically using a transformation matrix, i.e.

$$\begin{bmatrix} x \\ z \end{bmatrix} = \begin{bmatrix} \cos\theta & \sin\theta \\ -\sin\theta & \cos\theta \end{bmatrix} \begin{bmatrix} X \\ Z \end{bmatrix} \tag{2.1}$$

We position the origin of both coordinate systems on the permeability jump, directly below the dense line source, which is itself is positioned at $(X = 0,\ Z = H)$ – see figure 2.2.

Our theoretical model is predicated on the following simplifying assumptions; (i) Although the upper and lower layers are assumed to support different permeabilities, the porosities are assumed equal, i.e. $\phi_1 = \phi_2 \equiv \phi$. (ii) The upper and lower layers are assumed to be very deep in vertical extent (Goda & Sato, 2011); the consequences of assuming otherwise will be briefly highlighted in section 2.5. (iii) Initially, the entire porous medium is assumed to be uniformly saturated with ambient fluid of density ρ_o. (iv) The source and ambient fluids have equal dynamic viscosities and are assumed to be fully miscible so that effects due to capillarity can be ignored. (v) When the plume strikes the permeability jump at $x = 0$, all of its fluid is then discharged in the form of flows propagating up- and down-dip; this assumption is defensible provided $k_2/k_1 \ll 1$ – see e.g. figure 3 of Sahu & Flynn (2017). (vi) The so-produced up- and downdip gravity currents remain long and thin. (vii) Consistent with Bear (1972); Woods & Mason (2000); Pritchard *et al.* (2001); De Loubens & Ramakrishnan (2011), gravity current fluid is at all times separated from overlying ambient fluid by a sharp interface. (viii) The density difference between the source fluid and the ambient fluid is moderate and the flow remains Boussinesq everywhere in the domain. (ix) Spatial variations in the density within the up- and downdip gravity currents and within the contaminated fluid consisting of discharged plume fluid that has drained into the lower layer are modest and can be ignored to leading order.

The plume line source discharges fluid of density $\rho_s > \rho_o$ at a constant volume flux per unit width, q_s. The source buoyancy flux per unit source width is $F_s = q_s g_s'$, where $g_s' = g(\rho_s - \rho_o)/\rho_o \ll g$ is the source reduced gravity. As the dense fluid falls downwards, entrainment occurs as a result of which the volume flux of the resulting plume increases with the vertical distance from the source. Using a boundary layer approximation, Wooding (1963) derived an expression to predict this variation in the limit of small Péclet number, i.e. $\mathrm{Pe} = U d_o \tau / D_m \ll O(1)$, where U is a characteristic velocity, d_o is the mean grain diameter, D_m is the molecular diffusivity. Further, $\tau > 1$ is the (hydraulic) tortuosity, which is defined as the square of the hydraulic flow path length to the corresponding straight-line length (Carman, 1937) or as the product of porosity and a formation factor (Clennell, 1997; Ghanbarian *et al.*, 2013)[2]. Later,

---

[2] The equation for tortuosity as a function of porosity, $\tau = 1 - A\ln(\phi)$, was proposed by Comiti & Renaud (1989), where A depends on the shape of particles and their mean orientation in the porous medium. For randomly packed spheres with $\phi = 0.35$, A has a value of 0.49 (Mauret & Renaud,

Sahu & Flynn (2015) derived a similar relation for Pe $\gg O(1)$ and also proposed a relation for the variation of the plume reduced gravity with Z. Herein, we model the flow assuming Pe $\gg O(1)$ – see section 2.3.4.

When the plume strikes the permeability jump, discharged plume fluid is divided into equal ($\theta = 0°$) or unequal ($\theta \neq 0°$) flows to the right and left. The discharged plume fluid propagates as a pair of leaky gravity currents under a balance of buoyancy and viscosity with simultaneous draining into the lower layer. The pressure is continuous along $z = h(x, t)$ where h denotes the gravity current height, measured perpendicular to the permeability jump – see figure 2.2. Because of the continual addition of fluid from above, h steadily increases with time, t. Consequently, and because the density, ρ_p, and plume volume flux per unit width, q_p, vary with the vertical coordinate due to entrainment, the fluid feeding the gravity current has a density that slowly increases with time and a volume flux that slowly decreases with time. The influx density is denoted by $\rho_p(h_0)$ with a corresponding volume flux per unit width denoted by $q_p(h_0)$ where $h_0 \equiv h(x = 0, t) \equiv h_0(t)$ is the time-dependent gravity current height measured directly below the plume source. The volume influx $q_p(h_0)$ is obviously the same q_c. In a similar spirit, and neglecting spatial variations of the gravity current density, we have that $\bar{\rho_c} = \rho_p(h_0)$ where $\rho_o < \bar{\rho_c} < \rho_s$. Although the spatially-uniform approximation is clearly a theoretical simplification relative to the real flow, we expect internal stratification effects to be relatively minor provided H is not small. With this assumption, the average density difference between the up- and downdip gravity currents and the ambient fluid is $\Delta\bar{\rho_c} = \bar{\rho_c} - \rho_o$ and the corresponding reduced gravity is $\bar{g_c'} = g(\Delta\bar{\rho_c}/\rho_o)$.

Below the permeability jump, there is a draining of discharged plume fluid into the lower layer. The draining flow displaces less dense ambient fluid thereby creating an unstable interface leading to Rayleigh–Taylor type fingering (Saffman & Taylor, 1958; Homsy, 1987) – see figure 2.1. The occurrence of similar fingering phenomena has been

---

1997), and the tortuosity according to the equation can be estimated to be 1.51.

observed previously for gravity currents propagating along a horizontal permeability jump (Sahu & Flynn, 2017) or along the underside of a sloping, impermeable boundary (MacMinn & Juanes, 2013). A consequence of the fingers is that some mixing of draining discharged plume fluid and ambient fluid must occur. To distinguish the less dense discharged plume fluid in the lower layer from that more dense discharged plume fluid in the upper layer, we shall, in the lower layer, make reference to *contaminated* fluid, which in figure 2.2 is characterized by a depth l. By contrast, when we refer to discharged plume fluid, it should hereafter be understood that we refer specifically to the upper layer.

As a further consequence of the mixing described above, we cannot, strictly speaking, assume a sharp interface in the lower layer c.f. figure 2.1. Nonetheless, and for theoretical expediency, we assume a spatially-uniform mixing process in the lower layer and thereby define an average interface location for the contaminated fluid relative to the ambient – see figure 2.2. The average density of the contaminated fluid is $\bar{\rho_d} < \bar{\rho_c}$ and the corresponding density difference with the ambient fluid is $\Delta\bar{\rho_d} = \bar{\rho_d} - \rho_o$. Thus the mean reduced gravity of the draining fluid is expressed as $\bar{g_d'} = g(\Delta\bar{\rho_d}/\rho_o) < \bar{g_c'}$. Determination of $\bar{\rho_d}$ and $\bar{g_d'}$ will be discussed below.

2.3.2 Gravity currents

Consider, as in figure 2.2, a two-dimensional flow of the gravity currents propagating along the permeability jump in the upper layer along the up- and downdip directions. Let the Darcy velocity of the gravity currents be $\boldsymbol{u}_c \equiv (u_c, w_c)$, with components u_c and w_c in the along and cross jump directions, respectively. As noted above, the gravity currents are assumed long and thin (small aspect ratio, ε = height/length $\ll 1$). As a consequence, and consistent with the Dupuit approximation[3](see Bear,

---

[3] The Dupuit assumption is similar to the shallow water assumption in that both suppose the following: (i) small aspect ratio and hence the pressure is hydrostatic, (ii) Negligible vertical component of the flow. We retain the terminology "Dupuit approximation" because this is consistent with the existing groundwater flow literature (Bear, 1972; Cushman *et al.*, 2016).

1972, and appendix A.3) w_c can be considered small compared to u_c and the cross layer pressure gradient within each gravity current can be considered approximately hydrostatic (Huppert & Woods, 1995). Considering the along jump flows in a rotated coordinate system for $\theta > 0°$, we define the hydrostatic pressure in the cross flow direction as

$$P_c(x, z, t) = p_c(x, t) - \bar{\rho}_c g z \cos\theta \tag{2.2}$$

Here, $p_c(x, t)$ is given by

$$p_c(x, t) = P_o + (\bar{\rho}_c - \Delta\bar{\rho}_c) g x \sin\theta + \Delta\bar{\rho}_c g h \cos\theta \tag{2.3}$$

where P_o is the pressure measured at the origin. Using Darcy's law, it can be shown that the along jump flow velocities with the up- and downdip gravity currents are

$$u_c = -\frac{k_1 \Delta\bar{\rho}_c g}{\mu} \begin{cases} \dfrac{\partial h}{\partial x}\cos\theta + \sin\theta, & [\text{Updip, } -x_{N_u} < x < 0] \\[2ex] \dfrac{\partial h}{\partial x}\cos\theta - \sin\theta, & [\text{Downdip, } 0 < x < x_{N_d}] \end{cases} \tag{2.4}$$

where μ is dynamic viscosity and x_{N_u} and x_{N_d} are the nose locations in the up- and downdip directions, respectively – see figure 2.2. The velocities prescribed by (2.4) apply for $z < h$. Because the upper layer is assumed semi-infinite, the velocity within the ambient is considered negligible (c.f. De Loubens & Ramakrishnan (2011)). To derive an evolution equation for h, we take the depth-average of the mass conservation equation, similar to (2.6) of Huppert & Woods (1995), and consider mass loss due to draining from the gravity current undersides. Upon substituting (2.4) into the resulting depth-averaged equation, we obtain

$$\phi\frac{\partial h}{\partial t} = \begin{cases} \dfrac{k_1 \bar{g}_c'}{\nu}\dfrac{\partial}{\partial x}\Big(h\dfrac{\partial h}{\partial x}\cos\theta + h\sin\theta\Big) + w_{\text{drain}}, & [\text{Updip, } -x_{N_u} < x < 0] \\[2ex] \dfrac{k_1 \bar{g}_c'}{\nu}\dfrac{\partial}{\partial x}\Big(h\dfrac{\partial h}{\partial x}\cos\theta - h\sin\theta\Big) + w_{\text{drain}}, & [\text{Downdip, } 0 < x < x_{N_d}] \end{cases} \tag{2.5}$$

where $\nu = \mu/\rho_o$ denotes the kinematic viscosity and w_{drain} is the draining velocity, an expression for which is provided in the following subsection.

2.3.3 Draining flow in the lower layer

Here, we evaluate the time evolution of the average position of the interface between the contaminated and the ambient fluids in the lower layer. The Darcy velocity of the contaminated fluid in the lower layer is $\boldsymbol{u_d} \equiv (u_d, w_d)$, having components u_d and w_d in the along and cross jump directions, respectively. For $\theta = 0°$, the along jump velocity in the lower layer u_d is considered by Acton *et al.* (2001) to depend only on the horizontal gradient of the hydrostatic pressure exerted by the gravity current, i.e. $\partial h/\partial x$. Meanwhile, the cross-jump component of velocity, w_d, depends not on $\partial h/\partial x$ but rather on h. Because $\partial h/\partial x$ can be shown to be both approximately constant and small compared to unity, $|u_d| \ll \left|w_d\right|$. Consequently, the influence of u_d on the draining velocity has typically been ignored in previous works. However, for inclined permeability jumps ($\theta \neq 0°$), the along jump velocities may be significant because they include gravitational acceleration projected into the along jump direction. Using Darcy's law, the along jump velocities just below the jump boundary are given by

$$u_d = -\frac{k_2 \Delta\bar{\rho}_d g}{\mu} \begin{cases} \dfrac{\partial h}{\partial x}\cos\theta + \sin\theta, & [\text{Updip}, \ -x_{N_u} < x < 0] \\[2ex] \dfrac{\partial h}{\partial x}\cos\theta - \sin\theta, & [\text{Downdip}, \ 0 < x < x_{N_d}] \end{cases} \tag{2.6}$$

Meanwhile, the cross jump component is given by

$$w_d = -\frac{k_2 \Delta\bar{\rho}_d g}{\mu}\left(1 + \frac{h}{l'}\right)\cos\theta \tag{2.7}$$

where l' is the depth of the contaminated fluid as measured below and perpendicular to the permeability jump – see figure 2.2. In contrast to the case of a horizontal permeability jump, $|u_d| \approx \left|w_d\right| \tan\theta$, so that $|u_d|$ can be neglected only for relatively modest θ. For larger θ, u_d becomes significant and needs to be considered when modelling the draining flow. In such cases, the net draining flow velocity w_{drain} is influenced by both the along jump velocity and the hydrostatic head in the cross-jump direction. To evaluate w_{drain}, we take the resultant of these two velocities, i.e. $\sqrt{u_d^2 + w_d^2}$. Consistent with figure 2.2, it can be shown that for draining lengths significantly greater than the gravity current height, the direction of w_{drain} remains vertical and its length is given as $l = l'/\cos\theta$. Taking these factors into consideration, the draining velocity can be written as

$$w_{\mathrm{drain}} = -\frac{k_2 \Delta\bar{\rho}_d g}{\mu}\Big(1 + \frac{h}{l}\cos\theta\Big) \tag{2.8}$$

In the limiting case when $\theta = 0$°, (2.8) reverts back to the expression used in previous works (Goda & Sato, 2011; Sahu & Flynn, 2017).

At the contaminated-ambient fluid interface, the volume flow rate per unit width, q_{entr}, of the ambient fluid that mixes into the draining gravity current fluid can be expressed in terms of w_{drain} as

$$q_{\mathrm{entr}} = \frac{\Delta\bar{\rho}_c - \Delta\bar{\rho}_d}{\Delta\bar{\rho}_d}\int_{-x_{N_u}}^{x_{N_d}} w_{\mathrm{drain}}\mathrm{d}x \tag{2.9}$$

see Appendix A.1. The entrainment prescribed by q_{entr} is important because it, along with w_{drain}, dictates the time rate of increase of the draining fluid length, l. Following the derivation of Appendix A.1 and incorporating (2.8), it can ultimately be shown that l satisfies the following evolution equation:

$$\phi\frac{\partial l}{\partial t} = -\frac{\bar{g}'_c}{\bar{g}'_d}w_{\mathrm{drain}} = \frac{k_1\bar{g}'_c}{\nu}\frac{k_2}{k_1}\Big(1 + \frac{h}{l}\cos\theta\Big) \tag{2.10}$$

As with (2.5), (2.10) is valid in the range $-x_{N_u} < x < x_{N_d}$.

2.3.4 Gravity currents and draining flows fed by a descending plume

Recall that the density of the fluid supplied to the gravity currents slowly increases with time as a result of the gradual increase of h. Wishing to account for this fact in the governing equations (2.5) and (2.10) we adopt (2.25) of Sahu & Flynn (2015), and write

$$g'_c = \left[\Big(\frac{\pi F_s \nu}{16 k_1}\Big)^2 \frac{1}{\phi\alpha(H + Z_s - h_0\cos\theta)}\right]^{\frac{1}{4}} \tag{2.11}$$

Here, the source correction term $Z_s = \dfrac{1}{\phi\alpha}\Big(\dfrac{\pi\nu}{16F_s k_1}\Big)^2 q_s^4$ is evaluated considering the volumetric flow rate q_s at the plume source. Also, α is the transverse dispersivity, whose connection to the porous medium grain size is discussed below in section 2.6.1. Substituting (2.11) into (2.5) and (2.10) yields, after some simplification,

$$\frac{\partial h}{\partial t} = \begin{cases} \beta(1-\chi h_{0^-}\cos\theta)^{-\frac{1}{4}}\Big[\dfrac{\partial}{\partial x}\Big(h\dfrac{\partial h}{\partial x}\cos\theta + h\sin\theta\Big) - KG'\Big(1+\dfrac{h}{l}\cos\theta\Big)\Big], \\ \hfill [\text{Updip}, -x_{N_u} < x < 0] \\ \beta(1-\chi h_{0^+}\cos\theta)^{-\frac{1}{4}}\Big[\dfrac{\partial}{\partial x}\Big(h\dfrac{\partial h}{\partial x}\cos\theta - h\sin\theta\Big) - KG'\Big(1+\dfrac{h}{l}\cos\theta\Big)\Big], \\ \hfill [\text{Downdip}, 0 < x < x_{N_d}] \end{cases} \tag{2.12}$$

and

$$\frac{\partial l}{\partial t} = \beta K \begin{cases} (1-\chi h_{0^-}\cos\theta)^{-\frac{1}{4}}\Big(1+\dfrac{h}{l}\cos\theta\Big), & [\text{Updip}, -x_{N_u} < x < 0] \\ \\ (1-\chi h_{0^+}\cos\theta)^{-\frac{1}{4}}\Big(1+\dfrac{h}{l}\cos\theta\Big), & [\text{Downdip}, 0 < x < x_{N_d}] \end{cases} \tag{2.13}$$

Here β is a velocity parameter, χ is a source parameter, K is the ratio of the lower to upper layer permeabilities and G' is the ratio of the lower to upper layer reduced gravities within the draining fluid and gravity currents, respectively. More precisely, and in symbols,

$$\beta = \frac{k_1}{\phi\nu}\Big[\Big(\frac{\pi F_s \nu}{16 k_1}\Big)^2 \frac{1}{\phi\alpha(H+Z_s)}\Big]^{\frac{1}{4}}, \qquad \chi = \frac{1}{H+Z_s}, \qquad K = \frac{k_2}{k_1}, \qquad G' = \frac{\bar{g}'_d}{\bar{g}'_c} \tag{2.14}$$

Regarding the permeability jump angle θ as a further independent parameter, there are a total of five variables in the governing equations (2.12) and (2.13).

2.3.5 Initial and boundary conditions

Recalling the initial condition of the porous medium to be uniformly saturated by ambient fluid, we initialize the gravity current height and draining length to zero, i.e. $h = l = 0$ at $t = 0$. For $t > 0$, (2.12) and (2.13) are solved using an influx boundary condition, which requires the time rate of volume increase of the up- and downdip gravity currents to balance the volume of fluid supplied by the descending plume. The plume volume flux per unit width, q_c, supplied at $x = 0$ increases with distance from the source. Analogous to (2.11), q_c can be expressed in terms of h_0 using

$$q_c = \Big[\Big(\frac{16 F_s k_1}{\pi\nu}\Big)^2 \phi\alpha(H + Z_s - h_0\cos\theta)\Big]^{\frac{1}{4}} \tag{2.15}$$

– see (2.24) of Sahu & Flynn (2015). The q_c in (2.15) is divided into unequal up- and downdip components for $\theta \neq 0°$. To this end, and borrowing the notation of Rayward-Smith & Woods (2011), we consider that the dimensionless fraction of the flow propagating downdip is f_a, while the remaining fraction traveling updip is $1 - f_a$. The influx boundary conditions are then represented as

$$\beta^2\Big(h\frac{\partial h}{\partial x}\cos\theta + h\sin\theta\Big)\Big|_{0^-} = -(1-f_a)\Gamma(1-\chi h_{0^-}\cos\theta)^{\frac{1}{2}}, \quad [\text{Updip, } -x_{N_u} < x < 0]$$

$$\beta^2\Big(h\frac{\partial h}{\partial x}\cos\theta - h\sin\theta\Big)\Big|_{0^+} = -f_a\Gamma(1-\chi h_{0^+}\cos\theta)^{\frac{1}{2}}, \quad [\text{Downdip, } 0 < x < x_{N_d}] \tag{2.16}$$

where $\Gamma = (k_1 F_s)/(\phi^2\nu)$ is a buoyancy flux factor. The two components of (2.12) are coupled by insisting that the gravity current height remains continuous at $x = 0$, i.e.

$$h_{0^-} = h_{0^+} \tag{2.17}$$

By enforcing this condition at each time step, f_a can be determined as a function of time t. A final boundary condition is applied at the noses of the up- and downdip gravity currents, such that

$$h_{-x_{N_u}} = l_{-x_{N_u}} = 0 \qquad \text{and} \qquad h_{x_{N_d}} = l_{x_{N_d}} = 0 \tag{2.18}$$

Finally, the global mass balance equation can be written symbolically as

$$\int_{-x_{N_u}}^{x_{N_d}} (h + |l|)\mathrm{d}x = \int_0^t \Big[\frac{\Gamma}{\beta}(1-\chi h_0\cos\theta)^{\frac{1}{4}} + \beta K(1-G')\int_{-x_{N_u}}^{x_{N_d}}\Big(1 + \frac{h}{l}\cos\theta\Big)\mathrm{d}x\Big]\mathrm{d}t \tag{2.19}$$

The former term on the right-hand side represents the volume of fluid discharged by the plume while the latter term corresponds to the volume of lower layer ambient fluid entrained into the contaminated fluid.

2.3.6 Dimensionless governing equations

Following Goda & Sato (2011), we define characteristic spatial and temporal variables, Π_x and Π_t, as follows:

$$\Pi_x = \frac{q_c|_{h=0}}{\phi\beta} \qquad \text{and} \qquad \Pi_t = \frac{q_c|_{h=0}}{(1-\delta\cos\theta)^{-\frac{1}{4}}\phi\beta^2} \tag{2.20}$$

where

$$\delta = \frac{16}{\pi}\Big(\frac{\phi\alpha}{H+Z_s}\Big)^{\frac{1}{2}} \tag{2.21}$$

Note that Π_x characterizes the distance measured along the permeability jump, whereas Π_t characterizes the speed of draining into the lower layer. Using the above characteristic variables, we non-dimensionalize other variables as follows:

$$x^* = \frac{x}{\Pi_x}, \qquad h^* = \frac{h}{\Pi_x}, \qquad l^* = \frac{l}{\Pi_x}, \qquad t^* = \frac{t}{\Pi_t} \tag{2.22}$$

Thus (2.12) and (2.13) may be respectively rewritten as

$$\frac{\partial h^*}{\partial t^*} = \begin{cases} \Big(\dfrac{1-\delta h^*_{0^-}\cos\theta}{1-\delta\cos\theta}\Big)^{-\frac{1}{4}}\Big[\dfrac{\partial}{\partial x^*}\Big(h^*\dfrac{\partial h^*}{\partial x^*}\cos\theta + h^*\sin\theta\Big) - KG'\Big(1+\dfrac{h^*}{l^*}\cos\theta\Big)\Big], \\ \hfill [\text{Updip}, \ -x^*_{N_u} < x^* < 0] \\ \Big(\dfrac{1-\delta h^*_{0^+}\cos\theta}{1-\delta\cos\theta}\Big)^{-\frac{1}{4}}\Big[\dfrac{\partial}{\partial x^*}\Big(h^*\dfrac{\partial h^*}{\partial x^*}\cos\theta - h^*\sin\theta\Big) - KG'\Big(1+\dfrac{h^*}{l^*}\cos\theta\Big)\Big], \\ \hfill [\text{Downdip}, \ 0 < x^* < x^*_{N_d}] \end{cases} \tag{2.23}$$

and

$$\frac{\partial l^*}{\partial t^*} = K \begin{cases} \Big(\dfrac{1-\delta h^*_{0^-}\cos\theta}{1-\delta\cos\theta}\Big)^{-\frac{1}{4}}\Big(1+\dfrac{h^*}{l^*}\cos\theta\Big), & [\text{Updip}, \ -x^*_{N_u} < x^* < 0] \\ \Big(\dfrac{1-\delta h^*_{0^+}\cos\theta}{1-\delta\cos\theta}\Big)^{-\frac{1}{4}}\Big(1+\dfrac{h^*}{l^*}\cos\theta\Big), & [\text{Downdip}, \ 0 < x^* < x^*_{N_d}] \end{cases} \tag{2.24}$$

The initial condition reads $h^* = l^* = 0$. Meanwhile, the boundary conditions (2.16) become

$$\Big(h^*\frac{\partial h^*}{\partial x^*}\cos\theta + h^*\sin\theta\Big)\Big|_{0^-} = -(1-f_a)(1-\delta h^*_{0^-}\cos\theta)^{\frac{1}{2}}, \quad [\text{Updip}, \ -x^*_{N_u} < x^* < 0]$$

$$\Big(h^*\frac{\partial h^*}{\partial x^*}\cos\theta - h^*\sin\theta\Big)\Big|_{0^+} = -f_a(1-\delta h^*_{0^+}\cos\theta)^{\frac{1}{2}}, \quad [\text{Downdip}, \ 0 < x^* < x^*_{N_d}] \tag{2.25}$$

Note that the choice of scalings associated with (2.20) eliminates the factor of Γ present in (2.16) but absent in (2.25). The height continuity and nose conditions respectively read as

$$h^*_{0^-} = h^*_{0^+} \tag{2.26}$$

and

$$h^*_{-x^*_{N_u}} = l^*_{-x^*_{N_u}} = 0 \qquad \text{and} \qquad h^*_{x^*_{N_d}} = l^*_{x^*_{N_d}} = 0 \tag{2.27}$$

Also, the global mass conservation equation (2.19) now reads

$$\begin{aligned}\int_{-x^*_{N_u}}^{x^*_{N_d}} (h^* + |l^*|)\mathrm{d}x^* = \frac{1}{(1-\delta\cos\theta)^{-\frac{1}{4}}} \int_0^t \Big[(1-\delta h^*_0\cos\theta)^{\frac{1}{4}} \\ + K(1-G') \int_{-x^*_{N_u}}^{x^*_{N_d}} \Big(1 + \frac{h^*}{l^*}\cos\theta\Big)\mathrm{d}x^*\Big]\mathrm{d}t^*\end{aligned} \tag{2.28}$$

Equations (2.23)-(2.28) contain four dimensionless variables, namely θ, δ, K and G'. Here, θ defines the left to right asymmetry of the flow; δ defines the influence of the plume source; K defines the cross flow resistance at the permeability jump; and G' defines the degree of entrainment experienced by the draining fluid. The first three of these variables are easily estimated for a given porous medium and plume source location. However, G', defined as the ratio of the reduced gravity in the lower vs. upper layers, remains to be determined. We adopt an empirical approach in estimating G' as described in section 2.6.1[4]. With this value (plus θ, δ and K) to hand, (2.23)-(2.28) may be solved numerically e.g. using the explicit finite-difference scheme descried in appendix A.2.

2.4 Theoretical predictions

Sample model output is illustrated in figure 2.3a, which shows the evolution of the discharged plume fluid for a permeability jump angle $\theta = 15°$. In the large time

---

[4] In section 2.6.1, it will be shown that G' depends on the plume source conditions and θ. The ramifications of this observation are deferred to section 2.6.3 where we draw comparisons between theory and experiment.

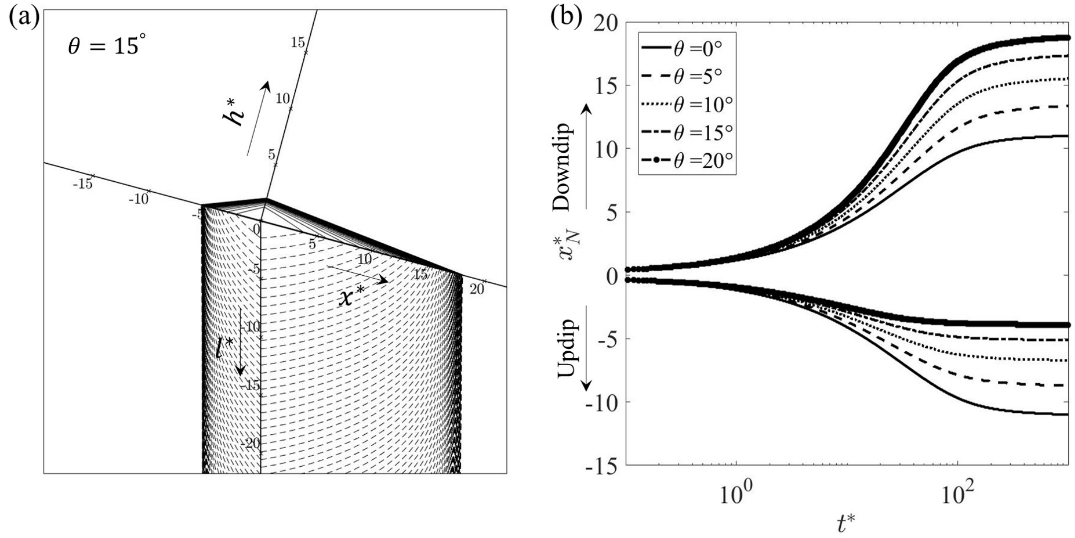

Figure 2.3: (a) Spatial-temporal evolution of the discharged plume fluid for $\theta = 15°$ (left panel). Contour lines of the flow front correspond to equally-spaced time intervals, (b) Nose positions, both up- ($x^*_N < 0$) and downdip ($x^*_N > 0$), compared for various θ (left panel). Results are shown assuming $\delta = 0.1$, $K = 0.1$ and $G' = 0.4$.

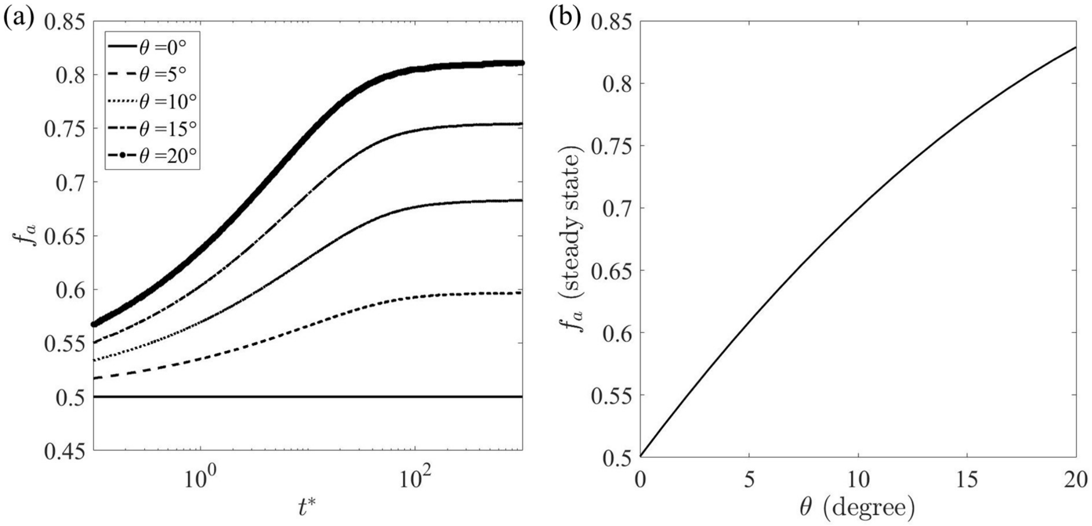

Figure 2.4: Variation of the downdip flow fraction f_a as a function of (a) time t^*, compared for various θ (left panel), and (b) permeability jump angle θ, at steady state (right panel). Results are shown assuming $\delta = 0.1$, $K = 0.1$ and $G' = 0.4$.

limit, the up- and downdip gravity currents reach their respective runout lengths. Similar behaviour was predicted by Goda & Sato (2011) and was also observed in laboratory experiments by Sahu & Flynn (2017), but both of these previous studies

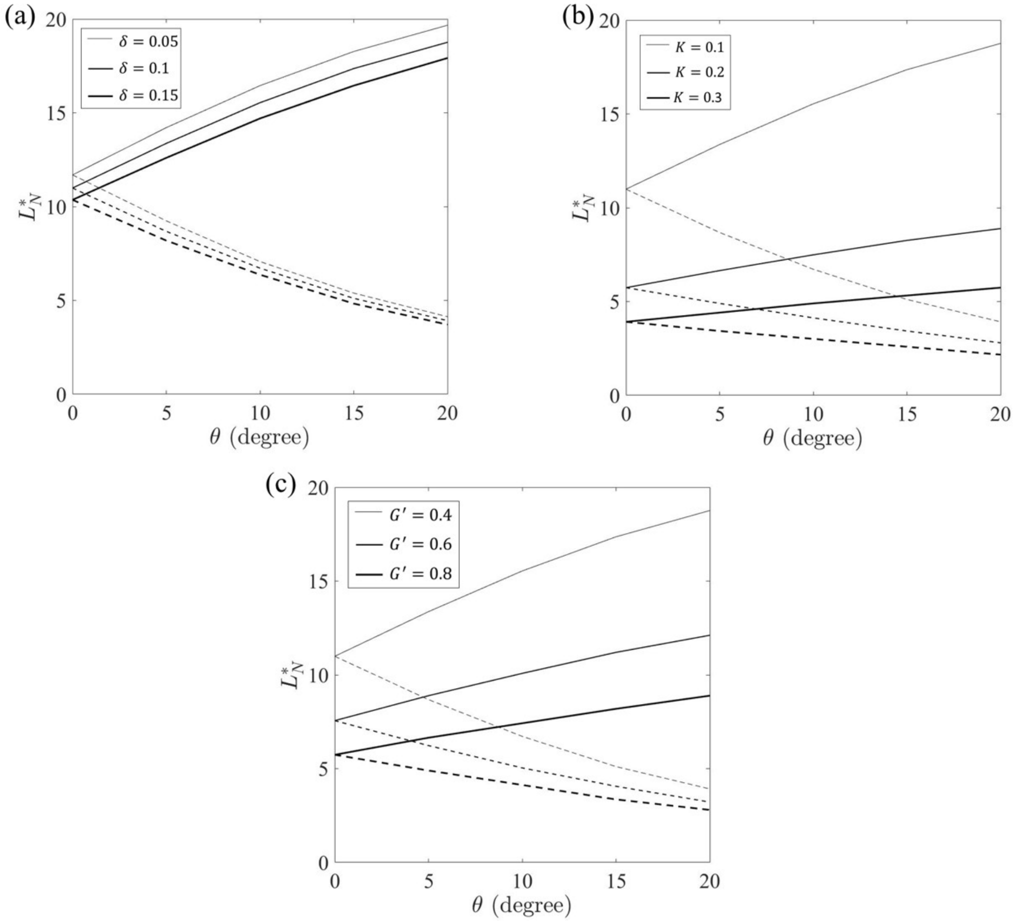

Figure 2.5: Variation of gravity current runout lengths as a function of permeability jump angle θ compared for various dimensionless parameters , i.e. (a) δ for constant $K = 0.1$ and $G' = 0.4$ (top-left panel); (b) K for constant $\delta = 0.1$ and $G' = 0.4$ (top-right panel); and (c) G' for constant $\delta = 0.1$ and $K = 0.1$ (bottom-center panel). Up- and downdip runout lengths are shown with the dashed and solid lines, respectively.

focused on the case of a horizontal permeability jump. The asymmetry that follows from setting $\theta > 0°$ is evident not only in figure 2.3a, but also in figure 2.3b which tracks nose positions for both the up- ($x_N^* < 0$) and downdip ($x_N^* > 0$) currents for $0° \leq \theta \leq 20°$. As this latter panel makes clear, runout lengths are achieved when $t^* \gtrsim 10^2$. Meanwhile, and as is true for other permeability jump angles, the former panel confirms that the gravity current aspect ratio remains relatively modest. The implications of this observation vis-á-vis Dupuit's approximation are outlined in appendix A.3.

The asymmetry between the up- and downdip flows may be further understood by plotting the downdip flow fraction f_a as a function of time, shown in figure 2.4a. As expected, when $\theta = 0°$, f_a has fixed value of 0.5 and remains time invariant; however, for $\theta > 0°$, f_a is a monotone increasing function of time that plateaus only as runout is approached. Steady state values of f_a are plotted versus θ in figure 2.4b where a monotone increasing trend is seen.

The magnitude of the steady state runout lengths, L_N^*, for both up- and downdip flows are plotted as a function of θ in the panels of figure 2.5. When $\theta = 0°$, up- and downdip runout lengths are equal, but the disparity grows with θ. Furthermore, the influence of the other three dimensionless variables, i.e. δ, K and G', on the runout lengths are illustrated in each of the panels. Regarding figure 2.5a and the influence of δ, smaller δ is associated with larger H, smaller $\bar{\rho}_c$ and therefore (moderately) larger L_N^*. In like fashion, L_N^* increases as K decreases and the resistance to drainage increases (figure 2.5b). Finally, figure 2.5c shows that large L_N^* is also associated with small G' whereby draining is retarded and discharged plume fluid therefore propagates greater distances along the permeability jump before crossing into the lower layer.

The retention of discharged plume fluid in the upper layer is analysed by defining, as with Goda & Sato (2011) and for arbitrary time t^*, a storage efficiency E_h^*. This storage efficiency is defined as the ratio of the volume (per unit width) of the discharged plume fluid retained in the upper layer, i.e within the up- and downdip gravity currents to the total volume (per unit width) that has been discharged by the plume to the gravity currents over this same time interval. Figure 2.6 shows E_h^* for different K and G'. At early times, little of the discharged plume fluid has drained contributing to a rapid initial increase in length of the gravity currents. However, as the gravity currents approach their respective runout lengths, more of the fluid discharged by the plume drains into the lower layer and E_h^* falls more steeply. At later times, E_h^* asymptotically approaches zero.

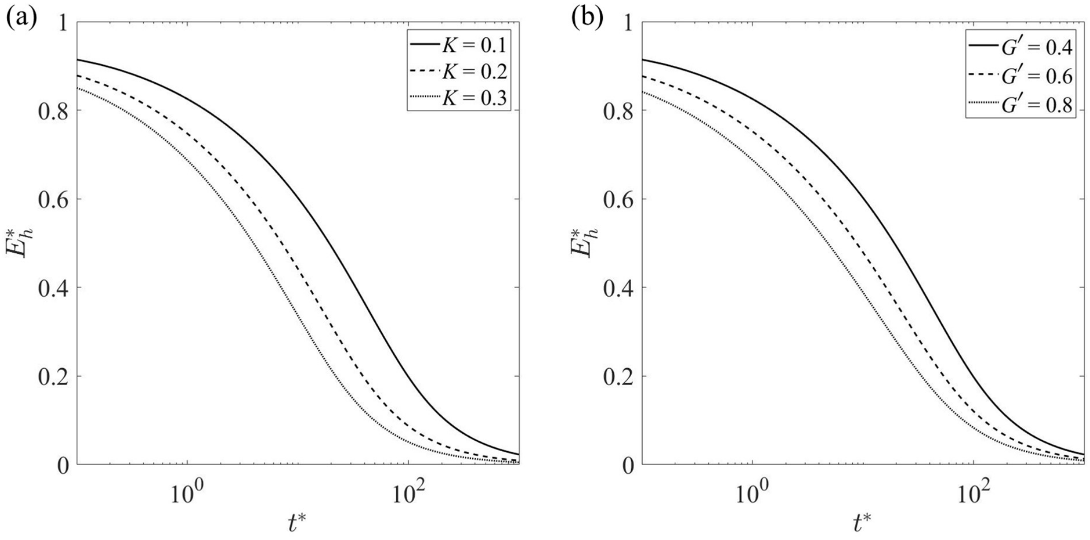

Figure 2.6: Time variation of the storage efficiency, E_h^*. The comparisons in (a) are for various K and constant values of $\theta = 15°$, $\delta = 0.1$ and $G' = 0.4$ (left panel); those in (b) are for various G' and constant values of $\theta = 15°$, $\delta = 0.1$ and $K = 0.1$ (right panel).

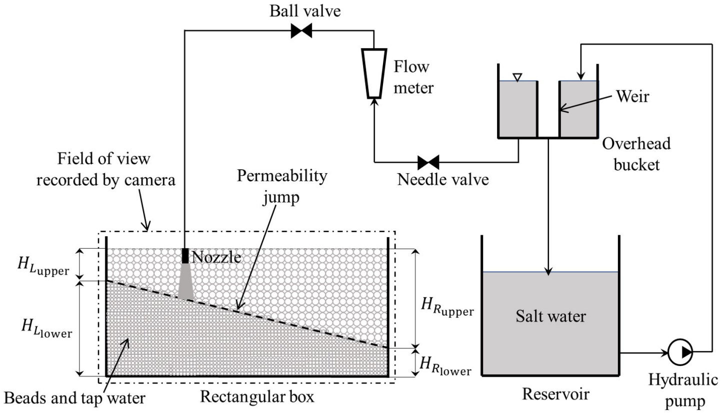

Figure 2.7: Schematic of the setup for the laboratory experiments.

2.5 Experiments

2.5.1 Experimental setup

A transparent acrylic box 118 cm long × 7.6 cm wide × 60 cm deep filled with spherical glass beads (Potters Industries A Series Premium) and tap water served as the experimental tank. Glass beads were $d_1 = 3.0 \pm 0.2\,\text{mm}$ and $d_2 = 1.0 \pm 0.2\,\text{mm}$ in diameter and were used to construct the two layer porous medium in the man-

Table 2.1: Porous media dimensions. (Notations are described in figure 2.7)

θ	Height, cm			
(degree)	$H_{L_{\text{upper}}}$	$H_{L_{\text{lower}}}$	$H_{R_{\text{upper}}}$	$H_{R_{\text{lower}}}$
0	26.0	22.0	26.0	22.0
5	21.3	26.7	31.5	16.5
10	16.0	32.0	36.6	11.4
15	8.6	39.4	40.0	8.0

Table 2.2: Conditions at the plume source.

Flow combination	Q_s	g'_s	F_s
	(cm^3/s)	(cm/s^2)	(cm^3/s^3)
1	0.51 ± 0.02	20.1 ± 1.0	1.3 ± 0.2
2	0.51 ± 0.02	80.2 ± 1.0	5.3 ± 0.2
3	1.02 ± 0.02	20.1 ± 1.0	2.6 ± 0.2
4	1.02 ± 0.02	80.2 ± 1.0	10.6 ± 0.2

ner depicted in figure 2.7, with the larger beads in the upper layer and the smaller beads in the lower layer. The beads had a density of $1.54\,\text{g/cm}^3$ as compared to $\rho_o = 0.998\,\text{g/cm}^3$ for the tap water. The porosity of the tank was measured and found to be $\phi = 0.38 \pm 0.05$. Permeabilities were determined based on the empirical relationship proposed by Kozeny and Carman, which is discussed in Dullien (1979), i.e.

$$k_i = \frac{d_i^2 \phi^3}{180(1-\phi)^2}$$

where d is the diameter of beads with index $i = 1,\ 2$. For all experiments conducted here, the value of the permeability ratio, $K = k_2/k_1 \propto d_2^2/d_1^2$ was kept fixed at 0.11.

As depicted in figure 2.7, source fluid was supplied at the top of the upper layer using a line nozzle that spanned the tank width. The nozzle was designed in such a manner that it produced a uniform flow along its length even at small flow rates (Roes, 2014). For all of the experiments to be reported upon below, the nozzle was located at the center of the tank and at a vertical height of $H = 18.3\,\text{cm}$ from the permeability jump. Shown in table 3.1 are the different values of θ used and the corresponding maximum and minimum layer heights of the upper and lower layers.

Dense source fluid supplied through the nozzle was prepared by mixing a precalculated mass of salt into tap water in a 100 L reservoir, whose density was measured to an accuracy of $0.00005\,\text{g/cm}^3$ using an Anton Paar DMA 4500 density meter. Moreover, for the purpose of flow visualization, a small amount of cold-water dye (Procion MX) was added to the salt-water in the reservoir. The dye concentration (determined from the calibration curves of Appendix A.4.1) was small enough that it did not significantly alter the plume source density. The dyed, salt-water was then pumped into an overhead bucket using a hydraulic pump (Little Gaint Pump Co.). The bucket contained a cylindrical weir that helped to maintain a constant hydrostatic pressure. Moreover, a manual flow control valve and a flow-meter (Gilmont GV-2119-S-P) were used to ensure a constant flow rate through the nozzle.

2.5.2 Experimental parameters and flow visualization

Experiments were conducted for four permeability jump angles as listed in table 3.1 and four source conditions as listed in table 2.2. For each jump angle, all four source conditions were considered such that we performed 16 experiments in total. It took approximately 1 hour for each experiment to complete.

For flow visualization, experimental images were captured using a Canon Rebel EOS T2i 18.0 PM with an 18-55 mm IS II zoom lens, which collected images every 30 s. Uniform intensity back-lighting was achieved using a 3M 1880 overhead projector and by covering the backside of the acrylic box with tracing paper, which served to diffuse the incoming light. The images captured were standard RGB, 720×400 pixels in size and had a resolution of 72 dpi. They were post-processed in MATLAB where all of the images corresponding to a particular experimental set were first cropped to remove unwanted regions outside of the flow domain. The images were then corrected by

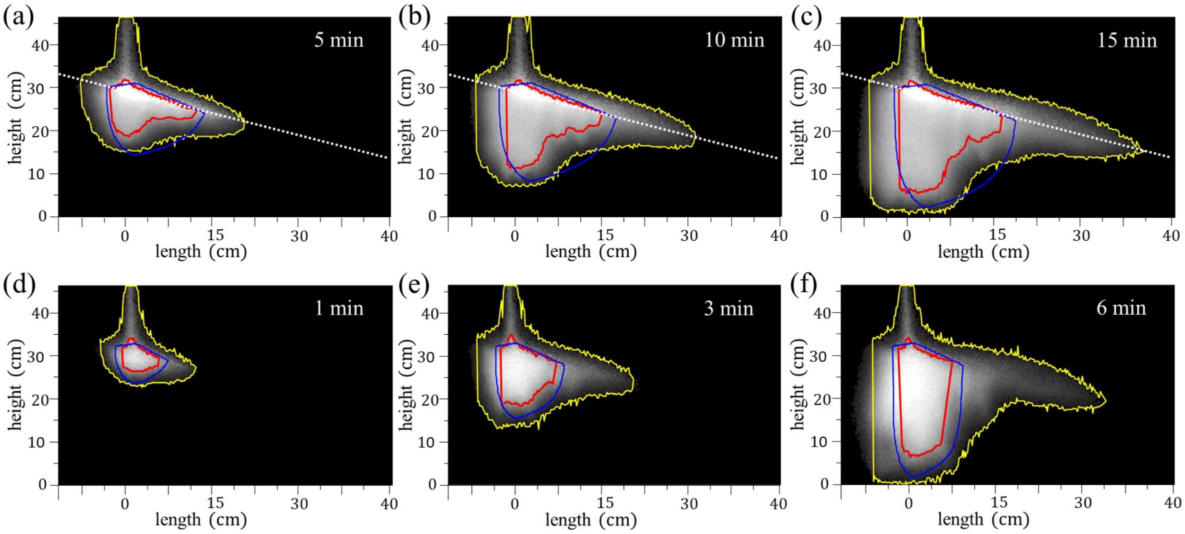

Figure 2.8: [Color] False-color experimental images showing discharge along, and draining through, the permeability jump, which here makes an angle $\theta = 15°$ to the horizontal. Panels (a-c) corresponds to flow combination 3 and panels (d-f) correspond to flow combination 4 – see table 2.2. Red, blue and yellow contours are as described in the text. The significance of the dotted lines drawn along the permeability jump in each of panels (a-c) is explained in relation to the ITS plot of figure 2.9 below.

subtracting away the reference image (collected before the initiation of flow) to remove any systematic spatial variations in the light intensity. Finally, the images were converted to false-color and the pixel intensities were normalized and so ranged from 0 to 1. Images so processed were then compared to categorize various experimental phenomena.

2.5.3 Experimental observations and interface detection

For qualitatively analyzing the experimental results, comparison is made between results obtained with $\theta = 15°$ and a source flow rate of $Q_s = 1\,\text{cm}^3/\text{s}$, but exhibiting two different source reduced gravities – $g'_s = 20\,\text{cm/s}^2$ and $80\,\text{cm/s}^2$ – corresponding to flow combinations 3 and 4, respectively from table 2.2. Representative snapshot images are presented in figure 2.8a-c for $g'_s = 20\,\text{cm/s}^2$ and figure 2.8d-f for $g'_s = 80\,\text{cm/s}^2$. As expected, the plume, after striking the permeability jump, propagated

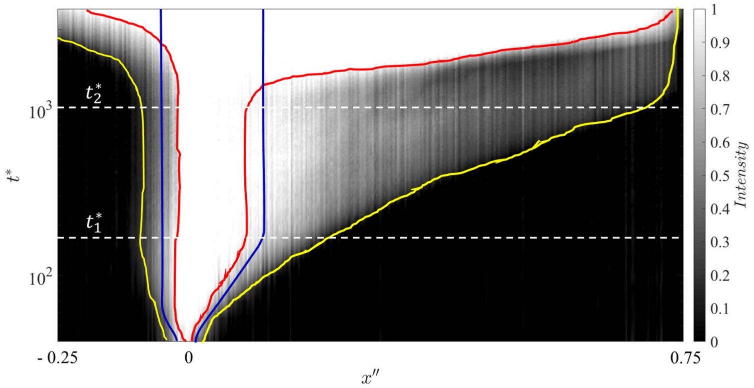

Figure 2.9: [Color] Inclined time series (ITS) image for the experiment considered in figure 2.8a-c. The red contour shows the nose position of the bulk interface whereas the yellow contour shows the nose position of the dispersed interface. The normalized intensity bar indicated at right shows the transition from pure discharged plume fluid (intensity of 1) to pure ambient fluid (intensity of 0). Time intervals are marked by the horizontal dashed lines to identify different stages of the flow dynamics, which are described in text. The analogue theoretical prediction is indicated by the blue contour.

as an asymmetric pair of gravity currents while simultaneously draining into the lower layer. From our previous discussion, we anticipate that the discharged plume fluid, as it crosses the permeability jump and mixes with lower ambient fluid, will lose its sharp interface. Interestingly, figure 2.8 suggests that a similar behavior arises even in the upper layer where dispersion, not accounted for in the model of section 2.3, results in a blurring of the boundary between discharged plume fluid and ambient fluid. Motivated by this observation, two distinct interfaces were identified in all our experimental images. These are indicated by the red and yellow contours and are defined as the bulk and dispersed interfaces, respectively. (Our method for determining the precise shape of the bulk and dispersed interface is described below.) Within the bulk interface, the pixel intensity is both high and very nearly uniform in space and time. Because pixel intensity is a surrogate for fluid density, we surmise that the density (or reduced gravity) of the fluid within the red contour, which we shall refer to as the bulk fluid, is also approximately uniform. Conversely, the dispersed interface separates the ambient fluid from either discharged plume fluid or from contaminated fluid that has been more substantially diluted through process of dispersion[5]. The region in between the bulk and dispersed interfaces shows a non-trivial variation of pixel intensity, suggesting a reduced gravity that varies, not always monotonically, in space. In turn, the fluid located between the red and yellow contours is referred to as the dispersed fluid. Note finally that the bulk interface or red contour was defined by considering pixels having an intensity of 0.85. Meanwhile, the dispersed interface or yellow contour was defined by considering pixels having an intensity of 0.005. These threshold values were chosen such that they gave consistent results while processing all our experimental images[6].

In order to analyze the bulk and dispersed interfaces in greater detail, we plot an inclined time series (ITS) image, which is, in turn, derived from snapshot images. An example appears in figure 2.9, which is constructed from 390 snapshot images collected from the experiment depicted in figure 2.8a-c. ITS images are produced by considering the time evolution of the flow along a sloping line located two to three pixels above the permeability jump. Pixel intensities along this sloping line (shown as dotted lines in figure 2.8a-c) are extracted as a function of t from the start to the end of the experiment. In figure 2.9, the abscissa, x'', is normalized by the along-jump length where $x'' = 0$ coincides with the origin indicated schematically in figure 2.2. Thus $x'' < 0$ corresponds to the updip flow while $x'' > 0$ to the downdip flow. In figure 2.9, and consistent with figure 2.8, the red and yellow contours respectively

---

[5] In miscible fluids, diffusion and dispersion are two mechanisms that lead to mixing. Diffusion arises due to the random motion of molecules and the diffusive flux acts in the direction of concentration gradient which is governed by Fick's law. By contrast, dispersion (also known as hydrodynamic dispersion) arises due to the multiplicity of possible flow trajectories within a given averaging volume and is primarily a function of flow and geometrical properties, i.e. velocity and pore size. The relative importance of dispersion and diffusion can therefore be assessed with reference to a Péclet number, defined as $\mathrm{Pe} = Ud_o/D_m$, where U is a characteristic velocity, d_o is the mean grain diameter, D_m is the molecular diffusivity (Wooding, 1963; Sahu & Flynn, 2015).

[6] Choosing threshold values below 0.005 (for dispersed interface) included too much background noise in the image due to light fluctuations, as was evident upon image subtraction. The high-level threshold of 0.85 was chosen to capture the most robust interface profile for the bulk interface. On the other hand, our results are not especially sensitive to the choice of 0.85. For example, less than a 5% difference in average densities within the contour, both in the upper and lower layer, was noted when a threshold value of 0.9 was selected.

show the nose positions of the bulk and dispersed interfaces.

The flow dynamics of the up- and downdip gravity currents are analyzed by tracking in time the position of the noses corresponding to the bulk and dispersed interfaces represented in ITS plots such as figure 2.8. Accordingly, we can describe the evolution of the flow as follows: at $t^* \equiv t/\Pi_t = 0$, plume fluid first reaches the permeability jump. For $t^* > 0$, gravity currents consisting of discharged plume fluid propagate up- and downdip and simultaneously drain into the lower layer. The nose corresponding to the bulk interface of the downdip gravity current becomes arrested at $t^* = t_1^*$ at which point the downdip runout length L_{N_d} is reached. By contrast, the updip runout length L_{N_u} is reached at an earlier point in time because L_{N_u} is often substantially less than L_{N_d} – see figures 2.3 and 2.5. For $t^* > t_1^*$ discharged plume fluid continues to drain into the lower layer during which time the noses of the bulk interface, both up- and downdip, remain fixed. Eventually, given the finite height of our experimental box, contaminated fluid makes contact with the bottom (impermeable) boundary. We designate this point in time as t_2^*. For $t^* > t_2^*$, there form a pair of secondary (horizontal) gravity currents at the base of the lower layer. The left and right propagation of these secondary-gravity currents has the effect of re-mobilizing the previously arrested gravity currents in the upper layer. In figure 2.9, for instance, such a remobilization occurs at a non-dimensional time just larger than 10^3. The associated details and dynamics of the flow post-runout are beyond the scope of the present inquiry and shall be explored in a forthcoming study. In the present analysis, all the results discussed below correspond to dimensionless times strictly below t_2^*, to ensure the contaminated fluid has not made contact with the bottom boundary.

2.5.4 Qualitative comparison between theory and experiment for the gravity current shapes

Figure 2.8 suggests that non-trivially considers different flow behaviour may be observed depending on g_s'. For $g_s' = 20\,\mathrm{cm/s^2}$, a larger volume of discharged plume fluid propagates along the permeability jump, whereas for $g'_s = 80\,\mathrm{cm/s^2}$, a larger fraction drains into the lower layer. These observations are consistent with the efficiency curves presented in section 2.4 – see figure 2.6b. This leads to longer up- and, more especially, downdip gravity currents in the former case vs. the latter. Also shown in each of the images in figure 2.8 are complementary theoretical results predicted using the (sharp interface) model of section 2.3. These are plotted as the blue contours where, consistent with the experimental measurements to be summarized in section 2.6.3, we have considered G' values of 0.43 and 0.66 in panels (a-c) and (d-f), respectively. In general, we find good correspondence with the red contours, particularly in the upper layer. However, and as we will explore in further detail in section 2.6.3, theory slightly over-predicts the length of the gravity currents, both up- and downdip. In the lower layer, the agreement is typically less robust. At least part of the reason for this discrepancy comes from the general neglect of dispersion by the analytical model which is more prominent in the lower layer because of flow instabilities. With this being the case, we cannot everywhere expect good overlap of the blue and red contours because, in practice, some non-trivial fraction of the dense fluid that drains into the lower layer is mixed into the ambient and so appears between the red and yellow contours. This is especially true in figures 2.8d-f.

2.6 Results and discussion

2.6.1 Determination of G' and α

To make quantitative predictions with the theory of section 2.3, we first need to specify the values for the reduced gravity ratio G' and the transverse dispersivity α. Finding the value of G' theoretically is challenging and we therefore adopt an empirical approach. The reduced gravity ratio was previously determined experimentally by Sahu & Flynn (2017) for the case of a horizontal permeability jump, and an average value of 0.6 ± 0.1 was reported. However, no exhaustive estimate has ever been made regarding the dependence of G' on either the source conditions or on the details of the porous medium, e.g. the magnitude of the permeability jump angle. Herein, we seek to address this shortcoming and thereby categorize the variation of G' with θ, the source volume flux, Q_s and the source reduced gravity, g_s'[7]. The value of G' is computed by taking the ratio of the reduced gravities in the lower and upper layers. The non-intrusive procedure for estimating these reduced gravities is outlined in Appendix A.4.2. On the basis of this approach, we find that G' is basically independent of time, at least for $t^* < t_2^*$. Figure 2.10 shows the variation of G' with g_s' for $\theta = 0°$, $5°$ and $15°$ and for two different Q_s, i.e. 0.5 and $1\,\text{cm}^3/\text{s}$. For prescribed Q_s, G' exhibits a monotone increasing dependence on g_s'. Meanwhile, G' values corresponding to the lower source flow rate of $0.5\,\text{cm}^3/\text{s}$ were found to exceed those corresponding to $1\,\text{cm}^3/\text{s}$. Considering separately these two source volume flow rates, we determine empirical relations of the following form:

$$\begin{aligned} G'_{0.5} &= 4.51 \times 10^{-3} g_s' - 6.03 \times 10^{-4}\theta + 0.546 \\ G'_{1} &= 3.82 \times 10^{-3} g_s' - 6.08 \times 10^{-4}\theta + 0.386 \end{aligned} \tag{2.29}$$

In both the above relations, it can be seen that G' depends much more sensitively on g_s' than it does on θ. Hence, for all practical purposes and for the range of θ values defined in table 3.1, we can, in the comparisons to follow, eliminate the θ dependence and consider G' only as a function of g_s' and Q_s.

Fortunately, it is more straightforward to estimate the value of the transverse dispersivity, α, which appears in the definition of β in (2.14), of q_c in (2.15) and of δ in (2.21), i.e. α is set by the upper layer bead diameter, d_1. From (4b) of Delgado (2007) and consistent with the range prescribed by Freeze & Cherry (1979), we take $\alpha \approx 0.025\,d_1$.

---

[7] Throughout this study, we leave the source reduced gravity, g_s' in its dimensional form. However, in the interest of non-dimensionalizing g_s', we have demonstrated the scaling of this term in Appendix A.5.

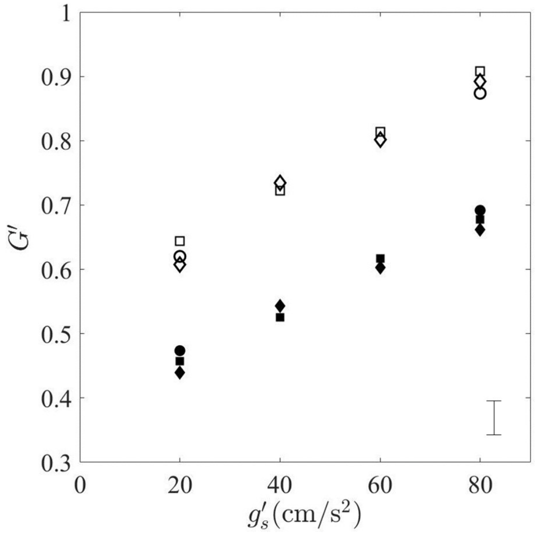

Figure 2.10: Reduced gravity ratio G' vs. the source reduced gravity g'_s. The open symbols correspond to a source flow rate of $0.5\,\mathrm{cm}^3/\mathrm{s}$ while the solid symbols consider $1\,\mathrm{cm}^3/\mathrm{s}$. The square, circle and diamond symbols show $\theta = 0°$, $5°$ and $15°$, respectively. A representative error bar is shown in the bottom-right corner.

2.6.2 Dispersion effects

To quantify the degree of dispersion from experimental snapshot images such as those of figure 2.8, and to simultaneously confirm that our methods for flow visualization account for all of the dense fluid supplied by the source, we proceed by separately calculating the buoyancy (evaluated per unit tank width) B and the area (volume per unit width) A within the bulk and dispersed phases. Suppose, for instance, that we were to evaluate the buoyancy within the bulk phase. First we would determine the area enclosed by the red contour above and also below the permeability jump. We would then multiply the two areas in question by their respective averaged reduced gravities, i.e. $(\bar{g'_c})_{\text{bulk}}$ for the upper layer and $(\bar{g'_d})_{\text{bulk}}$ for the lower layer. Symbolically,

$$B_{\text{upper,bulk}} = (A \times \bar{g'_c})_{\text{upper,bulk}} \qquad \text{and} \qquad B_{\text{lower,bulk}} = (A \times \bar{g'_d})_{\text{lower,bulk}} \tag{2.30}$$

Adding these estimates of the layer specific buoyancy allows us to estimate, from the experimental images, the total buoyancy within the bulk phase, i.e. $B_{\text{bulk}} =$

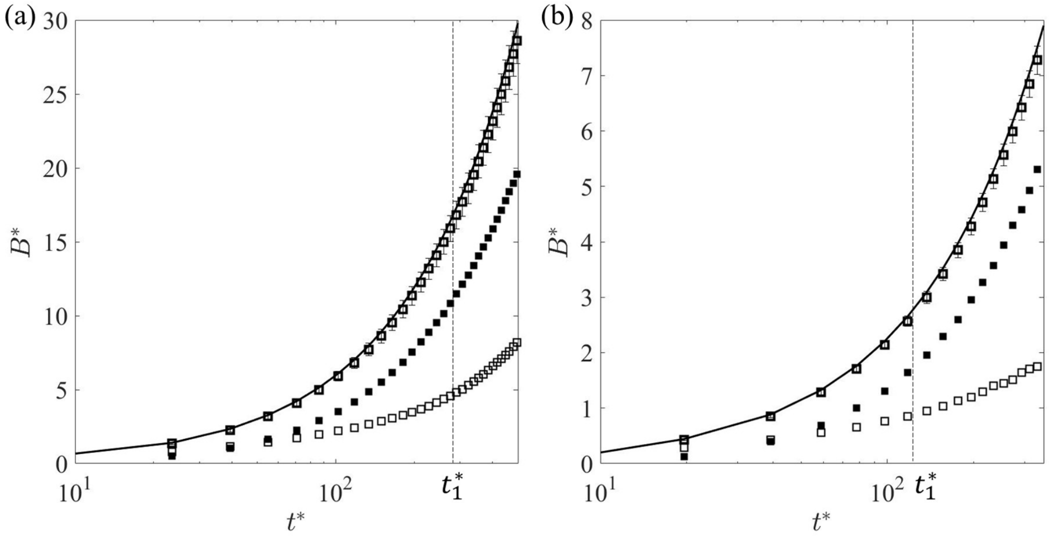

Figure 2.11: Time series of the buoyancy for flow combination 3 (panel a on the left) and 4 (panel b on the left), both for $\theta = 15°$. Thin open symbols: buoyancy within the dispersed phase (B^*_{disp}). Solid symbols: buoyancy within the bulk phase (B^*_{bulk}). Thick open symbols: total buoyancy ($B^* = B_{\text{bulk}} + B_{\text{disp}}$). For comparison, the total buoyancy as estimated from the (steady) plume source conditions is indicated by the solid line. Meanwhile the vertical dashed lines show the time when the runout length of the downdip gravity current is reached. Representative error bars are shown on the symbols for the total buoyancy.

$B_{\text{upper,bulk}} + B_{\text{lower,bulk}}$. The analogous equations for the dispersed phase read

$$B_{\text{upper,disp}} = (A \times \bar{g_c'})_{\text{upper,disp}} \qquad \text{and} \qquad B_{\text{lower,disp}} = (A \times \bar{g_d'})_{\text{lower,disp}} \tag{2.31}$$

The total buoyancy within dispersed phase is obtained from, $B_{\text{disp}} = B_{\text{upper,disp}} + B_{\text{lower,disp}}$. It is understood that, while evaluating the buoyancy within the dispersed phase, we consider only the region enclosed between the yellow and red contours. The total buoyancy is obtained by summing the constituent parts, i.e. $B = B_{\text{bulk}} + B_{\text{disp}}$. Further, we non-dimensionalize the individual buoyancies using the variables defined in (2.20) and thereby multiply by Π_t^2/Π_x^3. In figure 2.11, and considering both $g_s' = 20\,\text{cm/s}^2$ (panel a) and $g_s' = 80\,\text{cm/s}^2$ (panel b), B^* matches well the analogue value obtained directly from the conditions at the plume source, i.e. by evaluating $F_s^* \times t^*$. Figure 2.11 shows that, as expected, B^*_{bulk}, B^*_{disp} and their sum, $B^*_{\text{bulk}} + B^*_{\text{disp}}$, are all monotone increasing functions of time. Nonetheless, it is clear that the bulk phase

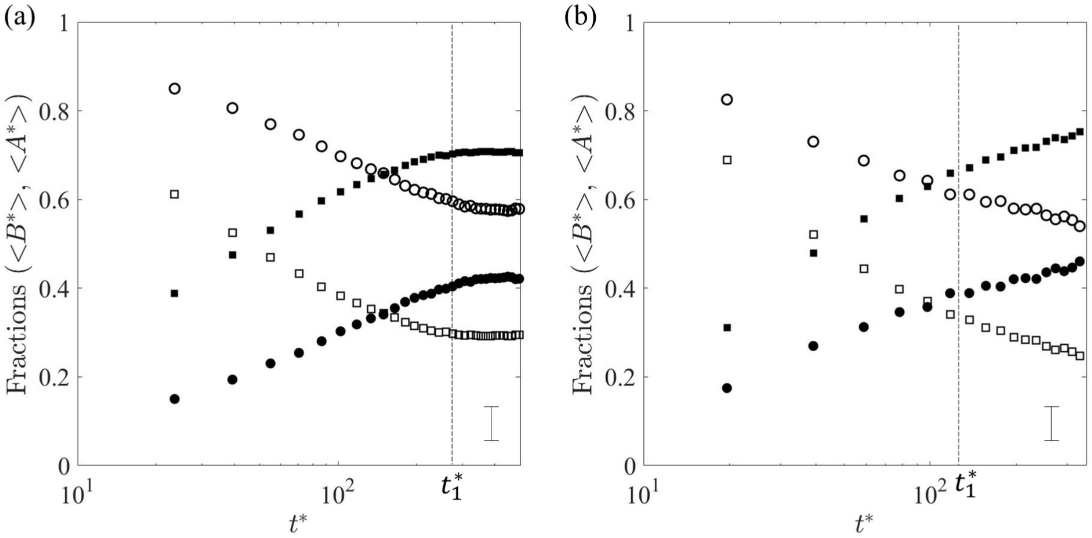

Figure 2.12: Fractions of buoyancy, <B^*> (in squares), and area, <A^*> (in circles), plotted as functions of time. Solid and open symbols correspond, respectively, to the bulk and dispersed phases. Panel (a) corresponds to flow combination 3 (left panel), while (b) corresponds to flow combination 4, both for $\theta = 15°$ (right panel). Meanwhile, the vertical dashed lines show the time when the runout length of the downdip gravity current is reached. A representative error bar is shown in the bottom-right corner in each of the panel.

retains a disproportionate share of the dense fluid within the box. To quantify matters more precisely, we make the following definitions for the buoyancy fractions:

$$<B^*_{\text{bulk}}>= \frac{B^*_{\text{bulk}}}{B^*_{\text{bulk}} + B^*_{\text{disp}}} \qquad \text{and} \qquad <B^*_{\text{disp}}>= \frac{B^*_{\text{disp}}}{B^*_{\text{bulk}} + B^*_{\text{disp}}} \tag{2.32}$$

Time-series of <B^*_{bulk}> and <B^*_{disp}> are shown as squares in figure 2.12. Results are presented for both $g'_s = 20\,\text{cm/s}^2$ (panel a) and $g'_s = 80\,\text{cm/s}^2$ (panel b). It can be seen that, except at very early times, <$B^*_{s,\text{bulk}}$> always exceeds <$B^*_{s,\text{disp}}$> and that the difference grows with time, particularly for larger g'_s. Analogous to (2.32), we also quantify the fractions corresponding to the non-dimensional area, A^*, occupied by either of the bulk or dispersed phases, i.e.

$$<A^*_{\text{bulk}}>= \frac{A^*_{\text{bulk}}}{A^*_{\text{bulk}} + A^*_{\text{disp}}} \qquad \text{and} \qquad <A^*_{\text{disp}}>= \frac{A^*_{\text{disp}}}{A^*_{\text{bulk}} + A^*_{\text{disp}}} \tag{2.33}$$

which have their terms defined implicitly in (2.30) and (2.31). Representative data appear as circles in figure 2.12. As with buoyancy, the area fractions also evolve in

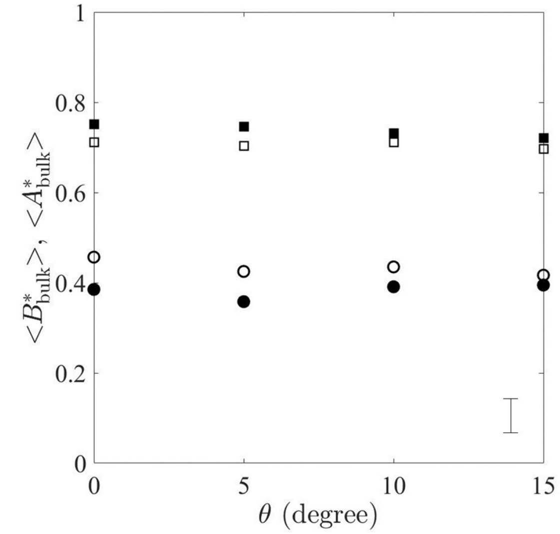

Figure 2.13: Bulk fluid buoyancy fraction $<B^*_{\text{bulk}}>$ (in squares) and area fraction $<A^*_{\text{bulk}}>$ (in circles), measured at $t^* = t^*_1$ and plotted versus the permeability jump angle θ. Solid symbols correspond to flow combination 3; open symbols correspond to flow combination 4. A representative error bar is shown in the bottom-right corner.

time. For low source reduced gravity (figure 2.12a), an asymptotic state is reached at about $t^* = t^*_1$ wherein $<A^*_{\text{disp}}>$ exceeds $<A^*_{\text{bulk}}>$. For $g'_s = 80\,\text{cm/s}^2$, no asymptotic state is achieved before t^*_2 and so the long term behaviour is less clear. Even so, and as with figure 2.12a, figure 2.12b confirms that $<A^*_{\text{disp}}>$ exceeds $<A^*_{\text{bulk}}>$ at least over the time interval of interest.

Complementing the data of figure 2.12, figure 2.13 shows the variation of the buoyancy and area fractions for the bulk phase as functions of θ. The data (and others like them, not shown) confirm that $<B^*_{\text{bulk}}>$ and $<A^*_{\text{bulk}}>$, though dependent on the source conditions, are effectively independent of θ. For all considered values of θ, it is observed that $<B^*_{\text{bulk}}> \gtrsim 0.7$, suggesting that most of the source fluid injected into the porous medium remains within the bulk phase. Figure 2.13 also suggests, however, that typical values for $<A^*_{\text{bulk}}>$ are significantly smaller, i.e. less than 0.5. This suggests that the boundary of the discharged plume fluid/contaminated fluid may extend well beyond the predictions of the sharp interface model derived in section 2.3. The implications of this observation are discussed in conjunction with figure

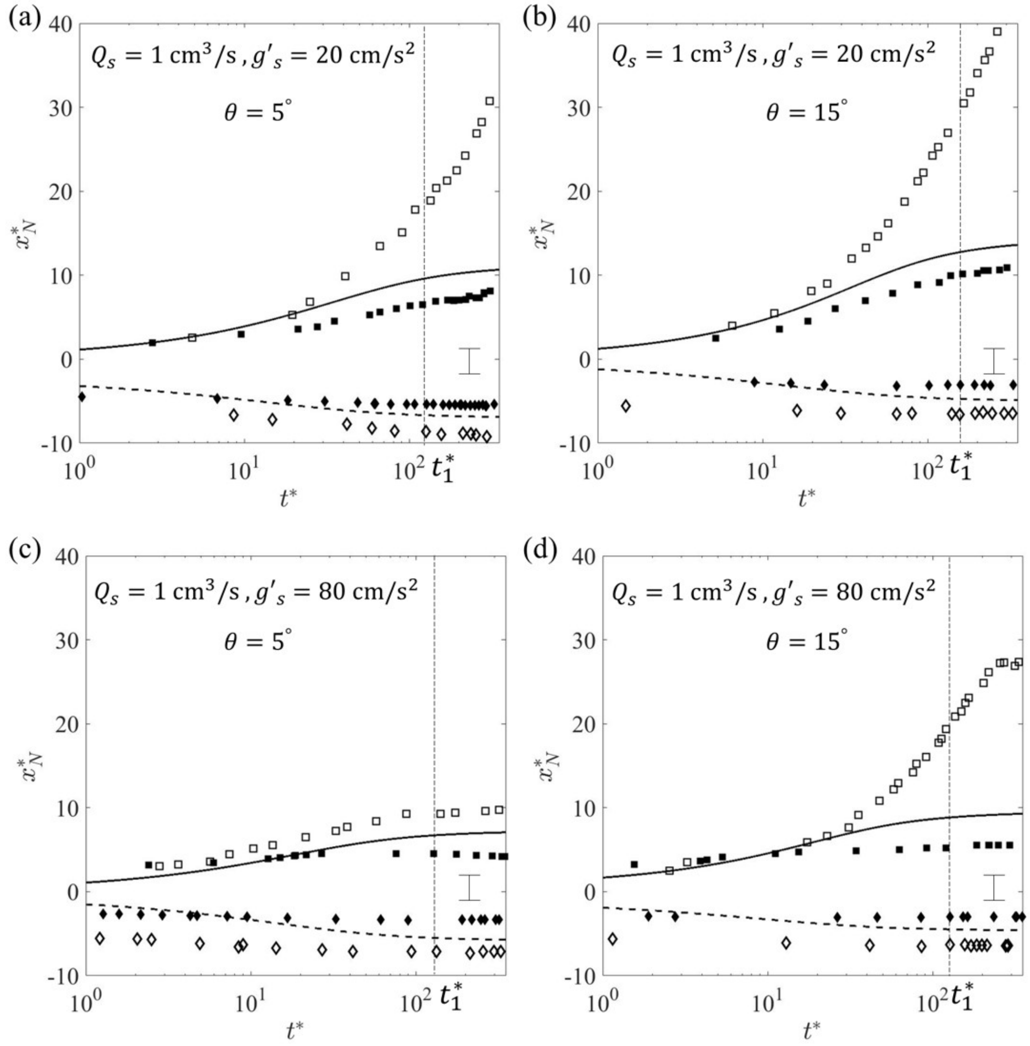

Figure 2.14: Nose propagation for up- ($x_N^* < 0$, diamonds) and downdip ($x_N^* > 0$, squares) gravity currents as functions of time. The solid symbols correspond to the bulk interface, while the open symbols correspond to the dispersed interface. Analogue theoretical results are shown by the dashed (for updip) and solid (for downdip) curves. The source conditions and permeability jump angles are as specified in each of the panels. Meanwhile, the vertical dashed lines show the time when the runout length of the downdip gravity current is reached. A representative error bar is shown in the bottom-right corner of each panel.

2.14 below.

2.6.3 Up- and downdip gravity currents: Transient and steady state analysis of the nose position

The transient nose positions corresponding to the up- and downdip gravity currents are shown in figure 2.14. Comparisons are made between two different values of θ. The panel pairs a,b and c,d respectively consider flow combinations 3 and 4. At early times, solid symbols (indicating the bulk interface) nearly coincide with the open symbols (indicating the dispersed interface). However, at later times and more especially when $t^* > t_1^*$, substantial deviations are observed as more of the dispersed fluid propagates ahead of the arrested (bulk interface) front. It is observed that the dispersion intensity and, correspondingly, the degree of spread between the solid and open symbols depends on g_s' and θ. Not surprisingly, greater spreads are observed downdip than they are updip.

Theoretical predictions of nose propagation for both up- and downdip gravity currents are also plotted in figure 2.14. In all cases, the theoretical curves typically lie between the solid and open symbols. It is evident that the theoretical predictions align better with the bulk interface. Further to figure 2.8, these observations confirm that the model of section 2.3 is generally reliable when considering the advance of the bulk interface, less so for the dispersed interface.

Comparisons between theory and experiment may also be made when the gravity currents reach their runout lengths. Figure 2.15 shows experimentally determined runout lengths attained by the bulk phase on the downdip side (solid squares) and on the updip side (solid diamonds) for a range of θ. Meanwhile the open symbols indicate the progression of the dispersed phase. Because the nose of the dispersed phase does not become arrested in the manner of the bulk phase, the open symbols specifically consider nose positions measured at $t^* = t_1^*$. The region between the bulk and dispersed noses is shaded in red on the downdip side, and in green on the updip side. The breadth of these shaded regions is a measure of the thickness of the dispersed phase at t_1^*. The panels in figure 2.15 also include analogue theoretical predictions.

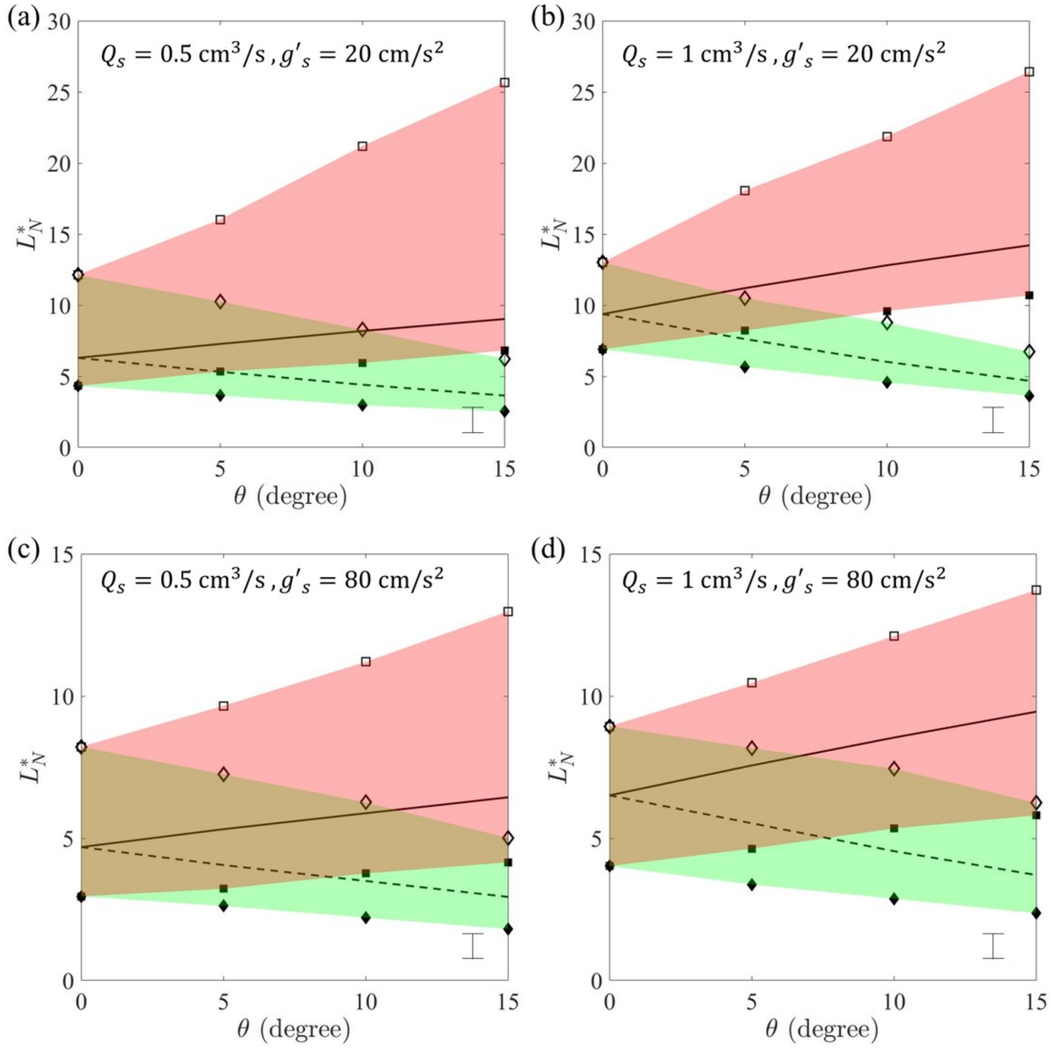

Figure 2.15: [Color] Gravity current runout lengths, L_N^* , plotted vs. θ. Up- and downdip results are respectively indicated by solid symbols in diamonds and squares. Also shown (by open symbols) are the positions of the nose of the dispersed phase, measured at $t^* = t_1^*$. The region between the solid and open symbols are filled with green and red, respectively, for the up- and downdip directions. Theoretical predictions are shown with the dashed (for updip) and solid (for downdip) curves. Source conditions are as specified, and a representative error bar is drawn in the bottom-right corner in each of the panels.

As expected, the up- ($L_{N_u}^*$) and downdip ($L_{N_d}^*$) runout lengths respectively show a monotone decrease and increase with θ. In all cases, the theoretical predictions lie within the (admittedly broad) shaded bands. Especially when $g_s' = 20\,\mathrm{cm/s^2}$ (panels a and b), model predictions are closer to measurements of the bulk interface. Also, and whether considering up- or downdip flow, measured runout lengths are longer when Q_s is large and g'_s is small. Theoretical predictions are in good agreement with this experimental finding.

2.7 Summary and conclusions

We have developed a mathematical model describing the propagation of gravity current flow along an inclined permeability jump in a heterogeneous porous medium consisting of two layers of different permeabilities – see figure 2.2. Convection originates from a source located at the top of the upper layer from where the dense fluid first falls vertically in the form of a plume and then, upon reaching the adverse permeability jump, divides into an unequal pair of up- and downdip gravity currents. The volume influx supplied to the gravity currents is modeled as a time dependent parameter that decreases as the up- and downdip gravity currents grow in height. The parameter f_a quantifies the fraction of discharged plume fluid going up- vs. downdip. We solve the dimensionless governing equations by defining four dimensionless parameters namely the permeability jump angle, θ, plume source factor, δ, permeability ratio, K, and reduced gravity ratio, G' – the dynamical significance of each of these parameters is emphasised in section 2.3. Note that G' is unique in that it depends on the plume source conditions and (very weakly) on θ – see (2.29). Key theoretical conclusions derived from the model predictions are as follows: (i) f_a is a monotone increasing function of time that attains a constant value when the up- and downdip gravity currents reach their runout lengths. (ii) Runout lengths depend on all four dimensionless parameters, and their relative importance in determining the magnitude of the runout length is discussed in section 2.4. For $0° \leq \theta \leq 20°$, runout lengths were predicted to occur when $t^* \gtrsim 10^2$.

To validate our theoretical model, laboratory experiments were conducted in a two-layer porous medium created using spherical beads of two different sizes. Experiments were performed for four different combinations of plume source volume flow rate and source reduced gravity (see table 2.2); also, we considered the following four different permeability jump slope angles: $\theta = 0°$, $5°$, $10°$ and $15°$. In contrast with theory which, consistent with Bear (1972); Huppert & Woods (1995); Pritchard *et al.* (2001); Goda & Sato (2011); Sahu & Flynn (2015) and many others, assumes a sharp interface, our experimental images reveal the appearance of two distinct interfaces, categorized as bulk and dispersed interfaces – see the red and yellow contours of figures 2.8 and 2.9. A careful analysis of laboratory images shows that the volume occupied by the dispersed phase may match or exceed the volume occupied by the bulk phase (figure 2.12). However, because the concentration of discharged plume fluid within the dispersed phase is often small, most ($\gtrsim 0.7$) of the fluid that originated in the plume remains behind the bulk interface (figure 2.13).

As in previous works (Huppert & Woods, 1995; Sahu & Flynn, 2015; Pegler *et al.*, 2016), the dynamics of the gravity currents were characterized by measuring their speed of advance. Here, measurements were made in both the up- and downdip directions and with reference to both the bulk and dispersed interfaces – see figure 2.14. Not surprisingly, downdip gravity currents propagated a greater distance compared to their updip counterparts anytime that $\theta > 0°$. The runout lengths are plotted as a function of θ in figure 2.15. Our theoretical model predicts runout lengths that lie between measured nose positions for the bulk and dispersed interfaces for all the experiments performed in this study. In general, theoretical predictions are closer to the bulk interface measurements than they are to the dispersed interface measurements.

Through this work we indirectly attempt to address some of the key uncertainties in the field of groundwater contamination (Khondaker *et al.*, 1990) and acid-gas injection (Bachu *et al.*, 2008*a*). These uncertainties include predicting the short- and longer-term dynamics, i.e. the transient and steady-state behaviour of a plume impinging on a leaky and sloping boundary. Equally important is to classify the respective volumes of discharged plume fluid that (i) propagate up- vs. downdip (c.f. f_a in figure 2.4), and, (ii) later experience dilution by Rayleigh-Taylor-type mixing (c.f. G' in figure

2.10) vs. dispersion (c.f. figures 2.11–2.13).

Our theoretical model is obviously constrained by a number of limiting assumptions, the relaxation of which is a topic of on-going/future study. For instance, we have assumed that the reduced gravity, g'_c, within the gravity currents evolves with plume length. However, our sharp interface model neglects the effect of mixing/dispersion across the gravity current-ambient interface (c.f. a recent work by Sahu & Neufeld (2020), who consider the dispersive interface in porous media gravity currents). Dispersion, in particular, is significant in that it allows discharged plume fluid to appear further downstream than is properly accounted for by a sharp interface model – compare e.g. the blue and yellow contours of figure 2.8. Our theoretical model furthermore assumes that the lower layer is infinitely deep. However, in the geophysical scenarios cited above, finite depth effects will be important e.g. in remobilizing a gravity current arrested at its runout length. Experiments confirming this behavior are already underway and will be reported upon in Chapter 3.

Chapter 3

Buoyant convection in heterogeneous porous media with an inclined permeability jump: An experimental investigation of filling box-type flows[1]

3.1 Abstract

We investigate experimentally the outflow that occurs when a plume of dense fluid strikes a sloping permeability jump in a saturated two-layered porous medium of finite extent. Contact of the plume with the jump results in a pair of leaky (primary) gravity currents that propagate up- and downdip. Previous studies have considered a thin or thick lower layer; here, we identify these nontrivial dynamics that arise for the intermediate thickness case. For instance, the primary gravity currents become arrested when the volume supplied by the plume matches that lost by basal draining. However, fluid draining into the lower layer will eventually contact the bottom boundary leading to the formation of secondary gravity currents. As these secondary gravity currents propagate left and right, they "tug" along the primary gravity currents causing remobilization. Of course, the motion of the primary and secondary

---

[1] Bharath, K. S. & Flynn, M. R. 2021 Buoyant convection in heterogeneous porous media with an inclined permeability jump: an experimental investigation of filling box-type flows. *J. Fluid Mech.* **924**, 1–31.

gravity currents must eventually become impeded by the sidewall boundaries leading, thereafter, to layer filling. We categorize the overall filling process as either simultaneous (upper and lower layers fill concurrently) or sequential (lower layer fills first). Factors influencing the filling mode include the permeability jump angle and the plume source conditions/location. Due to the asymmetric manner in which the upper layer fills, the plume, originally vertical, must become deflected. We categorize this deflection and identify scenarios where, somewhat counterintuitively, the plume bends towards the lower (lower permeability) layer. The significance of our measurements relative to real geophysical flows is highlighted with particular attention paid to geological sequestration and storage.

3.2 Introduction

There exist numerous geological scenarios where a dense or light source fluid is injected into a saturated, sedimentary porous medium that is, in lateral extent, either confined or effectively unconfined. In the former case, lateral boundaries may be associated with an anticlinal concave-down geometry or with sealing faults. Such boundaries are expected to exert a nontrivial influence on the evolution of the injectate be this associated with geothermal storage (MacKay, 2009; Paksoy & Beyhan, 2014), hydrogen storage (Feldmann *et al.*, 2016; Sainz-Garcia, 2017; Tarkowski, 2019), the sequestration of acid-gas in abandoned oil wells (Bachu & Gunter, 2004; Wu & Carroll, 2011) or the sequestration of supercritical CO_2 in deep saline aquifers (Torp & Gale, 2004; Ajayi *et al.*, 2019; Michael *et al.*, 2010).

For each of the above examples, a critical consideration is that of storage security, which requires, in turn, an assessment of the likelihood of injectate leakage. Such leakage may be due to inadequate seals (i.e. a geological boundary that is semi-permeable), filling a formation to capacity or leakage faults along the spreading boundary (Flett *et al.*, 2005). Our present focus is on the former instance, i.e. we consider that the bounding layer along which the injectate spreads does not altogether arrest vertical migration. Such a scenario, arises, for example, with the (albeit thin) layers of mudstone that are present within the Utsira Sand, the otherwise sandstone layer of thickness 200 m to 300 m into which supercritical CO_2 from the Sleipner project is injected (Boait *et al.*, 2012; Mouche *et al.*, 2010). The scenario in question is relevant to other examples of heterogeneous porous media e.g. the sandstone layers separated by tight inter-layers of comparable thickness considered in figure 5 of the hydrogen storage study of Feldmann *et al.* (2016). To predict the long-term fate of the injectate, it is important to predict the flow behavior along such leaky boundaries. Previous work (cited below) has emphasized the prediction of early-time dynamics such that the depth of the low permeable bounding layer is immaterial. Here, we relax this limitation and consider longer time horizons assuming bounding layers of intermediate thickness. In so doing, we demonstrate that the bounding layer depth (plus additional details such as the source conditions and inclination angle of the permeability jump) dictate the manner in which the (multi-layer) porous medium fills with injected fluid.

Common also to most of the examples cited above is that they combine the end-member states of buoyancy-driven flow, i.e. a vertical plume that, upon striking an impermeable or semi-impermeable boundary, feeds a horizontal (or nearly horizontal) gravity current. Although the plume may traverse only a modest vertical length compared to the long horizontal distances traveled by the gravity current, significant entrainment of external ambient fluid may nonetheless occur. This is especially true when the injectate and ambient fluid are miscible, e.g. a plume of H_2 rising through a cushion gas layer of CH_4 or N_2 (Feldmann *et al.*, 2016) or when the plume is deflected e.g. as a result of a background mean flow (Weaver & Wilson, 2000; Van Stempvoort *et al.*, 2013) and/or stratigraphic steering (Morgan *et al.*, 2008; Kamath *et al.*, 2012). In the idealized case where viscosity contrasts are small, the equations describing entrainment into a vertical plume are derived by Wooding (1963), this for the scenario of a deep, uniform porous medium and a diffusion-dominated Darcy flow characterized by low Péclét number, i.e. $\mathrm{Pe} \lesssim O(1)$. Sahu & Flynn (2015) present equations analogous to Wooding's but for the case $\mathrm{Pe} \gg O(1)$ in which circumstance dispersion dominates over diffusion.

In contrast to porous media plumes, more attention has been devoted to porous media gravity currents, whether these flow along boundaries categorized as impermeable (Huppert & Woods, 1995; Vella & Huppert, 2006*a*), semi-impermeable (Vella *et al.*, 2011; Farcas & Woods, 2013) or permeable (Pritchard *et al.*, 2001; Farcas & Woods, 2009; Goda & Sato, 2011). As regards the latter two scenarios, and assuming a gravity current of dense fluid, studies have sought to characterize the dynamical impact of basal draining whether due to a point sink or fissure (Neufeld *et al.*, 2009, 2011; Vella *et al.*, 2011; Farcas & Woods, 2013), edge drainage (Hesse & Woods, 2010; Rayward-Smith & Woods, 2011; Zheng *et al.*, 2013; Hagemann *et al.*, 2016) or distributed leakage (Pritchard *et al.*, 2001; Neufeld & Huppert, 2009; Woods & Farcas, 2009; Farcas & Woods, 2009; Yu *et al.*, 2017). Consistent with the preceding discussion, detailed characterizations should consider the depth of the lower layer, i.e. the layer into which fluid discharged by the gravity current drains. Arguably the simplest configuration assumes a lower layer that is infinitely deep, a case studied in precise analytical detail by Goda & Sato (2011). They examined a sharp permeability jump separating layers of comparatively large vs. small permeability. In adapting the analysis of Huppert & Woods (1995) and Pritchard *et al.* (2001), Goda & Sato (2011) derived coupled nonlinear advection equations describing the gravity current and draining flows. By solving these equations numerically, they demonstrated that gravity currents propagating along a permeability jump will eventually reach a terminal, or runout, length. Runout occurs when the influx to the gravity current matches the rate of basal draining into the lower layer (Consistent with the orientation relevant to geological sequestration, Goda & Sato (2011) assumed a buoyant gravity current traveling along the underside of a permeability jump. As such, fluid drained from the gravity current into the upper, not the lower, layer. We prefer to consider a dense gravity current so as to be consistent with numerous other studies e.g. Pritchard *et al.*

(2001); Lyle *et al.* (2005); Vella & Huppert (2006*a*); De Loubens & Ramakrishnan (2011); Sahu & Flynn (2015, 2016, 2017) and also the experiments to be reported upon in sections 3.3 to 3.5. The experiments performed in this study consider small density differences between the source and ambient fluids and, therefore, the flow remains Boussinesq everywhere in the domain. In such cases, the flow orientation, i.e. upward vs. downward, is immaterial.).

The theoretical study of Goda & Sato (2011) was broadened by later theoretical and experimental work conducted by Sahu & Flynn (2017). Sahu & Flynn (2017) made their upper and lower layers finite in horizontal and vertical extent and thereby additionally studied the timescales for layer filling by contaminated fluid. In this respect, Sahu & Flynn (2017)'s study was motivated by a desire to characterize the geological utility of "filling box" models. Originally studied in the non-porous media context (i.e. "a plume in a room"), filling box models describe the spatio-temporal evolution of buoyancy within a closed (Baines & Turner, 1969) or ventilated (Caulfield & Woods, 2002) control volume subject to localized heating or cooling. Although filling box models have been applied to problems of ocean circulation (Manins, 1979; Speer & Tziperman, 1990; Hughes & Griffiths, 2006), they have received less attention in the context of porous media flows in general and sequestration/storage flows in particular. This lack of attention is surprising given the natural ability of filling box models to describe the dynamical importance of boundaries in the context of reservoirs/aquifers.

Expanding on the study by Sahu & Flynn (2017) on porous media filling box models, we herein extend the analysis to situations of greater geological realism. For instance, a key characteristic of the experiments of Sahu & Flynn (2017) is that the permeability jump is horizontal. On the other hand, there are many instances where, in modeling real geological flows, it would be more appropriate to consider a permeability jump that is either sloping (Bachu *et al.*, 2008*a*,*b*; MacMinn *et al.*, 2010) or curved (Ajayi *et al.*, 2019). The former complication was incorporated into the recent theoretical study of Bharath *et al.* (2020). They consider up- and downdip gravity currents fed by a descending plume rather than by a source located along the permeability jump. In turn, their model captures the early time spreading dynamics by predicting the flow evolution up to the point of runout. On the other hand, the theory and laboratory experiments reported in Bharath *et al.* (2020) do not provide meaningful insights into the longer term dynamics and how these are influenced by (i) the depth of the lower layer, and, (ii) the presence of sidewall boundaries. To this end, the experiments described in this study provide an especially interesting vantage point from which to study filling box dynamics because of the appearance of primary *and* secondary gravity currents. These arise, respectively, along the permeability jump and along the bottom (impermeable) boundary. The relative motion of the primary vs. secondary gravity currents was ignored by Sahu & Flynn (2017) but has, as we shall see, a crucial influence on the manner in which the heterogeneous porous medium becomes filled with contaminated fluid. Because medium filling is closely related to medium storage efficiencies and the long-term fate of the injectate, it is important to be able to characterize the manner and speed with which the lower vs. upper layers are filled. Addressing such topics is a further objective of this study.

Throughout, we pursue an experimental approach and examine the evolution of the flow exhibited schematically in figure 3.1 a. Dense fluid, dyed for ease of visualization, is discharged by a line source and then propagates downward through the upper layer until it strikes the permeability jump. There follows drainage of discharged plume fluid into the lower layer and the formation and propagation of the primary and secondary gravity currents. Because the box in which experiments are performed is relatively thin in the spanwise direction, the flow is largely 2D, i.e. there is limited opportunity for spanwise flow instabilities to develop. In addition, the dynamic viscosities of the injected and ambient fluids are considered identical. These fluids being additionally fully-miscible, we neglect surface tension effects and assume infinitely

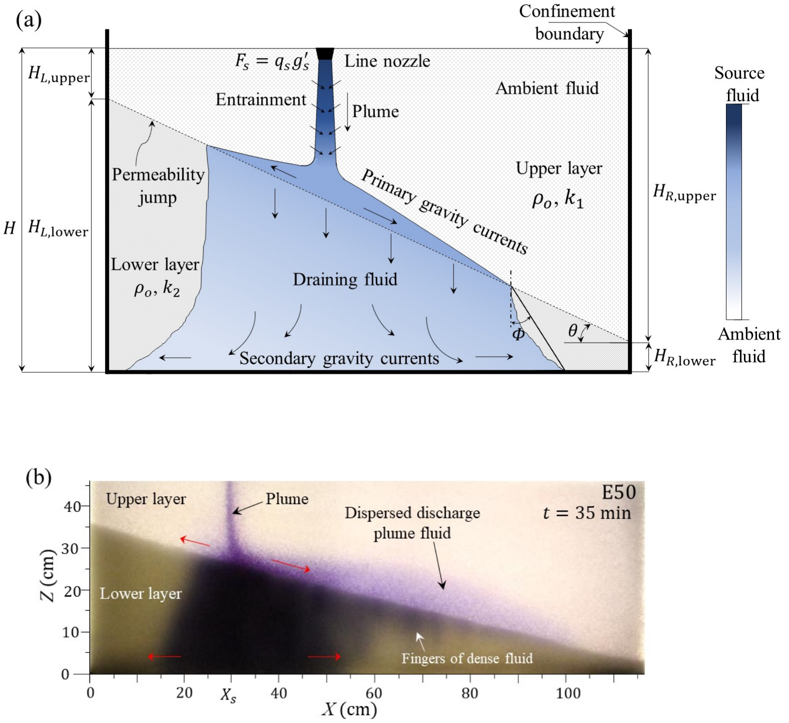

Figure 3.1: [Color] (a) Schematic showing discharged plume fluid propagating as pair of primary and secondary currents in the upper and lower layers, respectively. The colorbar indicates the variation of fluid density as the source fluid propagates through the heterogeneous porous medium. (b) Analogue snapshot image from our laboratory experiments. X_s on the horizontal axis indicate the position of the nozzle.

large values for the Bond number, which characterizes the ratio of buoyancy to capillarity. In this respect, our approach is consistent with numerous previous studies (Huppert & Woods, 1995; Rayward-Smith & Woods, 2011; Szulczewski & Juanes, 2013; Pegler *et al.*, 2016).

The rest of our manuscript is outlined as follows: in section 3.3, the experimental procedure is outlined as is our method for post-processing experimental images and analyzing the resulting measured data. In section 3.4, qualitative and quantitative analyses of the primarily horizontal flows in the upper and lower layers are made. The counterpart vertical and filling box flows are examined in section 3.5. The mutual dependence of horizontal and vertical flows during the filling process is discussed in

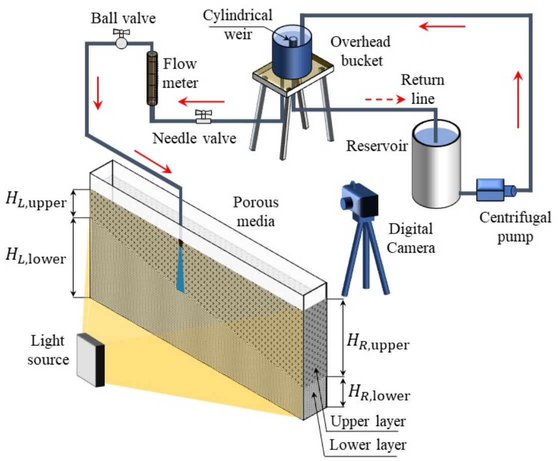

Figure 3.2: [Color] Schematic of the experimental setup.

Table 3.1: Porous media dimensions. Heights are considered accurate to within ±0.5 cm and angles are considered accurate to within ±0.2°.

θ	Height, cm			
(deg)	$H_{L,\text{upper}}$	H_{L_lower}	$H_{R,\text{upper}}$	$H_{R,\text{lower}}$
0	26.0	22.0	26.0	22.0
5	21.3	26.7	31.5	16.5
10	16.0	32.0	36.6	11.4
15	8.6	39.4	40.0	8.0

section 3.6. Finally, in section 3.7 we summarize and discuss the key findings and applications of this study.

3.3 Experimental procedure

3.3.1 Experimental setup

Experiments were performed using a transparent rectangular box of dimensions 118 cm long × 7.6 cm wide × 60 cm deep filled with spherical beads (Potters Industries A Series Premium) as shown in figure 3.2. The beads in the upper layer were $d_1 = 3.0 \pm 0.2$ mm in diameter and those in the lower layer were $d_2 = 1.0 \pm 0.2$ mm in diameter. The bead density, as specified by the manufacturer, was $1.54\,\text{g/cm}^3$. The entire porous medium was saturated with tap water having a density of approximately $\rho_o = 0.998\,\mathrm{g/cm^3}$. The layers were separated by a distinct interface, which we refer to as the permeability jump. Upper and lower layer permeabilities were determined based on the empirical relationship proposed by Kozeny and Carman, and discussed in Dullien (1979), i.e.

$$k_i = \frac{d_i^2 \phi^3}{180(1-\phi)^2}$$

where $i = 1, 2$ corresponds to the upper and lower layer, respectively. For all experiments conducted here, the value of the permeability ratio, $K = k_2/k_1 \propto d_2^2/d_1^2$ was kept fixed at 0.11. The heterogeneous medium was varied by changing the angle, θ, of the permeability jump, which, in turn, had the effect of changing the vertical distances $H_{L,\mathrm{upper}}$, $H_{L,\mathrm{lower}}$, $H_{R,\mathrm{upper}}$, $H_{R,\mathrm{lower}}$ defined schematically in figure 3.1 a and quantitatively in table 3.1. In all cases, $H_{L,\mathrm{lower}} + H_{L,\mathrm{upper}} = H_{R,\mathrm{lower}} + H_{R,\mathrm{upper}} = H = 47\,\mathrm{cm}$ where H represents the combined depth of the upper and lower layers.

As depicted in figure 3.2, dense source fluid was supplied at the top of the upper layer using a line source nozzle that spanned the tank width of 6.45 cm. The nozzle was designed in such a manner that it produced a uniform flow along its length even at small flow rates (Roes, 2014). For each of the permeability jump angles prescribed in table 3.1, experiments were performed by positioning the nozzle (source) at various horizontal locations. Using non-dimensional variables, the source location is characterized by $X_s^* = X_s/L$, where $L = 118\,\mathrm{cm}$ is the inside box length and X_s is the corresponding horizontal position of the nozzle midplane measured relative to the updip end wall. Adjusting the nozzle location allowed us to perform experiments for various effective lower layer depths and to study the influence of sidewall boundaries on the flow behavior.

Dense source fluid was prepared by mixing a precalculated mass of salt into tap water in a 100 L reservoir. The density of the resulting solution, ρ_s, was measured to an accuracy of $0.00005\,\mathrm{g/cm^3}$ using an Anton Paar DMA 4500 densitometer. Moreover, and for purposes of flow visualization, a small amount of cold-water dye (Procion MX) was added to the salt-water solution. The dye concentration (determined with reference to the calibration curves of Appendix B.2) was small enough that it did not significantly alter the plume source density. The dyed, salt-water was then pumped into an overhead bucket using a centrifugal pump (Little Gaint Pump Co., Model 3-MD). Inside of the bucket was placed a cylindrical weir whose purpose was to maintain a constant elevation of fluid inside the bucket. Fluid flowing over the weir was returned to the reservoir thereby assuring well-mixed conditions over the 3 to 5 hours of duration of each experiment. Fluid not flowing over the weir was discharged through 12.7 mm inner diameter tubing to the plume nozzle after first passing through a flow-control needle valve (0.5 inch, Swagelok SS-8GUF8), a flow meter (Gilmont GV-2119-S-P) and an on/off ball valve (0.5 inch, Kebechem). The flow parameters of interest are the source volume flux, Q_s, and the source reduced gravity, $g'_s = g(\rho_s - \rho_o)/\rho_o \ll g$, where g is gravitational acceleration. A detailed list of experimental parameters for different source conditions and porous media configurations is described in table B.1 of Appendix B.1.

3.3.2 Image capture

Experimental snapshots were captured using a Canon Rebel EOS T2i 18.0 PM with an 18-55 mm IS II zoom lens, which collected images every 30 s. Uniform intensity backlighting was achieved using a 3M 1880 overhead projector, whose head was situated at the box center, i.e. at respective horizontal and vertical distances of 60 cm and 25 cm from the box lower left hand corner. The projector was located 150 cm behind the box. The backside of the box was covered with tracing paper, which served to diffuse the incoming light. Images captured using the Canon Rebel camera were standard RGB, 720×400 pixels in size and had a resolution of 72 dpi. They were post-processed in MATLAB where all of the images corresponding to a particular experimental set were first cropped to remove unwanted regions outside of the flow domain. The images were then corrected by subtracting away a reference image (collected before

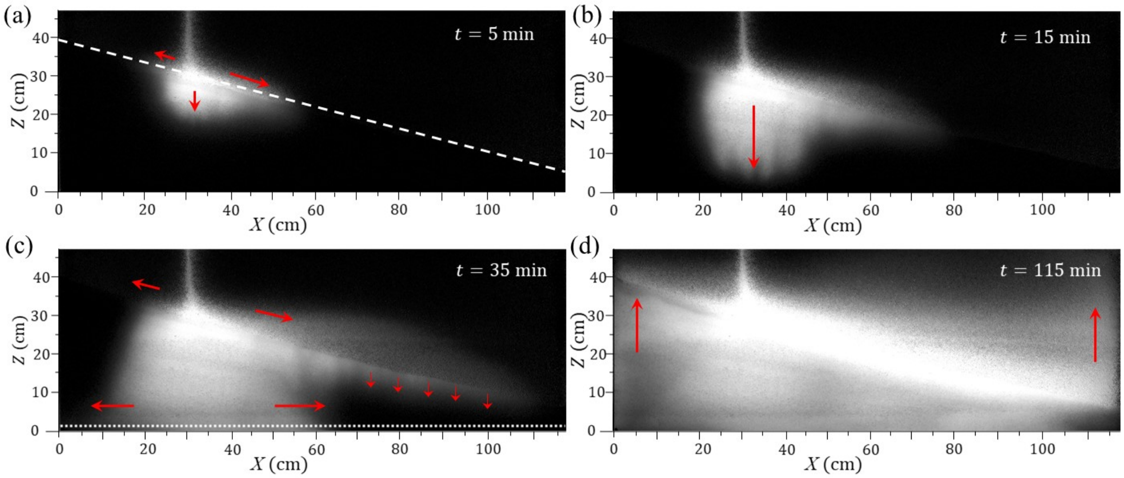

Figure 3.3: [Color] Snapshot images (false-color) for $\theta = 15^\circ$ with source conditions $Q_s = 1.01 \pm 0.02\,\mathrm{cm}^3/\mathrm{s}$ and $g_s' = 20.1 \pm 0.9\,\mathrm{cm/s}^2$ illustrating the time evolution of a canonical experiment. (a) Fluid discharged by the plume propagates as a pair of up- and downdip primary gravity currents and also drains into the lower layer. (b) A greater fraction of the discharged plume fluid drains into the lower layer as the primary gravity currents approach their respective runout lengths. (c) Formation of secondary gravity currents following contact by the draining fluid with the bottom (impermeable) boundary. The remobilization of the primary gravity currents occurs thereafter. (d) Vertical advection of discharged plume fluid towards the source, which occurs after the primary and secondary gravity currents reach the box sidewalls. The filling process is characterized by a “first front” that separates contaminated fluid (below) from uncontaminated ambient fluid (above). In all panels, arrows show the dominant flow directions. The dashed line of (a) and the dotted line of (c) respectively indicate the lines along which ITS (e.g. figure 3.4 a) and HTS (e.g. figure 3.4 b) images are collected.

the initiation of flow). This step removed any systematic spatial variations in the light intensity e.g. due to some localized “dark spot” within the bead pack. Finally, images were converted to false-color and the pixel intensities were normalized so that they ranged from 0 to 1.

3.3.3 Analysis of snapshot and time series images

A true color snapshot of an experiment with $\theta = 15^\circ$ is shown in figure 3.1 b. The source conditions measure $Q_s = 1.01 \pm 0.02\,\mathrm{cm}^3/\mathrm{s}$ and $g_s' = 20.1 \pm 0.9\,\mathrm{cm/s}^2$ – see E50 in table B.1. Figure 3.3 shows a sequence of false-color snapshot images for this case. The source fluid from the nozzle descends as a negatively buoyant plume from the

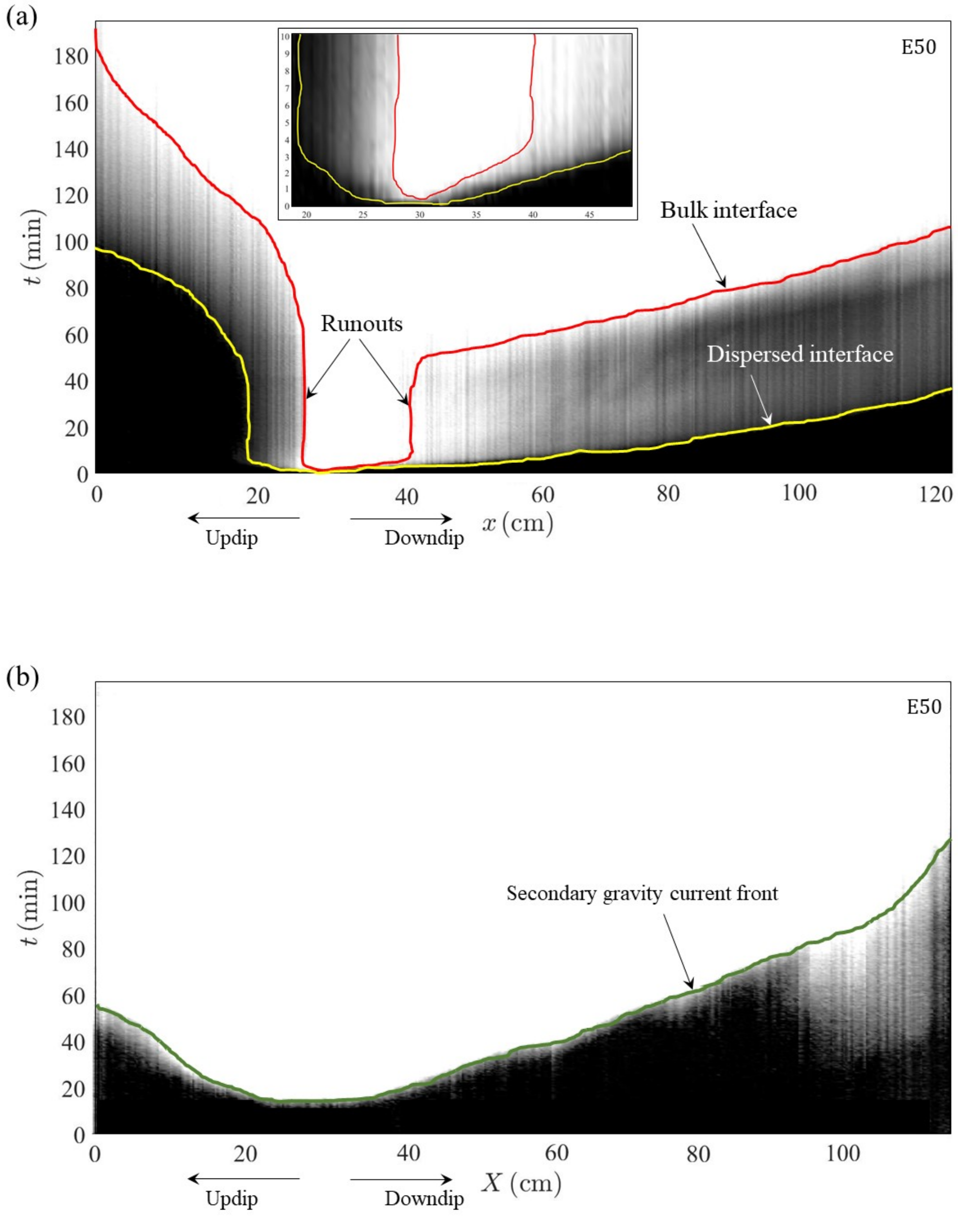

Figure 3.4: [Color] (a) Inclined time series (ITS) image and (b) horizontal time series (HTS) image, constructed from 390 snapshot images corresponding to the experiment of figure 3.3 and used to analyze the up- and downdip propagation of the primary and secondary gravity currents. The meaning of the red and yellow contours in (a) and of the green contour in (b) is explained in the text. The inset figure in (a) illustrates the flow behavior at early times.

nozzle. The plume fluid, upon striking the permeability jump, propagates either up- or downdip as a leaky gravity current or else drains directly into the lower layer, as shown in figure 3.3 a. The along-slope flow dynamics of the primary gravity currents are studied by plotting the nose positions, both up- and downdip, as functions of time. Facilitating this process, we construct inclined time series (ITS) images using the methodology summarized in Bharath *et al.* (2020). In brief, a diagonal line of slope $\tan\theta$ is drawn two or three pixels above the permeability jump. From the sequence of snapshot images, we then track the change of pixel intensity along this diagonal line, a process that results in ITS images such as that of figure 3.4 a. In contrast to the snapshot images of figure 3.3, which make reference to horizontal (X) and vertical (Z) coordinates, ITS images measure the flow evolution with reference to an along-slope coordinate, $x = X/\cos\theta$. Note that, in figure 3.4 a, $x_s = 25.9\,\text{cm}$ is defined to coincide with the location of the nozzle (located at $X_s = 25.0\,\text{cm}$) so that $x_s < 25.9\,\text{cm}$ and $x_s > 25.9\,\text{cm}$ correspond, respectively, to the up- and downdip directions.

Figure 3.4 a is derived from figure 3.3 and includes two contour lines. The red contour corresponds to the primary gravity current "bulk interface", and indicates the boundary above which the pixel intensity is both large and nearly uniform in space and time. As described in quantitative detail in Appendix B.2, we consider the solute concentration to be a direct function of the dye concentration. Because the solute concentration is a surrogate for the fluid density, we surmise that the density (or reduced gravity) of the fluid above the red contour is approximately uniform. We refer to the fluid appearing above the red contour as the bulk fluid. Conversely, the yellow contour of figure 3.4 a is referred to as the "dispersed interface"; it separates uncontaminated ambient fluid (having a pixel intensity at or near zero), from contaminated fluid consisting of discharged plume fluid that has been substantially diluted through process of dispersion – c.f. Sahu & Neufeld (2020). The red and yellow contours of figure 3.4 a were defined by considering pixel intensity thresholds of 0.85 and 0.005, respectively. These threshold values give consistent results when considering the entirety of our experimental data set. The region between the red and yellow contours shows a non-trivial variation of pixel intensity, suggesting that the density variation is non-monotone in both space and time. The associated mixing is due to the fact that the interface is not, as is often assumed in theory (Goda & Sato, 2011), sharp but rather miscible. As such, molecular diffusion and, more importantly, hydrodynamic dispersion causes a “smearing” of the solute concentration in the vicinity of the interface. In particular, longitudinal dispersion is especially important as the (downdip) gravity current speed increases. We refer to the fluid impacted by dispersion, i.e. the fluid located between the red and yellow contours, as dispersed fluid.

For sufficiently large lower layer depths, the noses of the up- and downdip primary gravity currents reach their respective runout lengths, as indicated by the snapshot image of figure 3.3 b. In the interest of quantifying the runout lengths corresponding to each of the interfaces identified above we refer to the ITS image in figure 3.4 a. The red contour becomes vertical at the point where the bulk interface reaches runout. A similar trend is observed for the dispersed interface except that here, runout is achieved only on the updip side. Not surprisingly, the gravity current nose corresponding to the bulk interface on the downdip side travels a greater distance than does its updip counterpart as illustrated in the inset of figure 3.4 a. By contrast, the updip flow achieves runout in less time.

The phenomenon of runout, whereby the volume of fluid supplied to the (primary) gravity current(s) is balanced by basal draining has been previously reported by numerous other researchers (Pritchard *et al.*, 2001; Goda & Sato, 2011; Sahu & Flynn, 2017; Bharath *et al.*, 2020). Notable in this study is that the draining fluid does not fall indefinitely. Rather, and as illustrated in figure 3.3 c, it eventually strikes the lower (impermeable) boundary leading to the formation of a pair of secondary gravity currents. To analyze the flow dynamics of these secondary gravity currents, we construct horizontal time series (HTS) images, as shown in figure 3.4 b. HTS images are constructed by considering the temporal variation of pixel intensity along a horizontal line located two or three pixels above the bottom boundary (see the dotted lines in figure 3.3 c). In contrast to the (dispersive) primary gravity currents, the noses of the secondary gravity currents are tracked using a single interface, considering a pixel intensity threshold of 0.85 which is indicated as the green contour in figure 3.4 b.

Also apparent in figure 3.4 b is evidence of basal draining, which presents as the patch of relatively bright pixels below the green contour for $X \gtrsim 90\,\mathrm{cm}$. The relative importance to lower layer filling of basal draining vs. secondary gravity current advection depends on the experimental parameters, most especially θ, g_s' and X_s. To this end, note that basal draining is often slow but the vertical distances involved may be relatively short. The horizontal advection speed may be larger by comparison but secondary gravity currents often travel long distances depending on the horizontal location of the plume source. When, as in figure 3.3, θ is relatively large and g_s' is small, the (downdip) primary gravity current experiences nontrivial dispersion. The resulting dispersed fluid likewise flows downdip and reaches the (right) sidewall well ahead of the secondary gravity current leading to the draining pattern evident in figure 3.4 b. The dispersed fluid in question can also move upwards, i.e. from figure 3.3 d we note the formation in the upper layer of a vertically ascending "first front". The formation of this first front represents the beginning of the filling process for the upper layer. Because upper layer filling initiates before the filling of the lower layer is complete, we categorize the experiment of figures 3.3 and 3.4 as an example of *simultaneous* filling. By contrast, *sequential* filling arises when the nose of the secondary gravity current reaches the sidewall boundary well before the nose of the primary gravity current. A precise method for distinguishing between cases of simultaneous vs. sequential filling is discussed in Appendix B.4.

3.3.4 Length and time scales

Whereas the discussion thus far has emphasized dimensional variables, it is advantageous to define characteristic spatial and temporal scales to non-dimensionalize the parameters of interest. For the primary and secondary gravity currents, characteristic length and time[2] scales are respectively defined as

$$S_X = L \qquad \text{and} \qquad T_X = \frac{q_c}{\phi\beta^2} \tag{3.1}$$

where L is the box length. In (3.1), the plume volume flux, q_c, evaluated at the permeability jump is given by (2.24) of Sahu & Flynn (2015), i.e.

$$q_c = \Big[\Big(\frac{16F_s k_1}{\pi\nu}\Big)^2 \phi\alpha(\hat{H} + Z_s)\Big]^{1/4} \tag{3.2}$$

and for along-slope flows, the velocity factor is given by $\beta = (k_1 g'_c)/\nu$ (Huppert & Woods, 1995). The reduced gravity, g'_c, evaluated at the permeability jump is given by (2.25) of Sahu & Flynn (2015). More formally, therefore, β is given by

$$\beta = \frac{k_1}{\phi\nu}\Big[\Big(\frac{\pi F_s \nu}{16k_1}\Big)^2 \frac{1}{\phi\alpha(\hat{H} + Z_s)}\Big]^{1/4} \tag{3.3}$$

In the above equations, $\hat{H} = H_{L,\text{upper}} + X_s \tan\theta$ is the vertical distance between the plume source and the permeability jump. Also, the source buoyancy flux per unit width is $F_s = q_s g'_s$, where q_s is the source volume flux per unit nozzle width. Moreover, the finite source correction term,

$$Z_s = \frac{1}{\phi\alpha}\Big(\frac{\pi\nu}{16F_s k_1}\Big)^2 q_s^4$$

is evaluated with reference to q_s and the kinematic viscosity, ν. From (4b) of Delgado (2007), and accounting for the fact that the plume is dispersion-dominant for all the experiments in this study, we take the transverse dispersivity to be $\alpha \approx 0.025d_1$ in

---

[2] The time scales processes occuring post-remobilization are different from that corresponding to early-time spreading. On the other hand, and for the sake of plotting and comparing the results related to both early- and late-time dynamics in the same plot, we adopt the early-time time scale for non-dimensionalizng parameters related to the motion of the gravity currents (both in the upper- and lower-layers) and the draining flows.

which d_1 is the mean diameter of the beads in the upper layer. Finally, a porosity of $\phi = 0.38$ is assumed corresponding to beads that are randomly distributed (Happel & Brenner, 1983).

For the filling box analysis, a different pair of characteristic length and time scales must be considered. These are

$$S_Z = H \qquad \text{and} \qquad T_Z = \frac{\phi L H}{q_s} \tag{3.4}$$

respectively, where H is the total height of the porous media. Note that, T_Z corresponds to the residence time based on the plume source volume flux and the porous medium void volume.

In the discussion to follow, a separate notation will be employed when non-dimensionalizing time (t) with T_X vs. T_Z. More specifically, we shall write $t^* = t/T_X$ and $\hat{t} = t/T_Z$.

3.4 Gravity current analysis

3.4.1 Primary vs. secondary gravity currents, qualitative comparison

In order to characterize the behaviour of the gravity currents in the upper and lower layers, it is helpful to contrast the evolution of nose position as shown in figure 3.5. Figures 3.5 a,b correspond to $g'_s = 20.1 \pm 0.9\,\text{cm/s}^2$ (the same experiment shown in figure 3.3) and figures 3.5 c,d correspond to $g'_s = 80.1 \pm 0.9\,\text{cm/s}^2$. In both cases, $\theta = 15°$ and $Q_s = 1.01 \pm 0.02\,\text{cm}^3/\text{s}$ – see E50 and E58 of table B.1. Although the primary gravity currents propagate along the sloping permeability jump, for the purposes of drawing an even dynamical comparison figure 3.5 resolves the flow of the primary (and secondary) gravity currents relative to the horizontal coordinate, X. In turn, the horizontal and vertical axes of figure 3.5 are respectively non-dimensionalized using the characteristic length and time scales defined in (3.1). In the former case, we set $X^* = (X - X_s)/L$, such that $X^* = 0$ indicates the plume source location. Thus $X^* < 0$ corresponds to the updip side (figures 3.5 a,c) and $X^* > 0$ corresponds to the

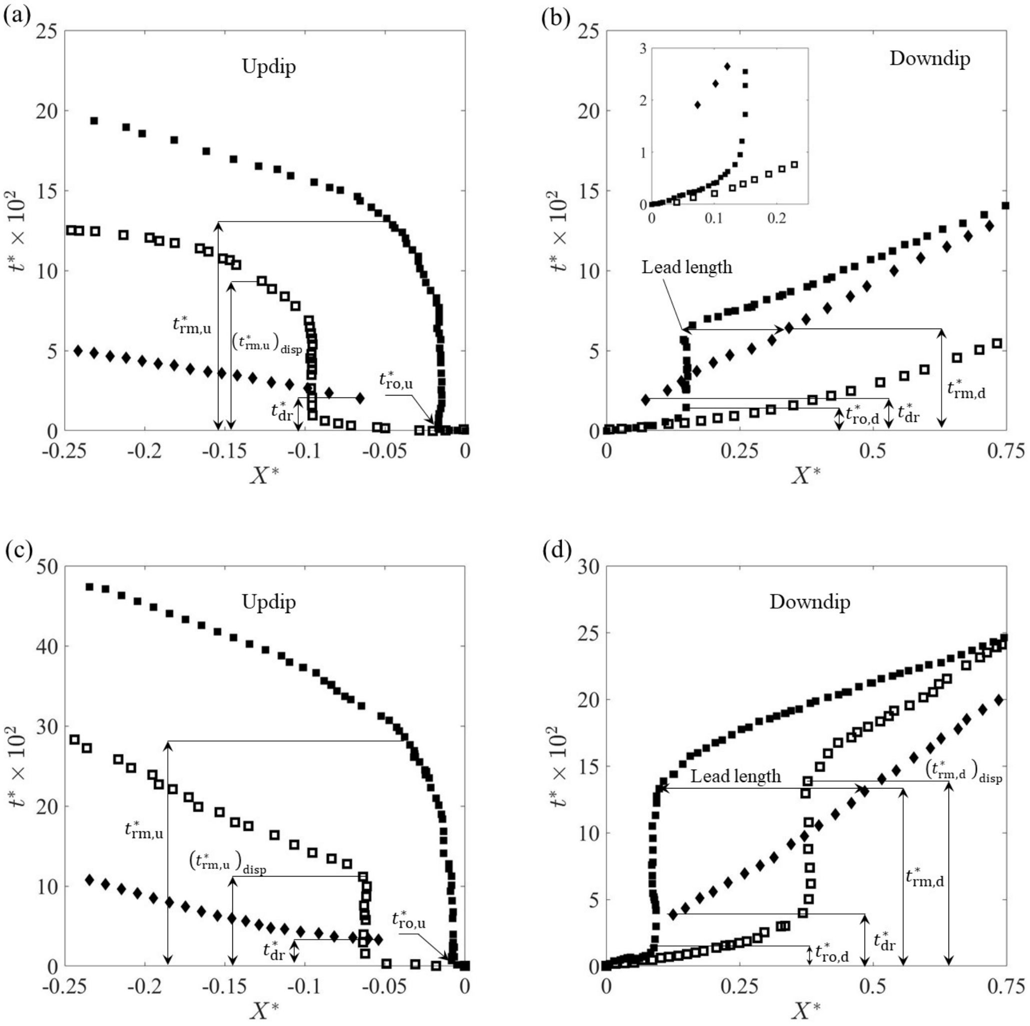

Figure 3.5: Time variation of the nose positions of the primary (squares) and secondary (diamonds) gravity currents for $\theta = 15^\circ$ and $Q_s = 1.01 \pm 0.02\,\mathrm{cm}^3/\mathrm{s}$. Closed and open squares correspond, respectively, to the bulk and dispersed interfaces. (a) Updip, $g'_s = 20.1 \pm 0.9\,\mathrm{cm/s}^2$, (b) downdip, $g'_s = 20.1 \pm 0.9\,\mathrm{cm/s}^2$, (c) updip, $g'_s = 80.1 \pm 0.9\,\mathrm{cm/s}^2$ and (d) downdip, $g'_s = 80.1 \pm 0.9\,\mathrm{cm/s}^2$. The variables $t^*_{\mathrm{ro,u}}$, $t^*_{\mathrm{ro,d}}$, $t^*_{\mathrm{rm,u}}$, $t^*_{\mathrm{rm,d}}$ and t^*_{dr} are defined in text. The inset figure in panel (b) shows a close-up view of the early time dynamics.

downdip side (figures 3.5 c,d). In all cases, $t^* = 0$ indicates the time instant when the plume first strikes the permeability jump.

In addition to differentiating between the primary (squares) and secondary (diamonds) gravity currents, figure 3.5 also distinguishes between the noses associated with interfaces classified as bulk (solid squares) vs. dispersed (open squares). The bulk interface noses of the primary gravity current reach their runout lengths at nondimensional times t^*_{ro}. Consistent with the above remarks, $t^*_{\mathrm{ro,d}} > t^*_{\mathrm{ro,u}}$, where 'u' and 'd' correspond, respectively, to updip and downdip. Along the downdip side, and for $t^* > t^*_{\mathrm{ro,d}}$, the bulk interface nose of the primary gravity current remains fixed until such time as it gets remobilized by the secondary gravity current, a process described in more detail below. In contrast, and as observed for $g'_s = 20.1 \pm 0.9\,\mathrm{cm/s}^2$, the nose corresponding to the downdip dispersed interface continues to propagate with only a moderate deceleration until it reaches the sidewall boundary (figure 3.5 b). Indeed, runout is realized with the dispersed interface only when (i) we examine the counterpart updip flow (figure 3.5 a), or, (ii) we increase the source reduced gravity e.g. from $g'_s = 20.1 \pm 0.9\,\mathrm{cm/s}^2$ (figures 3.5 a,b) to $g'_s = 80.1 \pm 0.9\,\mathrm{cm/s}^2$ (figures 3.5 c,d).

In the lower layer, meanwhile, the draining fluid makes contact with the bottom boundary at $t^* = t^*_{\mathrm{dr}}$, and thereafter, propagates as a pair of oppositely-directed secondary gravity currents. At $t^*_{\mathrm{rm,d}}$ ($> t^*_{\mathrm{dr}}$), the secondary gravity current arising on the downdip side remobilizes the previously arrested primary gravity current. At the point of remobilization, figures 3.5 b and d indicate that the secondary gravity current leads the primary gravity current by a horizontal distance that we shall refer to as the lead length. Corresponding to this lead length, we define a lead angle, Φ, in the manner suggested by figure 3.1 a. (Note that Φ does not, in general, correspond to the angle made by the fluid draining into the lower layer.) On the updip side, and owing to the horizontal position of the nozzle, the secondary gravity current travels a shorter distance in X^*. Consequently, remobilization is delayed and arises only after the secondary gravity current has collided with the sidewall boundary leading to a steady accumulation of draining fluid and the vertical ascent of the first front through the lower layer. Note finally that the methodology for determining precisely the runout and remobilization times is summarized in Appendix B.3.

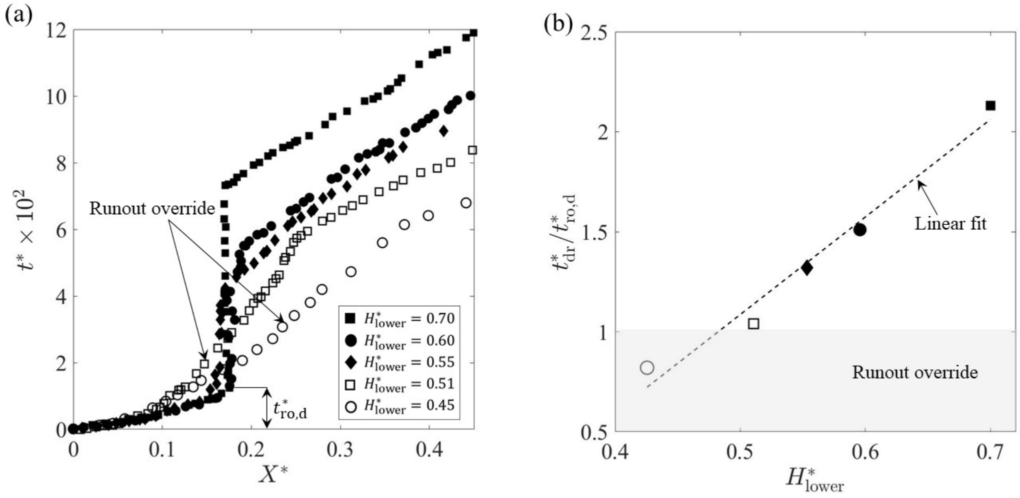

Figure 3.6: (a) Nose positions for the bulk interface of the primary gravity current. Timeseries corresponding to various lower layer depths, H^*_{lower}, are compared. (b) $t^*_{\mathrm{dr}}/t^*_{\mathrm{ro,d}}$ vs. H^*_{lower}. The shaded region indicates the parametric range where we expect runout to be bypassed. The experiments correspond to $\theta = 15^\circ$ and cases E49 – E53 from table B.1.

3.4.2 Primary vs. secondary gravity currents, quantitative comparison

The lower layer depth, H^*_{lower}, as characterized by its value measured directly below the nozzle and further non-dimensionalized by the total height, H, has a significant influence on the early time flow dynamics of the primary gravity current, i.e. for $t^* \leq t^*_{\mathrm{ro,d}}$. Consider, for example, figure 3.6 a, which considers five different values for the lower layer depth spanning the range $0.45 \leq H^*_{\mathrm{lower}} \leq 0.70$. Runout is achieved for sufficiently large H^*_{lower}. Moreover, the time required for remobilization, $t^*_{\mathrm{rm,d}}$, increases with the lower layer depth. When H^*_{lower} is small, however, runout is bypassed, a process we refer to as runout override. Thus when $H^*_{\mathrm{lower}} = 0.51$ or 0.45, the nose of the primary gravity current propagates, albeit unsteadily, without ever becoming arrested. In assessing whether runout will or will not occur, a comparison must be made between $t^*_{\mathrm{ro,d}}$ and t^*_{dr}, only the latter of which depends (approximately linearly) on H^*_{lower}. The comparison in question appears in figure 3.6 b where, for those experiments experiencing runout override, we suppose a value for $t^*_{\mathrm{ro,d}}$ that is

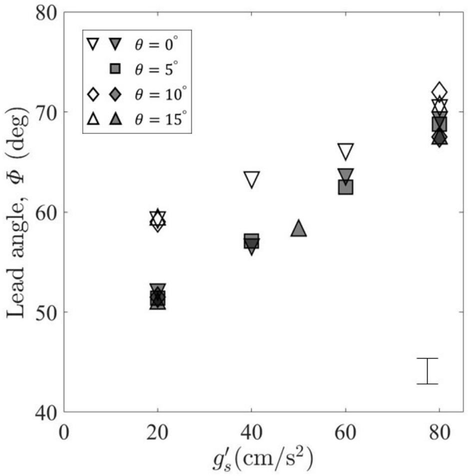

Figure 3.7: Variation of Φ, as defined in figure 3.1 a, with g'_s for different θ. Open and closed symbols correspond to $Q_s = 0.51 \pm 0.02\,\mathrm{cm^3/s}$ and $1.01 \pm 0.02\,\mathrm{cm^3/s}$, respectively. A representative error bar is shown in the lower right-hand corner.

consistent with the companion data sets of figure 3.6 a. When $t^*_{\mathrm{dr}}/t^*_{\mathrm{ro,d}} \lesssim 1$ runout override is expected as indicated by the gray-shaded region in figure 3.6 b.

The lead angle, Φ, is plotted vs. g'_s for various permeability jump angles, θ, in figure 3.7. The trend of the data is roughly linear with larger values of the lead angle occurring for smaller values of Q_s. Figure 3.7 suggests that the lead angle varies most strongly with g'_s followed by Q_s and followed finally by θ, the permeability jump angle exerting only a minor influence. Note also that the importance of the source volume flux is modulated by the source reduced gravity: whereas there is a significant disparity between the small vs. large Q_s data when $g'_s = 20.1 \pm 0.9\,\mathrm{cm/s^2}$, this difference largely disappears for larger g'_s.

For $t^* > t^*_{\mathrm{rm,d}}$, the front speed of the bulk fluid from the downdip primary gravity current is compared against the speed of the secondary gravity current in figure 3.8. The velocities of the primary and secondary gravity currents are both measured with respect to the horizontal and are both non-dimensionalized by the velocity factor β defined in (3.3). When the lead angle is relatively small, e.g. when $Q_s = 1.01 \pm 0.02\,\mathrm{cm^3/s}$ and $g'_s = 20.1 \pm 0.9\,\mathrm{cm/s^2}$, the primary and secondary gravity currents

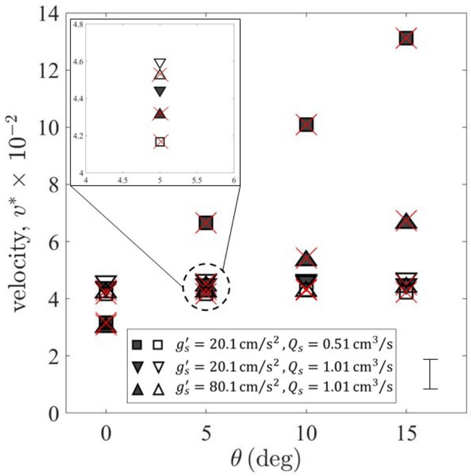

Figure 3.8: [Color] Non-dimensional downdip front velocity, v^*, vs. θ for different source conditions. The closed symbols denote the primary gravity current, and the open symbols denote the secondary gravity current. When the two gravity currents do not coexist, the marker symbols of both the primary and secondary gravity currents include a superimposed red cross. A representative error bar is shown in the bottom right-hand side corner.

coexist and therefore exhibit approximately equal propagation speeds. When the lead angle is large, by contrast, the primary gravity current will, in general, only remobilize when the nose of the secondary gravity current is very close to, or has already collided with, the sidewall boundary. In such instances of non-coexistence, figure 3.8 exhibits a comparatively large range of primary gravity current speeds even as the (normalized) speeds of the secondary gravity currents remain nearly constant. In particular, there are situations (inset, downward-facing triangles) where the speeds of the primary and secondary gravity currents are approximately equal even though the gravity current pair is classified as being of non-coexistence type. Note also that the primary gravity current speed increases roughly linearly with θ, an obvious reflection of the fact that larger permeability jump angles admit a more ready conversion of potential to kinetic energy. Also, and because the total height of our porous medium is fixed, large θ is associated with small $H_{R,\mathrm{lower}}$ – see table 3.1. Correspondingly, fluid from the secondary gravity current has a relatively small vertical distance over which to advect

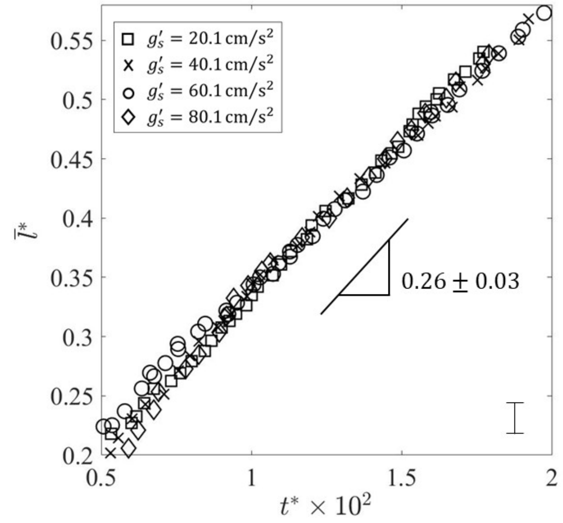

	Slopes	
θ (deg)	$Q_s = 0.51 \pm 0.02\,(\mathrm{cm^3/s})$	$Q_s = 1.01 \pm 0.02\,(\mathrm{cm^3/s})$
0	0.27 ± 0.04	0.26 ± 0.03
5	0.25 ± 0.03	0.24 ± 0.04
15	0.26 ± 0.04	0.27 ± 0.02

Figure 3.9: Evolution of the average draining length, $\bar{l}^*$, with t^* for various g_s' with $\theta = 0°$ and $Q_s = 1.01 \pm 0.02\,\mathrm{cm^3/s}$. The average slope of the data (as measured over the interval $0.5 \leq t^*(\times 10^2) \leq 2$) is reported. The adjoining table indicates the slope values measured for other combinations of θ and Q_s.

before striking the permeability jump. As the fluid in question nears the permeability jump, it has a correspondingly larger influence on the bulk fluid of the primary gravity current for two reasons. Firstly, the streamlines describing draining from the primary gravity current become deflected downdip. Secondly, with relatively less ambient fluid to displace from the lower layer, a greater fraction of the discharged plume fluid flows into the primary gravity current rather than into the lower layer. By both of these effects, we expect (and observe) the speed of the primary gravity current to increase with θ.

3.5 Draining phenomenon and filling box flow

3.5.1 Characterization of the draining flow

To predict the speed of descent of the fluid draining through the lower layer, it is necessary to define an average draining length as

$$\bar{l}(t) = \frac{1}{x_{N_d}(t) - x_{N_u}(t)} \int_{-x_{N_u}(t)}^{x_{N_d}(t)} l(\tilde{x}, t)\,\mathrm{d}\tilde{x} \tag{3.5}$$

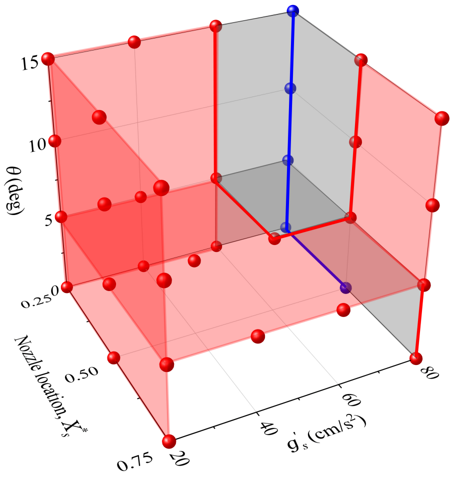

Figure 3.10: [Color] Downdip filling mode as a function of nozzle position, source reduced gravity and permeability jump angle. The red symbols indicate simultaneous filling, while the blue symbols indicate sequential filling. The gray region separating the red and blue symbols signifies a transition region.

where x_{N_u} and x_{N_d} are, respectively, the up- and downdip nose positions of the bulk interface and l is the vertical distance traversed by the draining fluid as measured relative to the permeability jump. The time variation of the non-dimensional average drain length, $\overline{l}^* \equiv \overline{l}/H$, is shown in figure 3.9 for a variety of source conditions. Consistent with figure 3.6 b and the study by Acton *et al.* (2001), $\overline{l}^*$ shows a linear increase with time, except at very early times (not shown in figure 3.9).

3.5.2 Simultaneous vs. sequential filling

In section 3.3.3, we suggested that the filling of the two-layer porous medium could be classified as simultaneous or sequential depending on whether or not the upper and lower layers fill concurrently. Drawing such a distinction is important for the following reason: our analysis has assumed as the dominant dynamical balance buoyancy and viscosity, however, there are other scenarios (Golding *et al.*, 2011; Burnside & Naylor, 2014; Krevor *et al.*, 2015) where capillarity is expected to play a non-subordinate role. In such cases, residual trapping of the injectate is expected to be important. The amount of trapping is found to vary according to whether the intruding flow

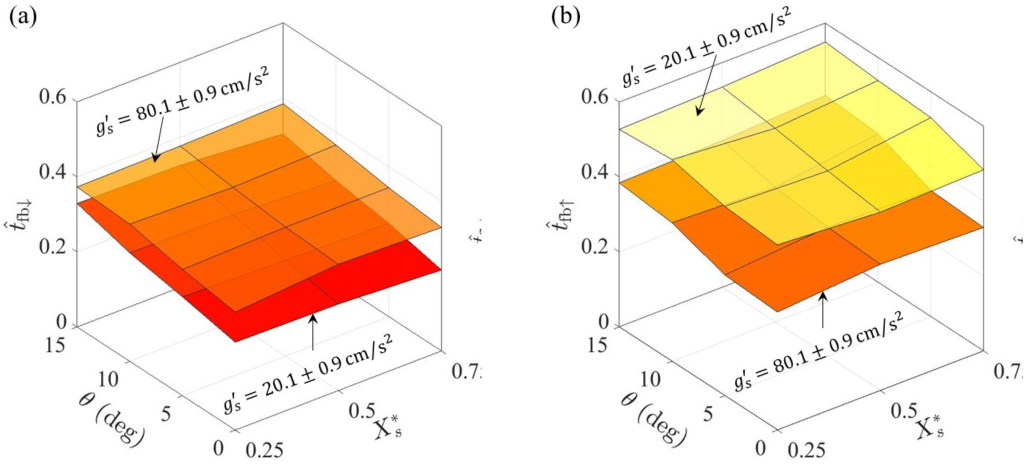

Figure 3.11: [Color] Lower- (a) and upper- (b) bound estimates of the non-dimensional filling box time plotted as a function of the permeability jump angle, θ, and the source position, X_s^*. Two values for the source reduced gravity, g_s', are considered where, in either case, $Q_s = 1.01 \pm 0.02\,\mathrm{cm}^3/\mathrm{s}$. To show the lower surface more clearly, the upper surface is purposely made semi-transparent in both plots.

is primarily horizontal vs. vertical (Adebayo *et al.*, 2017). Because sequential and simultaneous filling are associated with different proportions of horizontal vs. vertical flow, the details of the filling mode will, for this more general case of intermediate Bond number, influence the degree of residual trapping.

A rigorous way of distinguishing sequential vs. simultaneous filling is discussed in Appendix B.4. On this basis, an assessment can be made of the filling mode for each of the experiments performed. A summary of results, pertinent to $Q_s = 1.01 \pm 0.02\,\mathrm{cm}^3/\mathrm{s}$, is presented in figure 3.10 (see also table B.1 of Appendix B.1). The horizontal axes of figure 3.10 indicate the nozzle position and source reduced gravity, whereas the vertical axis indicates the permeability jump angle. The red and blue symbols respectively indicate cases of simultaneous and sequential filling. The gray region indicates a transition region from one filling mode to the other.

When the source reduced gravity is low or moderate, such as for $g_s' = 20.1 \pm 0.9\,\mathrm{cm/s^2}$, the primary gravity current experiences significant dispersion and the nose of the dispersed fluid collides with the sidewall boundary well before the nose of the secondary gravity current – c.f. figure 3.5 b. Thus the upper layer begins to fill well before the secondary layer is filled with contaminated fluid. Generalizing, simultaneous filling is anticipated for small g'_s irrespective of the nozzle position or permeability jump angle. By contrast, the tendency for sequential filling is greater when the source reduced gravity is comparatively large implying (i) shorter runout lengths for the bulk fluid, and, (ii) the possibility of runout for the dispersed fluid – see figure 3.5 d. Note, however, that sequential filing is realized in actual fact only when the nozzle is shifted updip. Regarding the influence of θ, figure 3.10 indicates that the filling mode changes as a result of adjusting θ only in the following instance: $\theta = 0^\circ$ to $\theta = 5^\circ$ for $g'_s = 80\,\mathrm{cm/s^2}$ and the nozzle located at the center of the tank. Figure 3.10 makes clear the fact that simultaneous filling occurs for small g'_s, large θ and downdip-shifted nozzles. By contrast, sequential filling is favored for large g'_s, small θ and a nozzle shifted updip.

The surface plots of figure 3.11 show the normalized filling box time, $\hat{t}_{\mathrm{fb}}$, as a function of θ and X^*_s where both large and small values of g'_s are considered. We define the filling box time as the time taken for the first front propagating through the upper layer to reach a vertical height corresponding to the approximate upper boundary of the porous medium, i.e. $Z^* = 0.99$. Complications arise because the first front is not always horizontal; rather, the upper layer may fill faster in the vicinity of the sidewall boundaries and more slowly in the neighborhood of the plume. This phenomenon is more prevalent for small g'_s and persists even in the limit of large first front elevations – see figures B3 a,c. For these reasons, we define in figure 3.11 the two following filling box times: (i) $\hat{t}_{\mathrm{fb}\downarrow}$ from figure 3.11 a represents a lower-bound estimate to the filling box time that is defined as the time when any portion of the first front (whether to the left or right of the descending plume) first reaches the elevation $Z^* = 0.99$; (ii) $\hat{t}_{\mathrm{fb}\uparrow}$ from figure 3.11 b represents an upper-bound estimate to the filling box time that is defined as the time when the entirety of the first front first has reached $Z^* = 0.99$. The filling box times exhibited in figures 3.11 a,b exhibit minor variations with θ and X_s^*, however, a more interesting variety appears when considering the influence of the source reduced gravity. To wit, $\hat{t}_{\text{fb}\downarrow}(g_s' = 20.1 \pm 0.9\,\text{cm/s}^2) < \hat{t}_{\text{fb}\downarrow}(g_s' = 80.1 \pm 0.9\,\text{cm/s}^2)$ but $\hat{t}_{\text{fb}\uparrow}(g_s' = 20.1 \pm 0.9\,\text{cm/s}^2) > \hat{t}_{\text{fb}\uparrow}(g_s' = 80.1 \pm 0.9\,\text{cm/s}^2)$. When $g_s' = 20.1 \pm 0.9\,\text{cm/s}^2$, the filling mode is always simultaneous and flows, particularly of the primary gravity currents, are characterized by ample dispersion. As a result, and although the upper layer fills relatively quickly with contaminated fluid, it does so non-uniformly. In other words, an abundance of contaminated fluid accumulates along the right sidewall boundary because the potential energy penalty associated with a significantly-deflected first front is small. Thus, it takes relatively little time for the first front to first reach $Z^* = 0.99$ but appreciably more time for the entirety of the first front to reach this elevation. The situation for $g_s' = 80.1 \pm 0.9\,\text{cm/s}^2$ is rather different. Here, less dispersion arises and, according to figure 3.10, the filling mode may be either simultaneous or sequential. In either case, the slope of the first front is smaller than when $g_s' = 20.1 \pm 0.9\,\text{cm/s}^2$. Correspondingly, the gap between $\hat{t}_{\text{fb}\downarrow}$ and $\hat{t}_{\text{fb}\uparrow}$ is smaller by comparison.

3.5.3 Plume deflection

In section 3.2, reference was made to plumes that become deflected as a result of a background mean flow (Weaver & Wilson, 2000; Van Stempvoort *et al.*, 2013) and/or stratigraphic steering (Morgan *et al.*, 2008; Kamath *et al.*, 2012). Motivated by recent observations of turbulent, non-porous media plumes made by Akhter & Kaye (2020), we now explore a further possibility, namely that a plume becomes deflected as a result of a hydrostatic pressure imbalance associated with fluid discharge from the selfsame plume.

When $\theta = 0°$ and the nozzle is centrally located, there exists, not surprisingly, a flow symmetry about $X_s^* = 0.5$ – c.f. figures 5 a - c of Sahu & Flynn (2017). This symmetry can be broken by adjusting θ and/or the location of the plume nozzle. Figures 3.12 a - c show experimental snapshot images where $\theta = 15°$ and the nozzle is

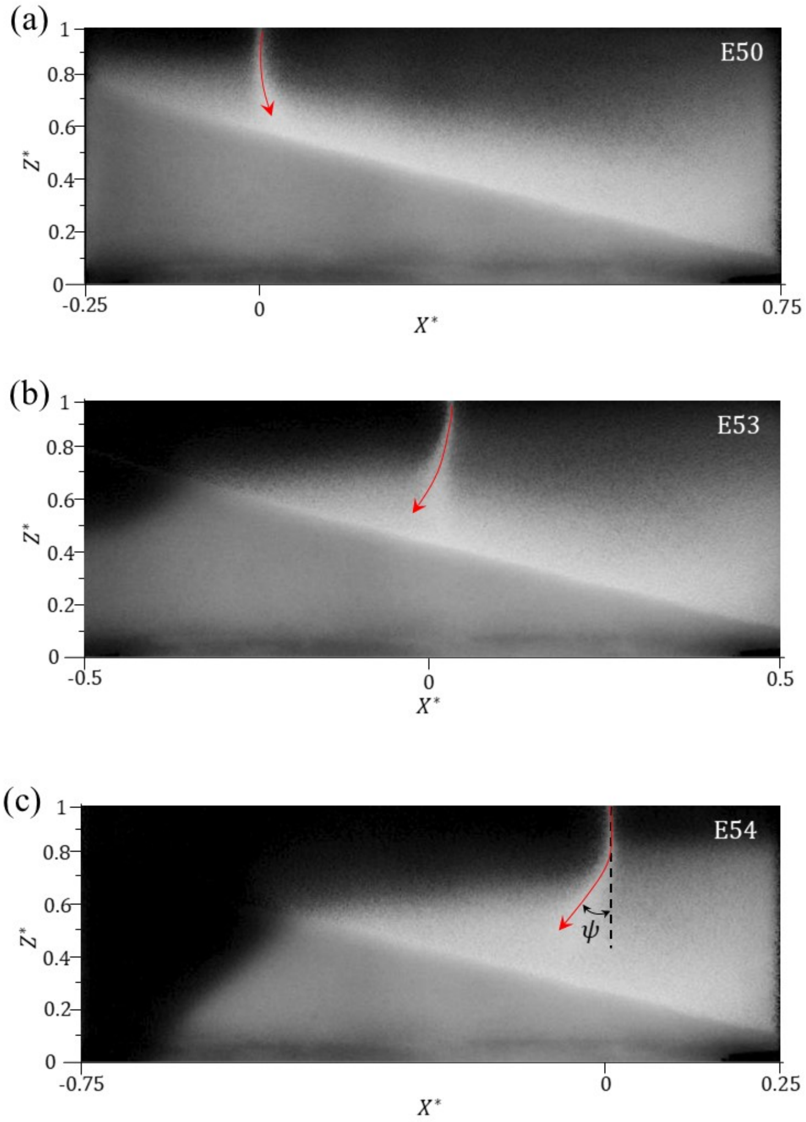

Figure 3.12: [Color] False-color snapshot images showing the deflection of the plume when the source is located (a) updip at $X_s^* = 0.25$, (b) centrally at $X_s^* = 0.5$ and (c) downdip at $X_s^* = 0.75$. The red arrows indicate the magnitude of the plume deflection. The deflection angle, ψ, is defined in (c). Experimental parameters are as follows: $\theta = 15°$, $g_s' = 20.1 \pm 0.9\,\mathrm{cm/s^2}$ and $Q_s = 1.01 \pm 0.02\,\mathrm{cm^3/s}$.

situated at $X_s^* = 0.25, 0.5$ and 0.75, respectively.

In figures 3.12 a - c, the nozzle is, respectively, shifted up- to downdip, but there is an opposite trend when considering the plume deflection. By contrast with the case of a flat permeability jump, figure 3.12 b confirms that an (updip) deflection of the plume is possible even when the nozzle is centrally located. When the plume is not centrally located, figures 3.12 a,c confirm that the deflection direction is away from the closer sidewall boundary. Interestingly, precisely the opposite trend was noted in the recent filling box experiments of Akhter & Kaye (2020), who considered turbulent non-porous media plumes and observed that the deflection direction was towards, not away from, this adjacent sidewall boundary. In summarizing Akhter & Kaye (2020)'s explanation of their observations, reference is made to the short and long sides, which respectively indicate the sides of the experimental tank having the shorter vs. longer horizontal distances from the descending plume to a sidewall boundary. Regarding the discharged plume fluid that accumulated along the bottom of their box, Akhter & Kaye (2020) noted that the depth of this layer was larger on the short side vs. the long side. They surmised that the resulting hydrostatic pressure imbalance led to a net circulation inside their filling box: at depth, dense fluid flowed from the short to the long side resulting in an oppositely-directed return flow of ambient fluid close to the plume source. Because our experiments are characterized by upper and lower layers, they admit a greater variety in terms of return flow pathways. Moreover, any overall circulation that develops within our filling box is expected to be comparatively weaker than in Akhter & Kaye (2020)'s experiments owing to the retarding influence of the porous medium. Correspondingly, and when the plume is shifted off-centre, we observe a deflection only in the direction of the long side. In the process, there arises the interesting scenario illustrated in figure 3.12 c (and also figure 3.12 b) whereby the plume bends towards, rather than away from, the (lower) layer of smaller permeability. This observation runs contrary to the pattern of streamline deflection that is associated with flow focusing whereby the flow is attracted to lenses of higher permeability – see e.g. figure 3.11 A of Phillips (1991).

Seeking to quantify the effects illustrated in figure 3.12, we define a plume deflection angle, ψ, in the manner suggested by figure 3.12 c. When the plume deflects updip (downdip), ψ assumes a negative (positive) value. The time variation of ψ for the

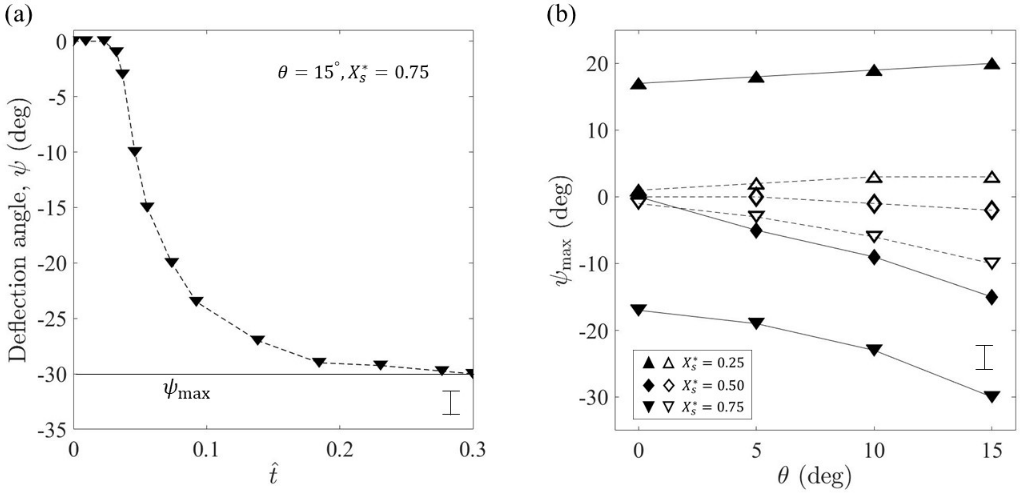

Figure 3.13: (a) Variation of the plume deflection angle, ψ, as a function of time for the experiment illustrated in figure 3.12 c. (b) The magnitude-maximum deflection angle, $\psi_{\max}$, plotted as function of permeability jump angle and nozzle location. Closed and open symbols respectively show $g_s' = 20.1 \pm 0.9\,\mathrm{cm/s^2}$ and $80.1 \pm 0.9\,\mathrm{cm/s^2}$. In (b), symbols are connected by lines only for the sake identifying, more clearly, trends within the data; the lines do not suggest a curve fit. Representative error bars are shown in the lower right-hand corner of each plot.

experiment illustrated in figure 3.12 c, is exhibited in figure 3.13 a. Initially, the plume shows no deflection; at $\hat{t} = 0.04$ the plume starts to deflect updip and there is a corresponding increase in the magnitude of ψ. For $\hat{t} \gtrsim 0.2$, ψ approaches its asymptotic value corresponding, in magnitude, to a maximum deflection angle, $\psi_{\max}$. In figure 3.13 b, $\psi_{\max}$ values are plotted vs. θ. In this same plot, comparisons are made against two different source reduced gravities corresponding to $g_s' = 20.1 \pm 0.9$ (closed symbols) and $80.1 \pm 0.9\,\mathrm{cm/s^2}$ (open symbols). It is observed that the magnitude of $\psi_{\max}$ typically increases with θ. Also, when the nozzle is shifted updip, the plume deflects downdip such that $\psi_{\max} > 0^\circ$. By contrast, $\psi_{\max} < 0^\circ$ when the nozzle is located at the center of the box or is shifted downdip. For fixed source conditions, this latter case is associated with the largest values for $|\psi_{\max}|$. When the source conditions are not fixed, $\psi_{\max}$ depends strongly on the source reduced gravity: for $g_s' = 80.1 \pm 0.9\,\mathrm{cm/s^2}$, the magnitude of plume deflection is significantly less than in the $g_s' = 20.1 \pm 0.9\,\mathrm{cm/s^2}$ case. Plumes containing comparatively dense fluid are more difficult to deflect and tend, therefore, to assume more of a vertical trajectory.

The deflection of the plume is expected to have a relatively minor impact on the overall entrainment of ambient fluid. When the plume deflects, (i) the path length increases, but, (ii) the plume centerline velocity decreases. Because the former and latter effects respectively serve to increase and decrease the rate of entrainment, we anticipate, by analogy with angled turbulent plumes (Lee & Chu, 2003), the net contribution to be even. On the other hand, once the plume becomes deflected, the balance of discharged plume fluid flowing up- vs. downdip must adjust, which may, in turn, impact the subsequent rate of filling of the upper and lower layers. Such considerations are especially relevant in the context of figures 3.12 a,c. In the former figure, the plume deflects downdip suggesting a more rapid filling of the upper layer in the neighborhood of the right sidewall boundary and a smaller value for $\hat{t}_{\mathrm{fb}\downarrow}$. Precisely the opposite trend is expected in figure 3.12 c where the plume deflects updip, which has the effect of (i) directing more dense fluid towards the left sidewall boundary, (ii) reducing the left-to-right difference in the elevation of the first front, and, (iii) increasing $\hat{t}_{\mathrm{fb}\downarrow}$.

3.6 Discussion

To this point, we have discussed three ostensibly distinct aspects of porous media filling box flows namely (i) the runout and subsequent remobilization of the primary gravity currents, (ii) the filling mode, be this simultaneous or sequential, and, (iii) the deflection of the descending plume. In fact, (i), (ii) and (iii) are all tightly interconnected. For example, the stasis characterizing runout is interrupted only when sufficient dense fluid has drained into the lower layer and, for example, the lead angle, $\mathit{\Phi}$, defined by figure 3.7 is exceeded. Thus the initial filling of the lower layer has a direct impact on the process of remobilization and, more generally, the gravity current flows observed along the permeability jump. On the other hand, it is the competition between the primary and secondary gravity currents that dictates whether the first contaminated fluid to reach the downdip sidewall boundary does so along the permeability jump or along the bottom of the box. In this way, the motion of the gravity currents (complicated by the process of dispersion in the upper layer) determines whether or not the upper layer begins to fill before the filling process is complete in the lower layer. Finally, and as highlighted most especially by figure 3.12, plume deflection arises precisely because of left-to-right asymmetries in the manner in which the upper layer fills with contaminated fluid. On the other hand, once the plume is deflected, the proportion of discharged plume fluid directed up- vs. downdip will adjust. In turn, such an adjustment increases the volume of dense fluid supplied to the updip gravity current and impacts the subsequent evolution of the filling process.

As the above explanation makes clear, no single aspect of the filling box dynamics can be categorized comprehensively without considering the impact of the other two. Somewhat after-the-fact, this rationalizes why the present analysis is so much more involved than that summarized in Bharath *et al.* (2020). In that study, the lower layer was effectively considered infinitely deep such that the dynamical phenomena of remobilization, layer filling and plume deflection became moot. On the other hand, even the more involved analysis considered in the present work examines only two layers whereas porous media of the type modeled numerically in the hydrogen storage study of Feldmann *et al.* (2016) contain many more strata, each of different permeability and thickness. Generalizing our results and the interconnections summarized above to this more complicated geometrical description remains a challenge to be conquered in future work.

3.7 Summary and conclusions

We have performed an experimental investigation of buoyancy-driven flows in a two-layered porous medium where the layers are separated by an inclined permeability jump. Throughout, the lower layer had a permeability that was $\frac{1}{9}^{\text{th}}$ the permeability of the upper layer. Experiments were conducted under ambient conditions and entailed the injection of dense salt water into the saturated porous medium leading to the formation of a vertically-descending plume plus gravity currents that propagated along the permeability jump and also along the bottom boundary of the experimental domain. Flows were visualized by the addition of a small amount of dye to the source fluid. In turn, we studied the impact of altering the permeability jump angle, the plume source horizontal location, the source volume flow rate and the source reduced gravity.

In contrast to previous studies (Goda & Sato, 2011; Bharath *et al.*, 2020) that have assumed upper and lower layers of great depth, a novel contribution of the present work is to specifically consider the effect of impermeable boundaries, both lateral and basal. As such, we focus on the processes of upper- and lower-layer filling. In the former case, filling follows from the up- and downdip flow of the primary gravity currents followed by the vertical advection of the first front. In the latter case, filling is related to the advection of the secondary gravity currents that propagate along the base of the lower layer. Added to this advection is the contribution of leakage through the permeability jump, which leads to convection over a broad area. In quantifying the dynamics of layer filling, time series images were constructed to analyse the evolution of flow fronts in both the upper and lower layers – see figure 3.4. An additional benefit of such figures lies in their revelation of primary gravity current dispersion (Sahu & Neufeld, 2020). Correspondingly and when describing the primary gravity current, we differentiate between the bulk vs. the dispersed phases. Except when the lower layer was relatively shallow, the former phase achieved runout, a state of (temporary) stasis wherein the plume inflow was balanced by basal draining. By contrast, runout was only observed for the dispersed phase of the primary gravity current when the plume source density was sufficiently large. Predictions of the runout distance have been made in previous studies; they were characterized by a permeability jump that is flat (Goda & Sato, 2011; Sahu & Flynn, 2017) or sloping (Bharath *et al.*, 2020). A fundamentally new component of our analysis is to characterize the remobilization of the primary gravity currents that arises some time after these primary gravity currents are surpassed by their secondary gravity current counterparts. We characterize, at the time of remobilization, the separation distance between the primary and secondary gravity currents by making reference to a lead angle, Φ – see figure 3.1 a. From figure 3.7, we note that Φ varies approximately linearly with the source reduced gravity but is uninfluenced by the permeability jump angle.

Whatever the particular details of runout and remobilization, comparisons can be drawn between the motion of the primary and secondary gravity currents – see e.g. figures 3.5 and 3.6. On the basis of this comparison, we find that when the primary and secondary gravity currents coexist, they travel at nearly equal velocities that are, in turn, nearly independent of the permeability jump angle – see figure 3.8. The jump angle plays a more important dynamical role for the case of non-coexistence, i.e. it exerts a significant influence on the speed of the remobilized primary gravity current.

In categorizing the nature of the filling in our layered porous medium, we distinguish between modes described as simultaneous vs. sequential. The differences between one and the other filling regime are analyzed by considering an example of each – see e.g. figure B3. From the analysis of figure 3.10, it is observed that simultaneous filling is favored when the source reduced gravity is relatively small and the nozzle is located close to the downdip sidewall boundary. The question of whether sequential vs. simultaneous filling occurs is important when considering the dynamics of the lower layer in particular. In sequential filling, most of the filling of the lower layer is by the horizontal advection of the secondary gravity current. By contrast, and for simultaneous filling, proportionally more of the lower layer filling is by basal draining from the overlying primary gravity current. In the abstract, and for real geological flows, drawing a distinction between simultaneous vs. sequential filling is important: as highlighted in section 3.5.2, either should be associated with a different degree of residual trapping, this for the case (not studied here) where capillary effects make a nontrivial contribution to the flow dynamics.

Whichever the filling mode, the experimental domain must at some point become effectively completely filled with contaminated fluid, defined as fluid having a density larger than that of the ambient fluid that fills the box at the initial instant. The time for this complete filling is defined as the filling box time, $\hat{t}_{\mathrm{fb}}$ i.e. the time required for the first front rising through the upper layer to very nearly reach the level of the plume source. In fact, and for the flows examined here, the inclination of the first front makes defining $\hat{t}_{\mathrm{fb}}$ unambiguously somewhat challenging. Rather, we consider in figure 3.11 lower ($\hat{t}_{\mathrm{fb}\downarrow}$) and upper ($\hat{t}_{\mathrm{fb}\uparrow}$) bound estimates to the filling box time. Whereas $\hat{t}_{\mathrm{fb}\downarrow}$ and $\hat{t}_{\mathrm{fb}\uparrow}$ vary little with the permeability jump angle and the horizontal position of the plume source, we find that dispersion causes the difference $\hat{t}_{\mathrm{fb}\uparrow} - \hat{t}_{\mathrm{fb}\downarrow}$ to be much larger when the source reduced gravity is comparatively small.

In a final component of our analysis, we investigated the trajectory of the descending plume and the manner in which this varies with time due to the filling of the upper layer. The plume may deflect either up- or downdip depending on the source reduced gravity and the nozzle location relative to the sidewall boundary. In turn, the time variation of the plume deflection angle, ψ, and the magnitude-maximum deflection angle, ψ_{max}, are characterized in figure 3.13.

The observations made in this experimental study help to address some of the key uncertainties arising from leakage across a permeability jump. In contrast to numerous previous studies for which the layer defined as our lower layer is either thin (Pritchard *et al.*, 2001; Farcas & Woods, 2009; Woods & Farcas, 2009) or inifnite (Goda & Sato, 2011; Bharath *et al.*, 2020), we consider instead a lower layer of intermediate depth. To this end, we find that the depth of the lower layer is important e.g. in dictating whether or not a state of intermediate runout is achieved – see figure 3.6. The lower layer depth also influences the manner in which the lower layer fills, i.e. whether by the advection of the secondary gravity current or else by the process of basal draining defined above. In studying the intermediate- and late-time dynamics, we find also that the flow propagation is effected by the sidewall boundaries which ultimately impede up- and downdip flow propagation and thereby act as a localized trap (Buschkuehle, 2005). The filling modes identified in this study help to predict the time required to fill these traps and, by extension, the adjoining high vs. low permeability layers.

Chapter 4

Buoyant convection in a multi-layered porous media with permeability jumps

4.1 Introduction

Common to many geological storage/disposal applications, for e.g. during sequestration of sc-CO_2 or acid-gas or else during underground storage of H_2 gas, the respective fluids are injected between two nearly impermeable sedimentary layers. However, due to high buoyancy forces or applying high injection pressure may open up potential leakage pathways and may raise doubts about the integrity of the seal (Rutqvist, 2012; Feldmann *et al.*, 2016; Espinoza & Santamarina, 2017). In the presence of these preferential flow pathways, the so-called impermeable layers, in long duration, do not altogether arrest the seepage/vertical migration, rather they allow the injected fluid to enter the neighbouring storage space or to migrate through multiple-layers before potentially escaping back to the environment. Such phenomena of drainage through multiple sedimentary layers is also observed during groundwater contamination, when a source of dense nonaqueous phase liquid (DNAPL) leaks through bedrock having different permeabilities (Steelman *et al.*, 2020).

In all of the above cases, based on the type of leakage mechanism, the flow patterns within the porous media are expected to vary depending on the porous media set-

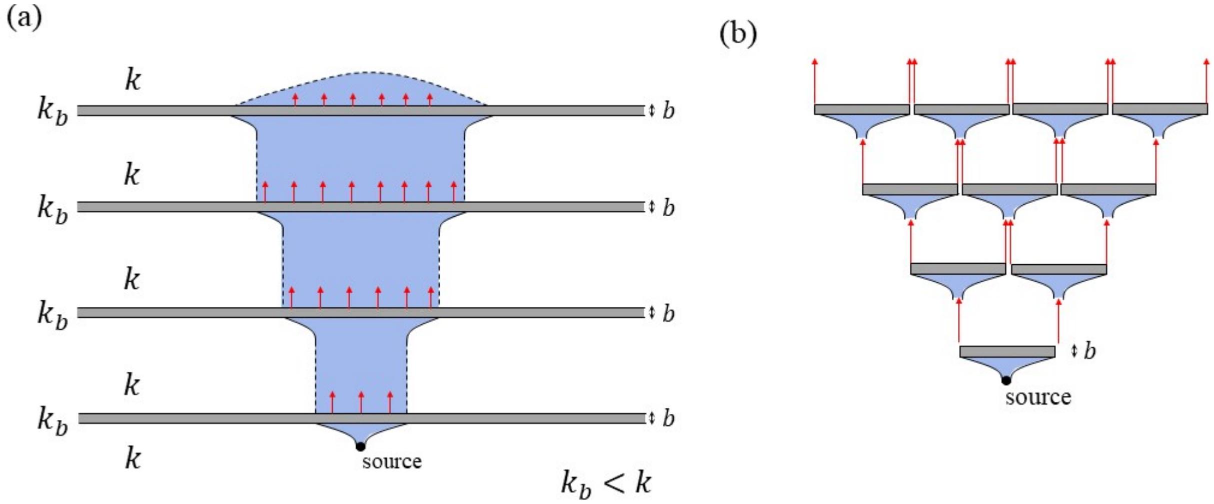

Figure 4.1: Flow patterns (a) in the presence of thin layers of low permeability within a uniform porous media, and (b) across impermeable multiple-flow barriers.

ting. In the theoretical study of Neufeld & Huppert (2009), they derived analytical equations to predict the flow pattern of the“outer envelope” within a multi-layered porous media created by introducing regularly spaced thin layers of low permeability within a uniform porous media, as described in the schematic of figure 4.1 a. They also predicted the maximum lateral extent (or degree of spreading) of the source fluid along each of the thin (horizontal) layers. In another study by Hesse & Woods (2010), the authors modeled the flow across impermeable multiple-flow barriers (positioned horizontally), which obstructed the vertical migration of plume fluid, as depicted in figure 4.1 b. They showed that a steadily rising buoyant fluid can be modeled as a cascade of independent flux partitioning events. Later, Rayward-Smith & Woods (2011) extended this study for the case of tilted impermeable flow barriers.

While investigating flows within a multi-layered porous media, most of the previous studies for the sake of simplicity have considered the flow barriers as impermeable, or, neglected to investigate the flow dynamics within these barriers by assuming them as thin. However, Nordbotten *et al.* (2009) demonstrated the importance of modeling the flow in all the barriers/layers, however small their permeabilities may be, which has a direct impact on the storage characterization of the geological injection sites.

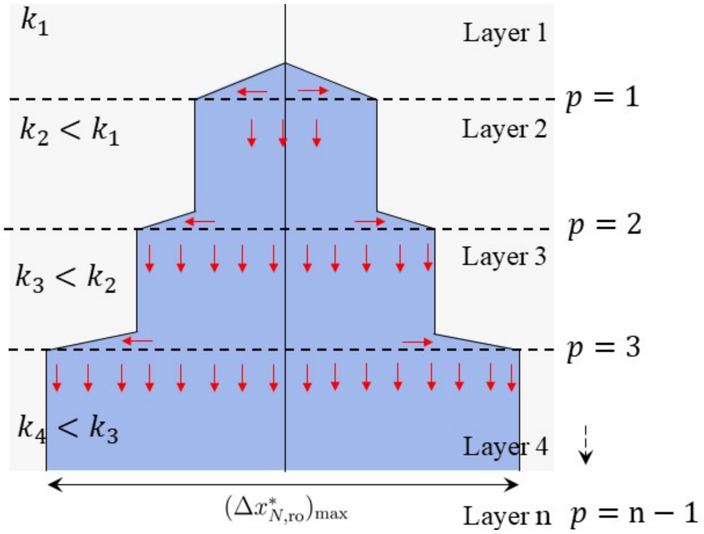

Figure 4.2: [Color] Schematic of discharged plume fluid propagating in a multi-layered porous medium.

In this spirit, considering a simple case of multi-layered porous media configuration, i.e. having two-layers of semi-infinite thicknesses, in Chapter 2 we derived analytical equations that predicts the early-time dynamics of gravity currents propagating, up- and downdip, along an inclined permeability jump. At later times, the gravity currents, along both up- and downdip, reach their respective runout distances at steady-state. However, fluid draining from underneath the respective gravity currents continue to propagate vertically downwards, until it gets impeded by an impermeable bottom boundary or another permeability jump. The flow dynamics related to the former scenario is investigated in details in Chapter 3, wherein, all of the draining fluid upon striking an impermeable boundary propagate along slope, in both left and right directions, as secondary gravity currents. At later instant in time, these secondary gravity currents tug along with it the previously arrested (primary) gravity currents in the upper layer. In contrast, allowing the draining fluid to strike another permeability jump, may change the dynamics of the secondary gravity currents. Analysing the flow dynamics of a dense fluid falling through a porous media having multiple permeability jumps is precisely the objective of this chapter.

In this study, we seek to predict the outer envelope formed inside a multi-layered porous medium formed by layers of different permeabilities. For this, we analyse the source fluid as it drains across multiple layers (not so thin), as shown in figure 4.2. Each of the adjacent layers share a common permeability jump boundary. The rest of the chapter is outlined as follows: in section 4.2, we establish steady-state equations for the flow in question. In section 4.3, we select an appropriate numerical scheme and describe the method of implementation of the problem in question. In section 4.4, we discuss the simulation results along with the comparison to theoretical predictions. Finally, in section 4.5 we summarize and discuss the key findings of this study.

4.2 Theoretical modeling

We consider the injection of a heavy source fluid of density, ρ_s, into a multi-layered porous medium which is previously saturated with ambient fluid of density, $\rho_o < \rho_s$, and adhere to Boussinesq approximation, as shown schematically in figure 4.2. For a porous media configuration having n-layers, each of the layers are separated from its adjacent layer by a single and sharp permeability jump, denoted as $p = 1, 2, 3......(\mathrm{n}-1)$, which may be horizontal or inclined at an angle θ to the horizontal. The injection of the source fluid is always made into the topmost layer (layer 1) and directly above the first permeability jump boundary $p = 1$.

4.2.1 Steady-state equations for gravity currents

The equations of gravity currents propagating along a flat or inclined permeable boundary, both up- and downdip, fed by a vertically descending plume were derived in Chapter 2. Thus recalling (2.12)

$$\frac{\partial h}{\partial t} = \begin{cases} \beta(1-\chi h_{0^-}\cos\theta)^{-\frac{1}{4}}\Big[\dfrac{\partial}{\partial x}\Big(h\dfrac{\partial h}{\partial x}\cos\theta + h\sin\theta\Big) - KG'\Big(1+\dfrac{h}{l}\cos\theta\Big)\Big], \\ \hfill [\text{Updip, } -x_{N_u} < x < 0] \\ \beta(1-\chi h_{0^+}\cos\theta)^{-\frac{1}{4}}\Big[\dfrac{\partial}{\partial x}\Big(h\dfrac{\partial h}{\partial x}\cos\theta - h\sin\theta\Big) - KG'\Big(1+\dfrac{h}{l}\cos\theta\Big)\Big], \\ \hfill [\text{Downdip, } 0 < x < x_{N_d}] \end{cases} \tag{4.1}$$

The notations in the above equation carry their usual meaning as described in Chapter 2. The first two terms on the right-hand side are the advection terms, whereas the third term corresponds to basal draining. Equation (4.1) has a steady-state solution when the up- and downdip gravity currents reach their respective runout lengths. It is expected that at runout, the length of the draining fluid continues to grow with time and therefore at later times the gravity up- and downdip become very small in comparison, i.e. $h \ll l$. Furthermore, G' is the ratio of the lower to upper layer reduced gravities, i.e. $G' = \bar{g}'_d/\bar{g}'_c$. It defines the degree of entrainment experienced by the draining fluid as it falls through the layer below the permeability jump. At later times, the volume of the draining fluid becomes sufficiently large compared to the area of the interface exposed to lower layer ambient fluid; as such, we consider G' as unity in the above equation. And K is the ratio of permeabilities of the lower to upper layer and is a measure of cross flow resistance at the permeability jump. At steady-state, (4.1) reduces to

$$0 = \begin{cases} \dfrac{\partial}{\partial x}\Big(h\dfrac{\partial h}{\partial x}\cos\theta + h\sin\theta\Big) - K, & [\text{Updip}, \ -x_{N_u,\text{ro}} < x < 0] \\ \\ \dfrac{\partial}{\partial x}\Big(h\dfrac{\partial h}{\partial x}\cos\theta - h\sin\theta\Big) - K, & [\text{Downdip}, \ 0 < x < x_{N_d,\text{ro}}] \end{cases} \tag{4.2}$$

here, $x_{N_u,\text{ro}}$ and $x_{N_d,\text{ro}}$ are the nose positions evaluated at runout on the up- and downdip sides, respectively. Since, the volume source is located above the permeability jump boundary, the value of reduced gravity in the velocity term is equal to that at the source itself, i.e. $\beta = (k_1 g'_s)/(\phi\nu)$. Furthermore, since β is a non-zero quantity, we equate rest of the terms within the bracket to zero. The general form of the steady-state gravity current equations along different permeability jump boundaries, i.e. $p = 1, 2, 3, 4, 5$.........(n $-$ 1) can be written as

$$0 = \begin{cases} \dfrac{\partial}{\partial x}\Big(h\dfrac{\partial h}{\partial x}\cos\theta + h\sin\theta\Big) - K\Big]_p, & \text{Updip}\begin{cases} -(x_{N_u,\text{ro}})_p < x < 0 & [p = 1] \\ -(x_{N_u,\text{ro}})_p < x < -(x_{N_u,\text{ro}})_{p-1} & [p > 1] \end{cases} \\ \dfrac{\partial}{\partial x}\Big(h\dfrac{\partial h}{\partial x}\cos\theta - h\sin\theta\Big) - K\Big]_p, & \text{Downdip}\begin{cases} 0 < x < (x_{N_d,\text{ro}})_p & [p = 1] \\ (x_{N_d,\text{ro}})_{p-1} < x < (x_{N_d,\text{ro}})_p & [p > 1] \end{cases} \end{cases} \tag{4.3}$$

4.2.2 Initial and boundary conditions

4.2.2.1 Source volume influx ($p = 1$)

We consider the position of the source in the first layer and at the permeability jump interface, i.e. at $p = 1$. The constant influx condition to the gravity currents reads

$$\begin{aligned} \beta\Big(h\frac{\partial h}{\partial x}\cos\theta + h\sin\theta\Big)\Big|_{0^-}\Big]_{p=1} &= -(1-f_{a,1})q_s, \quad [\text{Updip}, -(x_{N_u,\text{ro}})_{p=1} < x < 0] \\ \beta\Big(h\frac{\partial h}{\partial x}\cos\theta - h\sin\theta\Big)\Big|_{0^+}\Big]_{p=1} &= -f_{a,1}q_s, \quad [\text{Downdip}, 0 < x < (x_{N_d,\text{ro}})_{p=1}] \end{aligned} \tag{4.4}$$

here q_s is the source volume flux per unit width, the velocity factor $\beta = (k_1 g'_s)/(\phi\nu)$ and f_a is the volume fraction downdip measured at steady-state. The source reduced gravity $g'_s = g(\Delta\rho_s/\rho_o)$.

4.2.2.2 Resolving volume flux in the bottom layers ($p > 1$)

First, let us resolve the along slope volume flux, $q_{s,p=2}$, at the second permeability jump, i.e. at $p = 2$. For this, first we need to evaluate the draining flow rate across the permeability jump $p = 1$ given by

$$q_{\text{drain},p=1} = \Big(\int_{-x_{N_u,\text{ro}}}^{x_{N_d,\text{ro}}} w_{\text{drain}}\,\mathrm{d}x'\Big)_{p=1} \tag{4.5}$$

where, w_{drain} is the draining velocity across the permeability jump $p = 1$. In seeking an expression for w_{drain}, we recall draining velocity from (2.9) derived in Chapter 2 and assuming $h \ll l$, we consider

$$w_{\text{drain},p=1} = -\frac{k_2\Delta\rho_s g}{\mu} \tag{4.6}$$

Substituting (4.6) in (4.5), we get

$$q_{\text{drain},p=1} = -\frac{k_2\Delta\rho_s g}{\mu}(x_{N_d,\text{ro}} + x_{N_u,\text{ro}})_{p=1} \tag{4.7}$$

Now performing mass balance at $p = 2$, we get the expression of total volume flux along slope as

$$q_{s,p=2} = \frac{k_2\Delta\rho_s g}{\mu}(1-K_2)(x_{N_d,\text{ro}} + x_{N_u,\text{ro}})_{p=1} \tag{4.8}$$

here $K_2 = k_3/k_2$ is the ratio of permeability jump. Form (4.8) it becomes evident that for an along slope flow to exist, K_2 must be less than unity. Now, the constant influx condition to the gravity currents at $p = 2$ reads

$$\begin{aligned} \left(h\frac{\partial h}{\partial x}\cos\theta + h\sin\theta\right)\Big|_{0^-}\Big]_{p=2} &= -(1-f_{a,2})(1-K_2)(x_{N_d,\mathrm{ro}} + x_{N_u,\mathrm{ro}})_{p=1}, \\ &\qquad [\text{Updip, } -(x_{N_u,\mathrm{ro}})_{p=2} < x < -(x_{N_u,\mathrm{ro}})_{p=1}] \\ \left(h\frac{\partial h}{\partial x}\cos\theta - h\sin\theta\right)\Big|_{0^+}\Big]_{p=2} &= -f_{a,2}(1-K_2)(x_{N_d,\mathrm{ro}} + x_{N_u,\mathrm{ro}})_{p=1}, \\ &\qquad [\text{Downdip, } (x_{N_d,\mathrm{ro}})_{p=1} < x < (x_{N_d,\mathrm{ro}})_{p=2}] \end{aligned} \tag{4.9}$$

The general form of volume influx conditions in different layers and corresponding to $p > 1$, can be written as

$$\begin{aligned} \left(h\frac{\partial h}{\partial x}\cos\theta + h\sin\theta\right)\Big|_{0^-}\Big]_{p} &= -(1-f_{a,p})(1-K_p)(x_{N_d,\mathrm{ro}} + x_{N_u,\mathrm{ro}})_{p-1}, \\ &\qquad [\text{Updip, } -(x_{N_u,\mathrm{ro}})_{p} < x < -(x_{N_u,\mathrm{ro}})_{p-1}] \\ \left(h\frac{\partial h}{\partial x}\cos\theta - h\sin\theta\right)\Big|_{0^+}\Big]_{p} &= -f_{a,p}(1-K_p)(x_{N_d,\mathrm{ro}} + x_{N_u,\mathrm{ro}})_{p-1}, \\ &\qquad [\text{Downdip, } (x_{N_d,\mathrm{ro}})_{p-1} < x < (x_{N_d,\mathrm{ro}})_{p}] \end{aligned} \tag{4.10}$$

A final boundary condition is applied at the noses of the up- and downdip gravity currents at all values of p, such that

$$h_{-(x_{N_u,\mathrm{ro}})_{\mathrm{p=n}}} = 0 \qquad \text{and} \qquad h_{(x_{N_d,\mathrm{ro}})_{\mathrm{p=n}}} = 0 \tag{4.11}$$

4.2.3 Dimensionless governing equations

We define characteristic spatial and temporal variables, Π_x and Π_t, as follows:

$$\Pi_{x,s} = \frac{q_s}{\phi\beta} \qquad \text{and} \qquad \Pi_{t,s} = \frac{q_s}{\phi\beta^2} \tag{4.12}$$

Using the above characteristic variables, we non-dimensionalize other variables using

$$x^* = \frac{x}{\Pi_{x,s}}, \qquad h^* = \frac{h}{\Pi_{x,s}}, \qquad t^* = \frac{t}{\Pi_{t,s}} \tag{4.13}$$

Thus (4.3) may be respectively rewritten as

$$0 = \begin{cases} \dfrac{\partial}{\partial x^*}\Big(h^*\dfrac{\partial h^*}{\partial x^*}\cos\theta + h^*\sin\theta\Big) - K\Big]_p, & \text{Updip} \begin{cases} -(x^*_{N_u,\mathrm{ro}})_p < x^* < 0 & [p=1] \\ -(x^*_{N_u,\mathrm{ro}})_p < x^* < -(x^*_{N_u,\mathrm{ro}})_{p-1} & [p>1] \end{cases} \\ \\ \dfrac{\partial}{\partial x^*}\Big(h^*\dfrac{\partial h^*}{\partial x^*}\cos\theta - h^*\sin\theta\Big) - K\Big]_p, & \text{Downdip} \begin{cases} 0 < x^* < (x^*_{N_d,\mathrm{ro}})_p & [p=1] \\ (x^*_{N_d,\mathrm{ro}})_{p-1} < x^* < (x^*_{N_d,\mathrm{ro}})_p & [p>1] \end{cases} \end{cases} \tag{4.14}$$

Meanwhile, the boundary conditions (4.4) and (4.10) can, respectively, be written as

$$\begin{gathered} \Big(h^*\frac{\partial h^*}{\partial x^*}\cos\theta + h^*\sin\theta\Big)\Big|_{0^-}\Big]_{p=1} = -(1-f_{a,p=1}), \quad [\text{Updip}, -(x^*_{N_u,\mathrm{ro}})_{p=1} < x^* < 0] \\ \\ \Big(h^*\frac{\partial h^*}{\partial x^*}\cos\theta - h^*\sin\theta\Big)\Big|_{0^+}\Big]_{p=1} = -f_{a,p=1}, \quad [\text{Downdip}, 0 < x^* < (x^*_{N_d,\mathrm{ro}})_{p=1}] \end{gathered} \tag{4.15}$$

and for $p > 1$

$$\begin{aligned} \Big(h^*\frac{\partial h^*}{\partial x^*}\cos\theta + h^*\sin\theta\Big)\Big|_{0^-}\Big]_p &= -(1-f_{a,p})(1-K_p)(x^*_{N_d,\mathrm{ro}} + x^*_{N_u,\mathrm{ro}})_{p-1}, \\ &\qquad [\text{Updip}, -(x^*_{N_u,\mathrm{ro}})_p < x^* < -(x^*_{N_u,\mathrm{ro}})_{p-1}] \\ \Big(h^*\frac{\partial h^*}{\partial x^*}\cos\theta - h^*\sin\theta\Big)\Big|_{0^+}\Big]_p &= -f_{a,p}(1-K_p)(x^*_{N_d,\mathrm{ro}} + x^*_{N_u,\mathrm{ro}})_{p-1}, \\ &\qquad [\text{Downdip}, (x^*_{N_d,\mathrm{ro}})_{p-2} < x^* < (x^*_{N_d,\mathrm{ro}})_p] \end{aligned} \tag{4.16}$$

The nose conditions in (4.11) read as

$$h^*_{-(x^*_{N_u,\mathrm{ro}})_{p=\mathrm{n}}} = 0 \qquad \text{and} \qquad h^*_{(x^*_{N_d,\mathrm{ro}})_{p=\mathrm{n}}} = 0 \tag{4.17}$$

We develop a numerical approach to solve the equations (4.14-4.11), similar to that described in Appendix A.2. Model output predicts the steady-state flow pattern, e.g. by describing the shape of the "outer envelope" (as described in Neufeld & Huppert (2009)). As illustrated in figure 4.3, this outer envelope is defined as the boundary corresponding to the interface separating the source and the ambient fluids (marked in red on the plots). We further compare the model predictions with numerical simulations as described below.

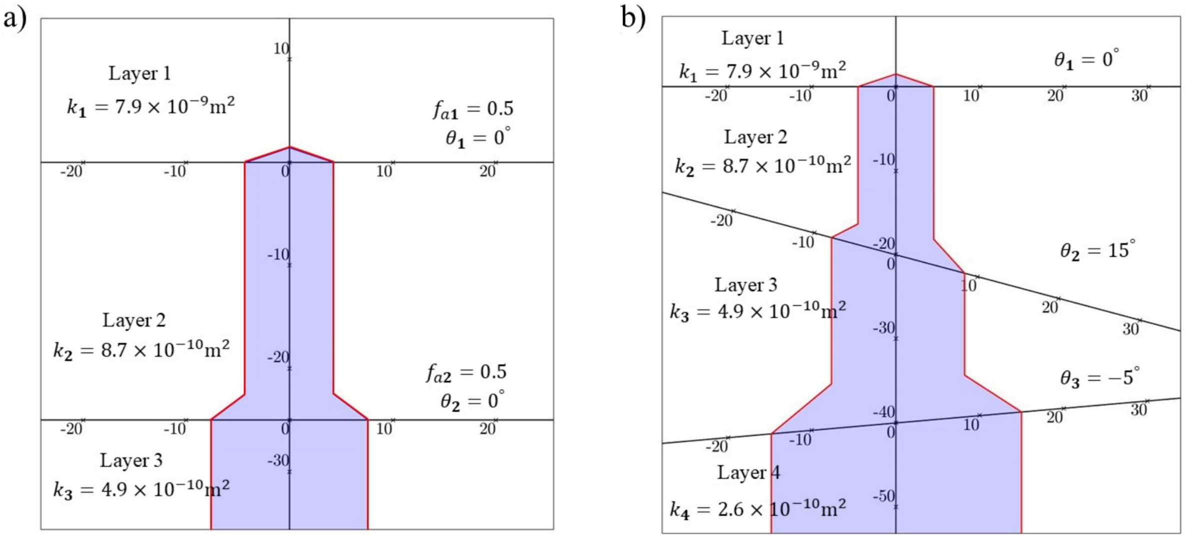

Figure 4.3: Analytical model predictions for porous media configuration having (a) three-layers with horizontal permeability jumps, and (b) four-layers with inclined permeability jumps.

4.3 Numerical modeling

4.3.1 Overview and selection of numerical scheme

In the past, many authors have explored various procedures to numerically discretize and simulate multiphase flows in porous media with Darcy velocity, such as finite-difference (FD), finite-element (FE) and finite-volume (FV) schemes. The key difference between FE methods and FD methods lies in the calculation of the fluid pressure gradient. The FD method computes the gradient using a finite-difference approximation. This requires that the interface between two nodes is perpendicular to the line connecting the nodes. FE methods, in general, do not suffer from this restriction because the gradient is calculated based on element interpolation functions. On the other hand, the FV approach enforces the conservation of quantities discrete levels, i.e. mass, momentum and energy remain conserved at local scales. However, conserving these quantities are a major challenge because the constitutive relations for multiphase flows are non-linear. FE methods commonly allow for a more flexible representation of geological structures as suggested by other authors (Lewis & Roberts, 1984; Morgan *et al.*, 1984), and therefore, we adopt this scheme to investigate flows in multi-layered geometry. In general, FE methods make use of the "weak form" to solve the partial differential equations. The methods to transform the differential equations to an integral form are generic and usually provide accurate predictions, and also they can be applied to complex geometries (Liu & Quek, 2003).

4.3.2 Model implementation in COMSOL multiphysics

In this study, we make use of the FE based multiphysics COMSOL (ver. 5.5) simulator to numerically simulate the motion of a dense source fluid inside a two-dimensional, multi-layered porous media. The porous layers are constructed using spherical beads and the permeability is calculated using the empirical relationship proposed by Kozeny and Carman, and discussed in Dullien (1979), i.e.

$$k = \frac{d^2\phi^3}{180(1-\phi)^2}$$

where d is the bead diameter and a constant porosity of $\phi = 0.38$ is assumed. The complexity of the porous medium is increased by progressively adding five layers of distinct permeabilities as described in the table 4.1 a-d. The layers from 1 to 5 appear in a decreasing order of their permeabilities. Furthermore, three different cases are selected such that ratio of permeabilities in the bottommost (Layer 5) and topmost (Layer 1) layers are varied. For Case 1, this ratio is 0.079; for Case 2, it is 0.063 and for Case 3, it is 0.049. As part of our study, we compare the five-layers case with cases having four-layers (Layer 4 eliminated), three-layers (Layers 4 and 3 eliminated) then two-layers (Layers 4, 3 and 2 eliminated). To explain the method of implementation in COMSOL, we demonstrate below the step-by-step process of setting up the problem, this for the simpler scenario of two-layers related to Case 1 of table 4.1a.

4.3.2.1 Physics selection

As a first step in establishing the problem, we need to select the appropriate set of equations in COMSOL that describes the flow in question. Since we are interested

Table 4.1: Configurations of the porous media.

Layer		**Case 1**		**Case 2**		**Case 3**	
No.	Depth (cm)	d (mm)	k (m^2)	d (mm)	k (m^2)	d (mm)	k (m^2)
1	4	3.0	7.14×10^{-9}	3.0	7.14×10^{-9}	3.0	7.14×10^{-9}
5	16	0.84	5.63×10^{-10}	0.75	4.46×10^{-10}	0.66	3.48×10^{-10}

(a) Two-layers

Layer		**Case 1**		**Case 2**		**Case 3**	
No.	Depth (cm)	d (mm)	k (m^2)	d (mm)	k (m^2)	d (mm)	k (m^2)
1	4	3.0	7.14×10^{-9}	3.0	7.14×10^{-9}	3.0	7.14×10^{-9}
2	4	2.18	3.78×10^{-9}	2.12	3.57×10^{-9}	2.06	3.35×10^{-9}
5	12	0.84	5.63×10^{-10}	0.75	4.46×10^{-10}	0.66	3.48×10^{-10}

(b) Three-layers

Layer		**Case 1**		**Case 2**		**Case 3**	
No.	Depth (cm)	d (mm)	k (m^2)	d (mm)	k (m^2)	d (mm)	k (m^2)
1	4	3.0	7.14×10^{-9}	3.0	7.14×10^{-9}	3.0	7.14×10^{-9}
2	4	2.18	3.78×10^{-9}	2.12	3.57×10^{-9}	2.06	3.35×10^{-9}
3	4	1.59	2.0×10^{-9}	1.5	1.78×10^{-9}	1.41	1.58×10^{-9}
5	8	0.84	5.63×10^{-10}	0.75	4.46×10^{-10}	0.66	3.48×10^{-10}

(c) Four-layers

Layer		**Case 1**		**Case 2**		**Case 3**	
No.	Depth (cm)	d (mm)	k (m^2)	d (mm)	k (m^2)	d (mm)	k (m^2)
1	4	3.0	7.14×10^{-9}	3.0	7.14×10^{-9}	3.0	7.14×10^{-9}
2	4	2.18	3.78×10^{-9}	2.12	3.57×10^{-9}	2.06	3.35×10^{-9}
3	4	1.59	2.0×10^{-9}	1.5	1.78×10^{-9}	1.41	1.58×10^{-9}
4	4	1.16	1.06×10^{-9}	1.06	8.92×10^{-10}	0.97	7.41×10^{-10}
5	4	0.84	5.63×10^{-10}	0.75	4.46×10^{-10}	0.66	3.48×10^{-10}

(d) Five-layers

in the low velocity flows, i.e. Re $\lesssim O(10)$, we first interface the Darcy's law by selecting: `Fluid flow` → `Porous media in subsurface flow` → `Darcy's law`. The equations for Darcy's velocity and continuity equation used are

$$\text{Darcy's velocity: } \mathbf{u} = \frac{k}{\mu}(\nabla p + \rho \mathbf{g}) \tag{4.18a}$$

$$\text{Continuity equation: } \frac{\partial}{\partial t}(\phi \rho) + \nabla.(\rho \mathbf{u}) = 0 \tag{4.18b}$$

where $\mathbf{u}$ is the Darcy velocity vector, k is the permeability of the porous medium, μ is the average dynamic viscosity of the fluids, ϕ is the porosity, p is the fluid's pressure, and ρ is the average fluid density. The permeabilities of Layer 1 and Layer 5 are set to $k_1 = 7.14 \times 10^{-9}\,\mathrm{cm}^2$ and $k_5 = 5.63 \times 10^{-10}\,\mathrm{cm}^2$, respectively, corresponding to Case 1 of table 4.1a. We set the porosity of the material as 0.38 in both layers. The properties of the ambient fluid, such as density and dynamic viscosity, are selected assuming fresh water at 20° C, i.e. $\mu = 1.002\,\mathrm{mPa.s}$ and $\rho_o = 998\,\mathrm{kg/m}^3$.

Then, in order to compute the species concentration and its transport we select: `Chemical species transport` → `Transport of diluted species in porous media`. The equation of molar concentration, c_i, that describes transport of solute concentration in a fully-saturated porous medium is given by the expression

$$\frac{\partial}{\partial t}(\phi c_i) + \mathbf{u}.\nabla c_i = \nabla.[(D_{\mathrm{D},i} + D_{\mathrm{e},i})\nabla c_i] + R_i + S_i \tag{4.19}$$

On the left-hand side, the first term corresponds to the accumulation of the species, while the second term corresponds to the convective transport due to a velocity $\mathbf{u}$. On the right-hand side, the first term introduces the spreading of species due to mechanical mixing (dispersion), as well as from the diffusion. The dispersion tensor is denote by D_D and the effective diffusion by D_e. For a fully-saturated porous media, $D_\mathrm{e} = (\phi/\tau)D$, where, D is the molecular diffusion coefficient and τ is the tortuosity and we set these to a constant values of $2.5 \times 10^{-5}\,\mathrm{cm}^2/\mathrm{s}$ and 2, respectively. However, in our study we neglect the contribution of dispersion and therefore set D_D to zero.

The last two terms on the right, R_i and S_i, describe the reaction rate and arbitrary source terms, respectively, are also set to zeros.

4.3.2.2 Model geometry

Next, the geometry of the two-dimensional porous medium is implemented, as shown in figure 4.4. The outer dimensions of the porous medium of height $H = 20\,\mathrm{cm}$ and length $L = 40\,\mathrm{cm}$ is selected and is maintained constant for all the other cases to be investigated in this study. The permeability jump boundary separating layers 1 and 5, located at a height of 16 cm from the base, is defined using a standard sigmoid function of the form $S(x) = 1/(1 + e^{-Ax})$, where the magnitude of the constant A denotes the sharpness of the permeability jump. In our study, we select $A = 3500$. The location of the source is modeled as a circular geometry of diameter 0.255 cm and is positioned at the horizontal center and 1 cm above the permeability jump, as indicated in figure 4.4.

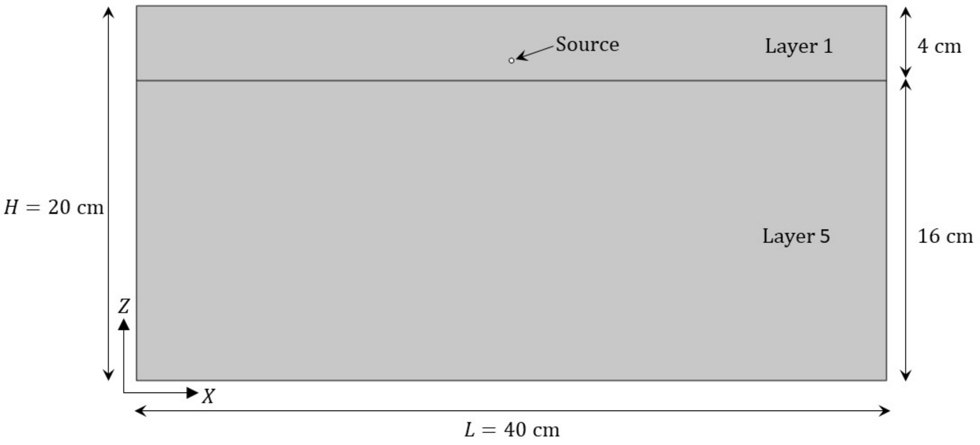

Figure 4.4: Geometric model.

4.3.2.3 Initial and boundary conditions

At $t = 0$, we assume that a quiescent state such that the pressure distribution is hydrostatic. Also, the solute concentration is set to $C_o = 0\,\mathrm{mol/m^3}$ corresponding to a source density of $\rho_o = 998\,\mathrm{kg/m^3}$. An inlet velocity of 1.6×10^{-3} m/s is specified only at the bottom half of the circular source. Also, the NaCl concentration at the source is set to $C_s = 350\,\mathrm{mol/m^3}$ corresponding to a source density of $\rho_s = 1018\,\mathrm{kg/m^3}$. The density is related to concentration field, C, by making use of the relation,

$$\rho = \rho_o + [(\rho_s - \rho_o)/(C_s - C_o)]\,C$$

The outer boundary of the box is set to no-flow conditions except at the bottom boundary, where the ambient fluid when being displaced by the source/contaminated fluid, as well as the source fluid itself at later times are allowed to exit perpendicular to the surface, as indicated in figure 4.5.

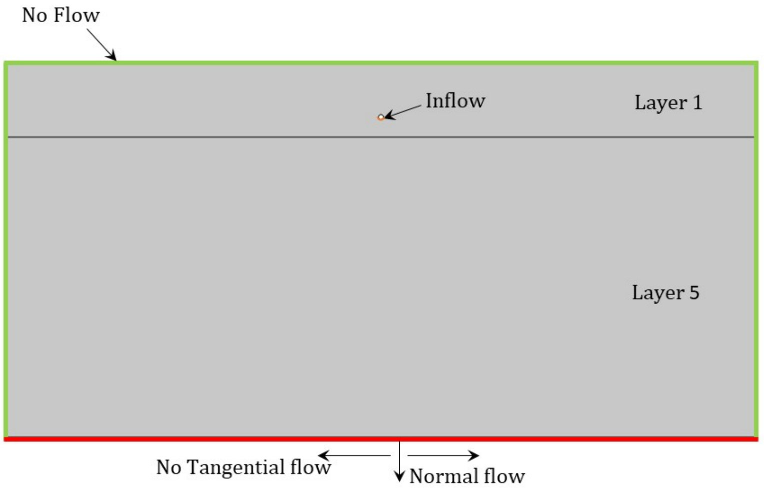

Figure 4.5: Boundary conditions on the geometry.

4.3.2.4 Meshing

At the final stage, we apply a triangular meshing on the geometry, as shown in figure 4.6. The mesh element dimension was allowed to vary between 3×10^{-5} cm (near the source) to 0.26 cm elsewhere.

4.3.2.5 Solver and interpolation functions

We make use of the implicit Backward Differentiation Formula (BDF) of order 4 as the choice of time-dependent solver with a manual time stepping of 0.5 s. In choosing the

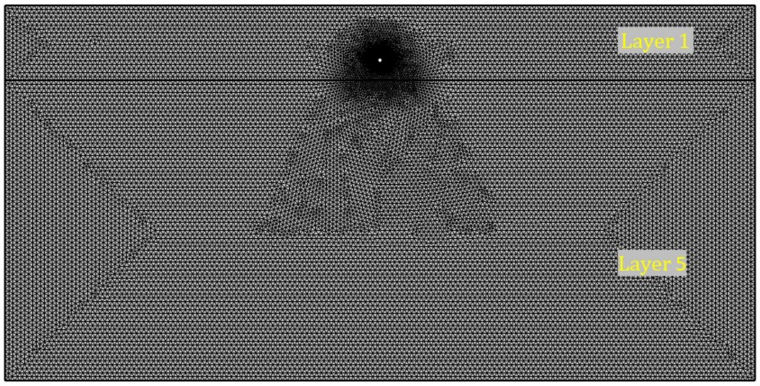

Figure 4.6: Meshed geometry.

interpolation functions defined at the nodal values of each element, we choose cubic polynomial for the pressure and a quadratic polynomial for the species concentration.

4.4 Results and discussion

4.4.1 Qualitative comparison between theory and simulation

By choosing a specific case from table 4.1, we perform simulations by progressively added layers. As an example, selecting the permeabilities of layers corresponding to Case 2 and maintaining each of the permeability jump between the layers horizontal ($\theta = 0°$), simulations are performed for two-, three-, four- and five-layers configurations, as illustrated in figure 4.7 a-d. To start with, a simulation is performed for a two-layered configuration, i.e. corresponding to Case 2 of table 4.1a – see figure 4.7 a. Later on, Layers 2, 3 and 4 of constant thicknesses are added between Layers 1 and 5, i.e. corresponding to Case 2 table 4.1 b-d – see figures 4.7 b-d.

For each of the above layered configurations, the outer envelope predicted by our theory (indicated as black profile) is also plotted and is observed to agree well with the simulation results[1]. However, in simulations, partly due to the transient effects

---

[1] For the sake of simplicity, we perform all our numerical simulations in dimensional units. Therefore, for qualitative comparisons, theoretical results were expressed and compared with numerical outputs in dimensional form. However, for quantitative comparisons, we non-dimensionalize the

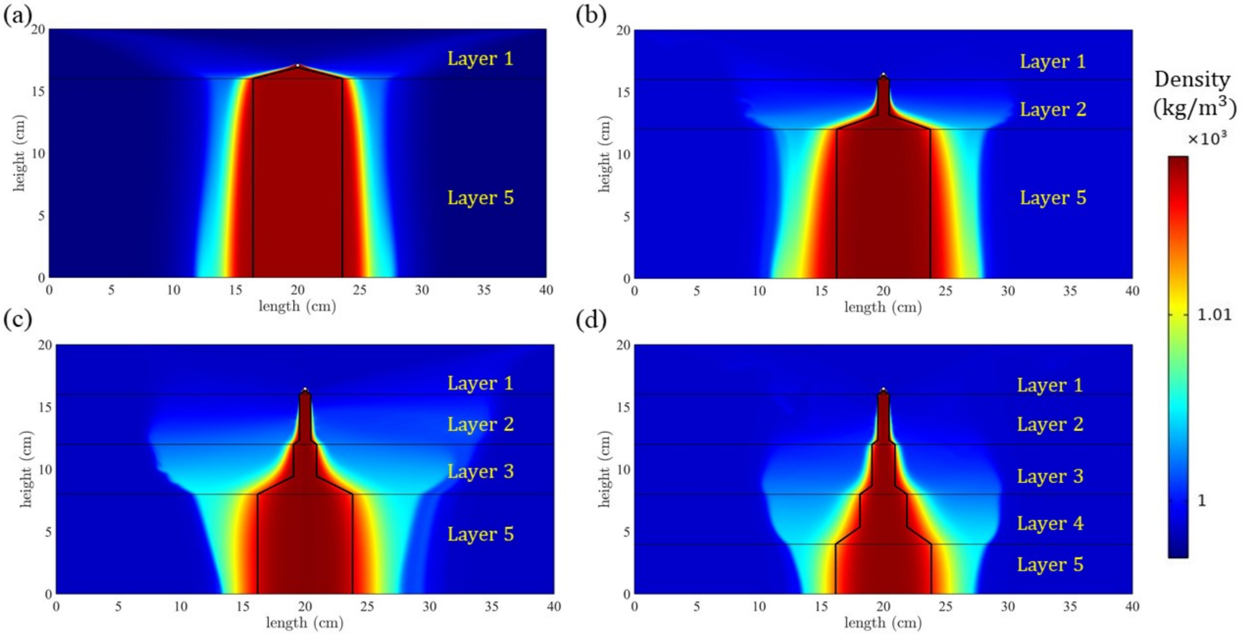

Figure 4.7: [Color] Steady-state results of numerical simulation corresponding to Case 2 for porous media configuration with (a) Two-layers, (b) Three-layers, (c) Four-layers, and (d) Five-layers. Permeability jump angles in all the case are 0°. The density colorbar is indicated on the right side. Also, for comparison, the theoretical prediction (in black contour) is plotted on each of the plots.

and partly due to the solute diffusion, the interface between the source and the ambient fluid is not sharp and a transition is seen as the color band varies gradually from red (source fluid) to light-blue and finally to dark-blue color (ambient fluid)[2]. Strictly speaking, the flow does not achieve steady state owing to diffusive effects which cause a continual mixing of source and ambient fluids. On the other hand, we find that, after some time, the envelope encompassing the bulk fluid stops expanding. We wish to determine the dimensions and lateral extent of this envelope and do so with reference to the average density between the source and ambient fluids. The procedure adopted is discussed below in Appendix C.2 in relation to section 4.4.2. Similar type comparison is also made by tilting the permeability jump by some fixed amount (i.e. $\theta = 3°$ or $6°$), in each of the layers. The results corresponding to $\theta = 6°$

---

parameters of interest.

[2] During the transient phase and in the absence of dispersion, gravity induced fingering instabilities were observed in each of the layers during the downward motion of the source fluid.

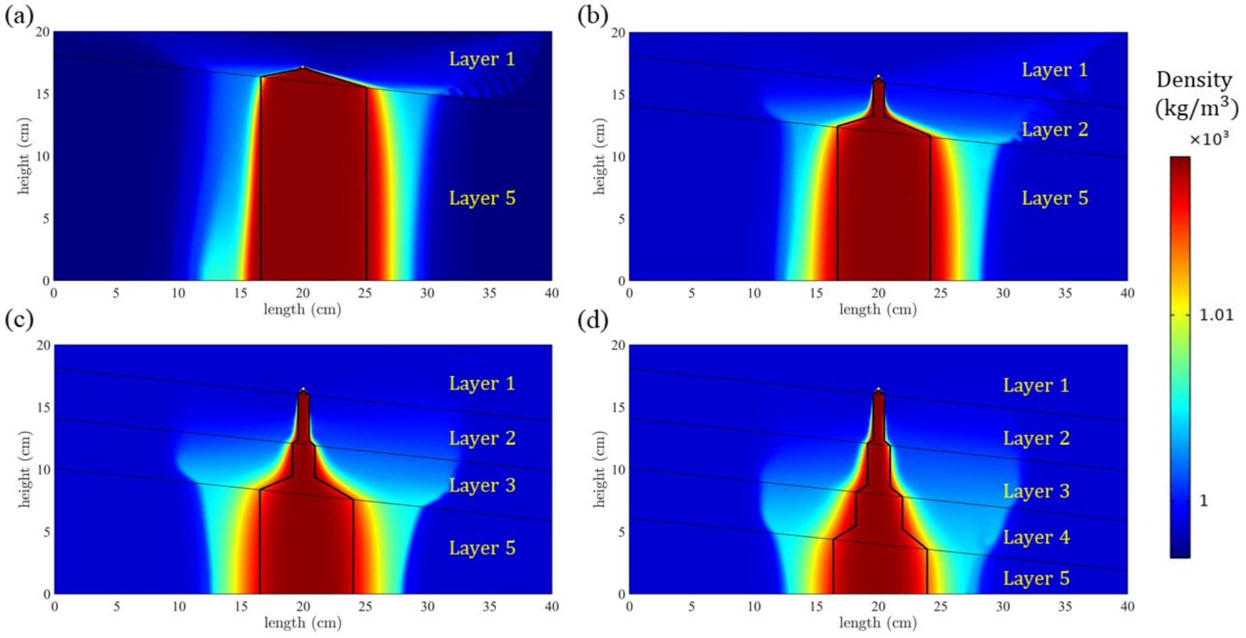

Figure 4.8: [Color] Steady-state results of numerical simulation corresponding to Case 2 for porous media configurations with (a) Two-layers, (b) Three-layers, (c) Four-layers, and (d) Five-layers. Permeability jump angles in all the case are 6°. The density colorbar is indicated on the right side. Also, for comparison, the theoretical prediction (in black contour) is plotted on each of the plots.

with five-layers for Case 2 is shown in figure 4.8. Even for inclined permeability jumps our theoretical model shows a good agreement of the outer envelope with the simulation result. In contrast to the above simulations which are performed for equal permeability jump angles in each of the layers, simulations are also carried out for Case 2 by selecting random inclination angles of the permeability jump in each of the layers, as shown in the figure 4.9. Here too, the outer envelope comparison with the theory is in good agreement.

In all the above comparative cases, the simulations results that are compared with theoretical predictions are for layers with decreasing values of permeabilities, i.e. $k_1 > k_2 > k_3 > k_4 > k_5$. However, for a special case when the layers are interchanged, i.e. when low permeability layer is placed above the high permeability layer, the simulation results are discussed in Appendix C.1.

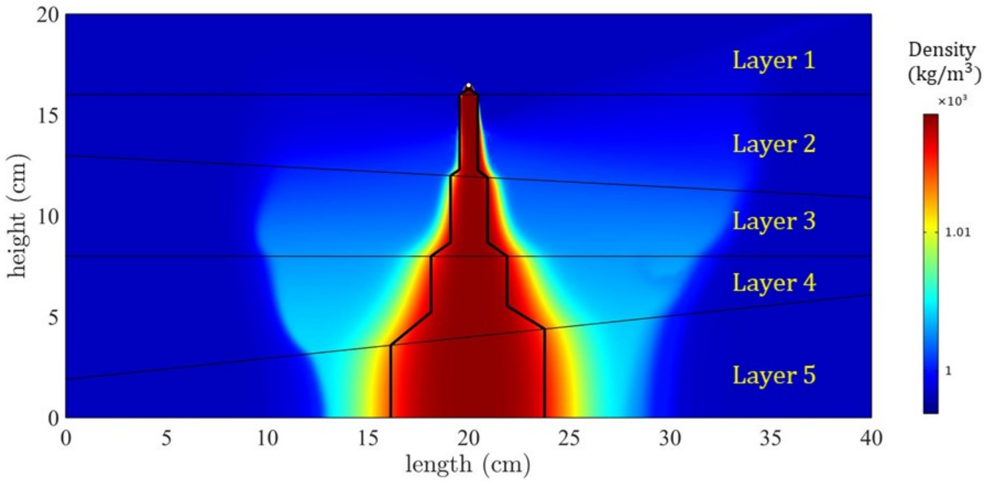

Figure 4.9: [Color] Steady-state result of numerical simulation for porous media having five-layers (corresponding to Case 2) with the permeability jump angles at the bottom of Layer 2 and Layer 4 are inclined at an angle of 3° and −6°, respectively. Also, for comparison, the theoretical prediction (in black contour) is plotted.

4.4.2 Quantitative comparison between theory and simulation

The lateral spreading distance of the source fluid is obtained by measuring the difference in up- and downdip runout lengths along a given permeability jump boundary. The method of determining the runout distances from COMSOL simulations is discussed in Appendix C.2. The total (non-dimensional) expanse of each gravity current is estimated from the relation $\Delta x^*_{N,\mathrm{ro}} = x^*_{N_d,\mathrm{ro}} + x^*_{N_u,\mathrm{ro}}$. In the interest of comparing the maximum expanse of the runout, $(\Delta x^*_{N,\mathrm{ro}})_{\max}$, (as indicated in figure 4.2) for all the layer configurations presented in this study, is measured along the bottom most permeability jump, which is clearly evident in figures 4.7-4.9.

We plot $(\Delta x^*_{N,\mathrm{ro}})_{\max}$ as predicted by the simulations (marked as open symbols) as a function of layer configuration, i.e. two-layers (1/5), three-layers (1/2/5), four-layers (1/2/3/5) and five-layers (1/2/3/4/5), in figure 4.10. The subplots a, b, c and d correspond to permeability jump angles of $\theta = 0°$, 3°, 6° and mixed-combination of θ, respectively. In each of the subplots, comparisons are made between the cases

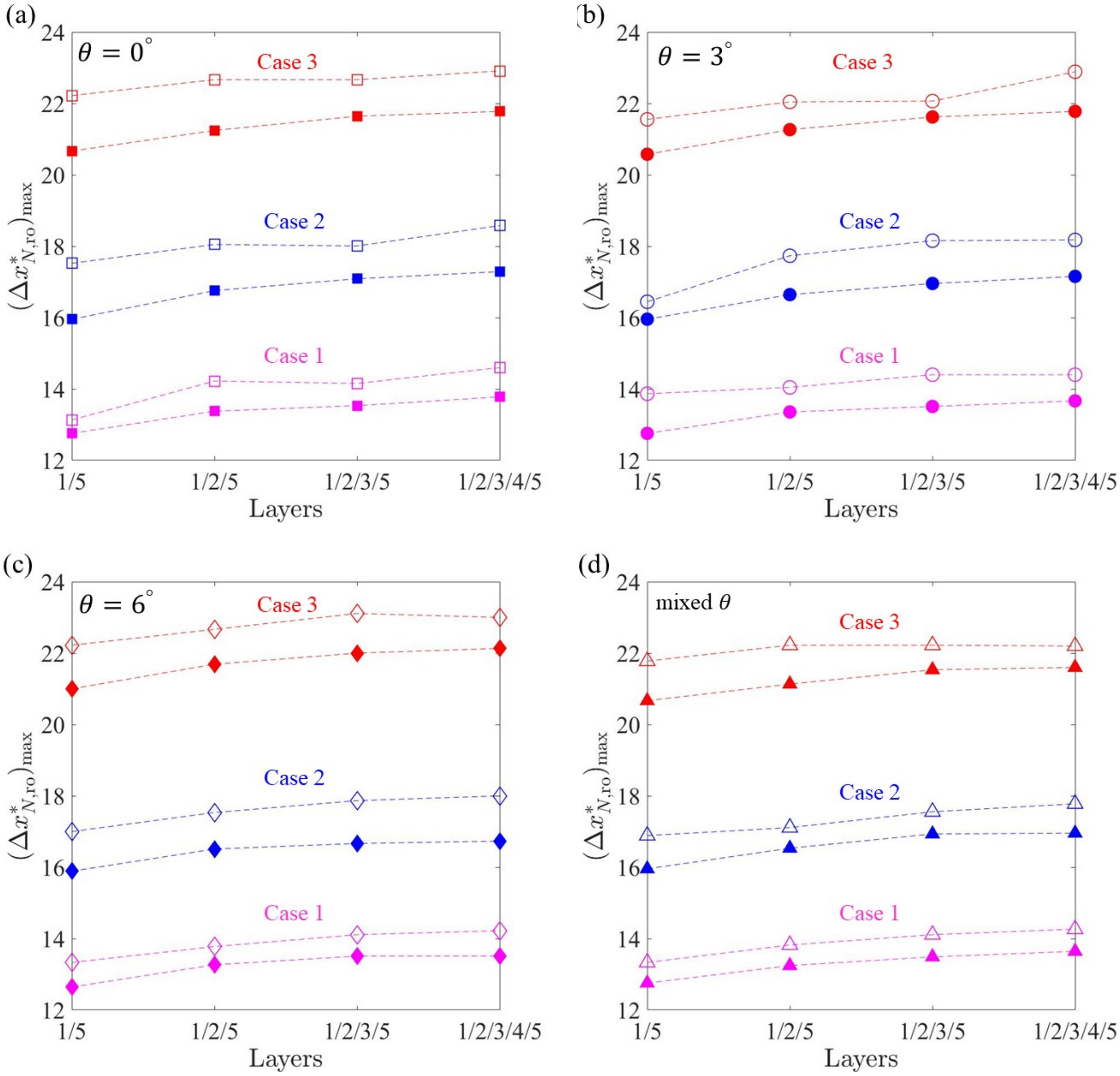

Figure 4.10: [Color] Maximum expanse of the runout, $(\Delta x^*_{N,\mathrm{ro}})_{\max}$, as a function of layer configurations, i.e. two-layers (1/5), three-layers (1/2/5), four-layers (1/2/3/5) and five-layers (1/2/3/4/5). We consider permeability jump angles of (a) $\theta = 0°$, (b) $\theta = 3°$, (c) $\theta = 6°$, and (d) mixed-combination of θ as selected in figure 4.9. Comparisons are made between the theory (closed symbols) and simulation (open symbols) predictions for all the three cases described in table 4.1.

described in table 4.1. Furthermore, $(\Delta x^*_{N,\mathrm{ro}})_{\max}$ as predicted by our theoretical model (marked as closed symbols) is also plotted for each of the cases. In comparing theoretical vs. numerical estimates of $(\Delta x^*_{N,\mathrm{ro}})_{\max}$, we find that latter is always greater than the former with a deviation ranging between 4% and 12%. It can be seen that

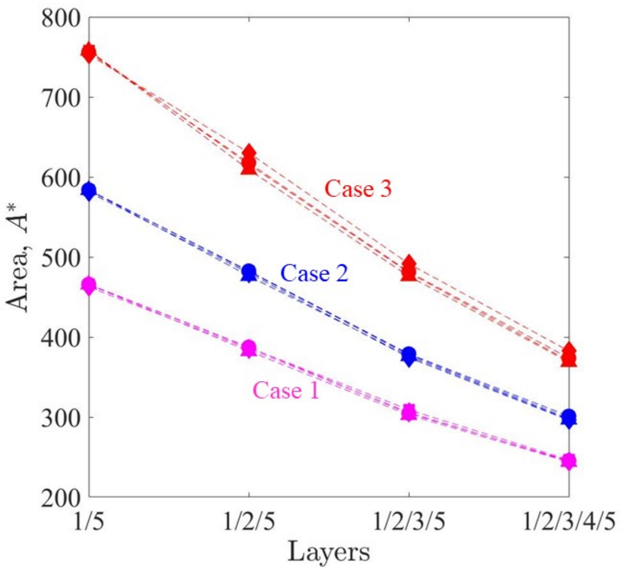

Figure 4.11: Dimensionless area, A^*, as a function of layer configuration, i.e. two-layers (1/5), three-layers (1/2/5), four-layers (1/2/3/5) and five-layers (1/2/3/4/5). Comparison is made between three different angles, i.e. 0° (square), 3° (circle), 6° (diamond) and mixed-combination of θ (upper-triangle), for all the three cases described in table 4.1.

for a particular case, $(\Delta x^*_{N,\mathrm{ro}})_{\max}$ varies weakly when additional layers are included in between the layers of maximum and minimum permeabilities. Also, $(\Delta x^*_{N,\mathrm{ro}})_{\max}$ remains nearly invariant with the inclination of the permeability jumps. However, $(\Delta x^*_{N,\mathrm{ro}})_{\max}$ is a strong function of ratio of maximum and minimum permeabilities, as evident in the comparison made between each of the three cases from any of figures 4.10 a,b,c or d.

Figure 4.10 gives the impression that the layer configuration has only a relatively small impact on the dynamics of the flow. While this is true when considering the maximum expanse of the contaminated fluid, figures 4.7–4.8 makes clear that the total volume of contaminated fluid stored in the layered porous medium must decrease as more intervening layers are added between Layer 1 and Layer 5. To characterize the variation of this volume, we introduce a non-dimensional parameter, A^*, defined as the total storage area occupied by the injected fluid and is measured when the flow reaches a steady-state. In other words, A^* is an indicator of the storage efficiency of the porous medium to store the fluid that is being injected into a porous space of fixed outer dimensions. Figure 4.11 shows the non-dimensional area, A^*, as a function of layer configurations. Since our theoretical model predictions are in reasonably good agreement with numerical predictions, we calculate A^* by estimating the area under the outer envelope from the theory alone. In contrast to figure 4.10, figure 4.11 confirms that A^* shows a strong variation with layer configuration. For a specific case, A^* decreases (almost linearly) with the addition of layers, however, the inclination angles of the permeability jump essentially make no impact on the storage area. This is because, for inclined permeability jump angles, reduced fraction of flow on the updip side is compensated with an increased flow on the downdip side. Therefore, and at steady-state, whatever runout length we lose on the updip side by increasing θ we gain on the downdip side.

4.5 Discussion and conclusions

Recalling the transient equations of gravity currents derived in Chapter 2, we developed a steady-state mathematical model that predicts the flow pattern inside a multi-layered porous media. The convection source is located at the first permeability jump (in the topmost layer). The boundary conditions, i.e. volume flux, at the other permeability jumps are resolved separately. In doing so, (4.8) suggest that gravity currents are formed at any given permeability jump whenever the ratio of the permeabilities between the lower and the upper layer is less than unity. Therefore, in the limit of our model predictions the layers must exist in a decreasing order of the permeabilities. Later, we employ finite-difference method in solving the final dimensionless equations in (4.14)–(4.17).

We also carry out numerical simulations using an FE based multiphysics COMSOL simulator. To be consistent with our theoretical model, we performed all our simulations for decreasing order of layer permeabilities, and therefore, selected three different cases with different ratios of permeabilities between the bottommost and topmost layers, i.e. for Case 1, this ratio is 0.079; for Case 2, it is 0.063 and for Case 3, it is 0.049, and by adding up to a maximum of five in between distinct layers. In general, the outer envelope comparisons made between our theory predictions and simulation results were in reasonably good agreement for all multi-layered combinations and sloping permeability jumps[3] – see figures 4.7-4.9. The maximum expanse of runout distances was measured and compared for 2-, 3-, 4- and 5-layer configurations of the porous medium, for each of the cases and also by setting the permeability jumps angles to 0°, 3° and 6°. The maximum runout expanse showed greater response to permeability ratios (three cases) compared to that when layers where either added or removed – see figures 4.7 and 4.8. The maximum runout expanse remained invariant with permeability jump angle – see figure 4.10. The effect of adding or removing layers greatly affected the storage area, wherein, the area occupied by the source fluid shows a near linear decrease as more layers are included – see figure 4.9. However, inclination angle of the permeability jumps showed essentially no impact on the storage area.

The flow patterns predicted in this study can indirectly be compared to the simulation carried out by Feldmann *et al.* (2016), who investigated the injection of hydrogen in a multi-layered porous media configuration with layers of different permeabilities – see their figure 5.

It is noteworthy to mention, the nature of this study is constrained by few assumptions. For instance, we have assumed that interface of the gravity current is always sharp in our theoretical model, and also in the interest of validating our theory predictions we have turned-off dispersion in all our COMSOL simulations. However, this

---

[3] Comparisons between numerical simulation and experiments, for both one- and two-layered porous media configurations, are being carried out by a current PhD student, in my research group. As an extended study, dispersion effects are also being included in the simulations in question. The comparisons made with the experimental cases show good agreement in the flow front profiles. More detailed explanation on the comparisons will be provided in this student's future publications or thesis report.

is not always true, because, the flow front significantly experiences the effects due to hydrodynamic dispersion as evident from the snapshot images in figure 2.8 of Chapter 2. The occurrence of dispersion may alter the character of the flow patterns. Also, in our theoretical model, we do not consider the dynamical effects of the gravity currents formed in the lower layers on the gravity currents formed in the layers above.

Chapter 5

Conclusions and future work

5.1 Summary and conclusions

A detailed and comprehensive study on buoyancy-driven flows in a multi-layered porous media is carried out by making use the three different modeling approaches, i.e. theory, CFD simulations and laboratory experiments. Our laboratory experiments, adhering to the methodology of a filling box model, have provided considerable insights and quantitative information about physical processes, which otherwise be rather be difficult to predict independently using theory or numerical technique. By suitably making use of the three approaches mentioned above, we have attempted to address the knowledge gaps that are highlighted in Chapter 1 of this thesis. Our initial investigation involved examining the early- and late-time dynamics of plume fluid being injected into a basic configuration of multi-layered porous media, i.e. having only two-layers that are separated by a sloping permeability jump boundary. The analysis in question constitutes Chapter 2 and Chapter 3 of the report. Later, the study was extended to a general case of multi-layered porous media configuration, which forms Chapter 4. To summarize:

In Chapter 2, we have predicted the early-time spreading dynamics of the gravity currents propagating along an inclined permeability jump with simultaneous basal draining into a deep lower layer. As a part of the theoretical model, we derive in analytical form a pair of coupled non-linear advection equations to be solved with a set of boundary conditions. This model accounts for the gradual change in density and volume influx at the inlet of the gravity current because we assume the source to be located at a certain height from the permeability jump. In doing so, we made of use of the plume equation derived by Sahu & Flynn (2015). In contrast to the horizontal permeability jump previously investigated by Goda & Sato (2011), the difference in the amount of discharged plume fluid flowing up- vs. downdip was resolved by including in the boundary conditions a time-dependent variable, f_a, that represents the fraction of fluid flowing downdip. We find that f_a is a monotone increasing function of time that attains a constant value when the up- and downdip gravity currents reach their runout lengths. This consequently led to the case of symmetry breaking up- and downdip gravity current flows, with respect to the source center. We solve the dimensionless governing equations by defining four key parameters namely the permeability jump angle, θ, plume source factor, δ, permeability ratio, K, and reduced gravity ratio, G'. The steady-state condition attained by the up- and downdip gravity currents, termed as the runout, is shown to be a function of these dimensionless parameters. For $0^\circ \leq \theta \leq 20^\circ$, runout lengths were predicted to occur when $t^* \gtrsim 10^2$. Furthermore, our experimental images reveal that a significant amount of flow dispersion occurs at the interface of the flow front due to mixing by hydrodynamic dispersion, which is most prominent along the flow directions. Therefore, we resolve and identify two phases of fluid, a part of the plume fluid least affected by mixing as "bulk" fluid, and the other region significantly affected by mixing as "dispersed" fluid, and the interface corresponding to each of these fluid phases as bulk- and dispersed interfaces, respectively. Furthermore, the amount of dispersion in the flow was quantified as a function of source conditions and permeability jump angles. The dynamics of along slope propagation of the gravity currents were compared between theory and experiments. Our theoretical model is based on the sharp interface assumption, and therefore, predicts the flow front as a single interface. At both transient- and steady-states, the nose positions of our theory always lie between the bulk and dispersed interface for all experiments, and in general, the predictions are close to bulk interface measurements than they are to the dispersed interface.

In real geological scenarios, the motion of the gravity currents advecting along-dip, as well as the basal draining fluid may get impeded by impermeable boundaries. In Chapter 3, and again in the spirit of a filling box flow, the case of two-layered porous media bounded by bottom and sidewall boundaries is considered. We built upon the studies of early-time dynamics of the gravity currents from Chapter 2, naming along permeability jump flows as "primary" gravity currents, and investigate the effects of limiting the depth of the lower layer. We demonstrated that for a finite lower layer depth, the draining fluid upon striking the bottom (impermeable) boundary leads to the formation of a pair of "secondary" gravity currents. As a consequence, there resulted in significant change in the dynamics of the primary gravity currents, such as, the occurrence of runout-override and remobilization. We have also paid utmost attention to details on the process by which the upper and lower layers fill with contaminated fluid. In the upper layer, filling follows from the up- and downdip propagation of the primary gravity currents, followed by vertical advection of the first front in the upward direction. Whereas, in the lower layer, filling primarily happens due to the advection of the secondary gravity currents that propagate along the bottom boundary. In addition, there is a contribution of leakage across the permeability jump, which leads to convection over a broader area. Furthermore, in categorizing the nature of filling of the two-layers, we distinguished between two modes described sequential and simultaneous. In sequential filling, most of the filling of the lower layer follows from the horizontal advection of the secondary gravity current. By contrast, and for simultaneous filling, proportionally more of the lower layer filling is by basal draining from the overlying primary gravity current. The parameter combinations conducive to one or the other filling regime were also identified. In the interest of determining the filling box time, i.e. the time required for the first front rising through the upper layer to very nearly reach the level of the plume source, we find that the inclination of the first front during the filling process makes it somewhat challenging to define this quantity unambiguously. Therefore, we considered two time bounds, one being the upper time bound and the other as the lower time bound, to estimate the filling box time. Then we examined the variation of these times as a function of the source conditions and permeability jump angles. It was observed that dispersion causes the difference in upper- and lower-time bounds to be larger when the source reduced gravity is comparatively smaller. During the filling process, we investigated the trajectory of the descending plume and the manner in which this varies with time due to the filling of the upper layer. It was observed that the plume deflected either up- or downdip depending on the source reduced gravity and the nozzle location relative to the sidewall boundary.

In the final component of this thesis, we have extended our investigation from a two-layered configuration to a general multi-layered configuration (more than two layers) in Chapter 4. Here, we have reduced the transient equations derived in Chapter 2 to obtain steady-state equations to predict the shape of the outer envelop associated with buoyant convection in the multi-layered geometry. The model solves for the equations of gravity currents at each of the permeability jump boundaries. A CFD simulation performed using COMSOL simulator was used to validate our theoretical predictions. Even though simulation results slightly overpredicted our theoretical predictions with a deviation ranging between 4% and 12%, overall, there was a good match to the outer envelope profile. However, our theoretical predictions are constrained by the fact that the porous layers starting from the point of source injection have to be arranged in a decreasing order of permeabilities. Taking this into account, we performed simulations for three different cases of lower to higher permeability ratios, i.e. 0.079, 0.063, 0.049. Furthermore, each of these cases was tested for geometries of two-, three-, four- and five-layers in configuration and for permeability jump angles of $\theta = 0°$, $3°$ and $6°$. In general, the maximum along-dip distance traveled by the contaminated (i.e. discharged plume) fluid was found to vary little with the number of layers but by a lot with the permeability reduction ratio. In contrast, the area occupied by the source fluid shows a linear decrease with layer addition. However, inclination angle showed no influence on the maximum runout span as well as on the storage area.

5.2 Primary contributions from the present work

The main findings and contributions of this thesis work can be summarized in the following major points:

- For inclined permeability jumps, our experiments suggest that the gravity currents propagating, both up- and downdip, along a permeable boundary experiences a greater amount of flow dispersion, especially on the downdip side for inclined permeability jumps. In particular, longitudinal dispersion (in the direction of the flow) was dominant compared to its transverse counterpart (perpendicular to the direction of the flow). Upon comparing our theoretical model, derived based on the sharp interface assumption, the predictions of the profile and nose position of the gravity currents, both up- and downdip, lies within the band of bulk and dispersed interfaces of our experiments. By this we have highlighted the limitation of the sharp interface assumption and emphasized the importance of considering flow dispersion in theoretical model for better predictions.

- We have investigated filling box flows, which serve as an analogue for studying closed porous media in a non-uniform porous medium having a single and sudden change in permeability. The associated flow study involves: (i) the relative dynamics between the primary and secondary gravity currents formed in the upper and lower layers, (ii) the filling process between the upper and lower layers, and (iii) estimating the filling box time(s), i.e. the time required for the first front rising through the upper layer to very nearly reach the level of the plume source.

- The effects of including layers of intermediate permeabilities on the flow pattern, maximum runout distance and the storage area were investigated. By including multiple layers in between any two-layers of fixed permeabilities, we observed that storage area decreases without significantly altering the maximum runout distance. The inclination angles made by the permeability jumps did not have any effect on either the maximum runout reached or the storage area.

5.3 Future Work

Primary topics for future studies are identified as follows:

- The gravity current flow is modeled, in this study and by several authors in the past, based on the sharp interface assumption. The sharp interface assumption means that the mixing is concentrated in a very narrow width at the interface of the two fluids and this width is very small compared with the length scale of the motion. However, making this assumption does not always yield accurate prediction of the flow front, especially for miscible fluids whose interface experiences a greater amount of hydrodynamic dispersion, in both transverse and longitudinal direction. This observation has been one of key highlights of this thesis. Therefore, it is very much important to consider dispersion effects while modeling gravity current flows. In this regard, in a very recent study by Sahu & Neufeld (2020), they modeled vertical entrainment into the gravity current by including transverse dispersivity into the equation of solute concentration. But they neglected the effects of horizontal entrainment. Our experimental images reveal that gravity currents propagating along a sloping boundary, especially downdip flows, are subjected to a greater amount of flow dispersion along the flow direction compared to the direction perpendicular – see snapshots of figure

2.8 in Chapter 2. Therefore, the effects of longitudinal dispersion also needs to be considered while modeling the gravity current flows.

- One of the key variables in the equations describing the up- and downdip motion of gravity currents along a permeability jump that dictates the magnitude of runout distances is the value of G'. It defines the degree of entrainment experienced by the draining fluid. Form experiments conducted by Sahu & Flynn (2017), they proposed the value of $G' = 0.6 \pm 0.1$ for the case of horizontal permeability jump and assuming $k_2/k_1 \ll 1$. In this study, from various experiments conducted for inclined permeability jumps, we established an empirical relation which suggests that G' is more a function of source conditions, i.e. the flow rate and reduced gravity, and less a function of the permeability jump angle. However, developing a theoretical relation to G' still remains an open challenge.

- In Chapter 3, filling box experiments were conducted considering an impermeable bottom boundary. Two pairs of gravity currents, the first pair is the primary gravity currents in the upper layer and the other being the secondary gravity currents in the lower layer, were observed. We analysed the eventual appearance of secondary gravity currents serves to remobilize the previously arrested primary gravity current. The theoretical approach to investigate this phenomenon of remobilization is left for the future study.

- The two filling modes identified in Chapter 3, were studied for the flow cases when buoyancy and viscosity were the dominant forces controlling fluid motion. However, there exist other scenarios where capillary trapping is expected to play a non-subordinate role (Golding *et al.*, 2011; Burnside & Naylor, 2014; Krevor *et al.*, 2015). In such cases, the degree of residual trapping was shown to be dissimilar for vertical and horizontal flows (Adebayo *et al.*, 2017). Because sequential and simultaneous filling are associated with different proportions of horizontal versus vertical flow, the details of the filling mode will, for this more general case of intermediate Bond number, influence the degree of residual trapping. Filling box dynamics for the fluid combinations having low or intermediate Bond numbers are yet to be investigated.

Bibliography

Acton, J. M., Huppert, H. E. & Worster, M. G. 2001 Two-dimensional viscous gravity currents flowing over a deep porous medium. *J. Fluid Mech.* **440**, 359–380.

Adebayo, A. R., Barri, A. A. & Kamal, M. S. 2017 Effect of flow direction on relative permeability curves in water/gas reservoir system: Implications in geological CO_2 sequestration. *Geofluids* **2017** (8), 1–10.

Ajayi, T., Gomes, J. S. & Bera, A. 2019 A review of CO_2 storage in geological formations emphasizing modeling, monitoring and capacity estimation approaches. *Pet. Sci.* **16** (5), 1028–1063.

Akhter, R. & Kaye, N. B. 2020 Experimental investigation of a line plume in a filling box. *Environ. Fluid Mech.* **20** (6), 1579–1601.

Bachu, S., Buschkuehle, B. E., Haug, K. & Michael, K. 2008*a* Subsurface Characterization of the Edmonton-Area Acid-Gas Injection Operations. *Tech. Rep.*. Energy Resources Conservation Board, ERCB/AGS Special Report 92.

Bachu, S., Buschkuehle, B. E., Haug, K. & Michael, K. 2008*b* Subsurface Characterization of the Pembina-Wabamun Acid-Gas Injection Area. *Tech. Rep.*. Energy Resources Conservation Board, ERCB/AGS Special Report 93.

Bachu, S. & Gunter, W. D. 2004 Acid-gas injection in the Alberta basin, Canada: A CO_2 -storage experience. *Geol. Soc. Spec. Publ.* **233** (Keushnig 1995), 225–234.

Baines, W. D. & Turner, J. S. 1969 Turbulent buoyant convection from a source in a confined region. *J. Fluid Mech.* **37** (1), 51–80.

Bear, J. 1972 *Dynamics of Fluids in Porous Media*. Dover Publications, Inc.

Bharath, K. S. & Flynn, M. R. 2021 Buoyant convection in heterogeneous porous media with an inclined permeability jump: an experimental investigation of filling box-type flows. *J. Fluid Mech.* **924**, 1–31.

Bharath, K. S., Sahu, C. K. & Flynn, M. R. 2020 Isolated buoyant convection in a two-layered porous medium with an inclined permeability jump. *J. Fluid Mech.* **902**, 1–31.

Boait, F. C., White, N. J., Bickle, M. J., Chadwick, R. A., Neufeld, J. A. & Huppert, H. E. 2012 Spatial and temporal evolution of injected CO_2 at the Sleipner Field, North Sea. *J. Geophys. Res. Solid Earth* **117** (3), 1–21.

Bridger, D. W. & Allen, D. M. 2010 Heat transport simulations in a heterogeneous aquifer used for aquifer thermal energy storage (ATES). *Can. Geotech. J.* **47** (1), 96–115.

Bryant, S. L., Lakshminarasimhan, S. & Pope, G. A. 2008 Buoyancy-dominated multiphase flow and its effect on geological sequestration of CO_2. *SPE J.* **13** (4), 447–454.

Burnside, N. M. & Naylor, M. 2014 Review and implications of relative permeability of CO_2/brine systems and residual trapping of CO_2. *Int. J. Greenh. Gas Control* **23**, 1–11.

Buschkuehle, B. E. 2005 Geological trapping of acid gas injected underground in Western Canada. *Greenh. Gas Control Technol.* (780), 1023–1028.

Carman, P. G. 1937 Fluid flow through granular beds. *Chem. Eng. Res. Des.* **75**, S32–S48.

Caulfield, C. P. & Woods, A. W. 2002 The mixing in a room by a localized finite-mass-flux source of buoyancy. *J. Fluid Mech.* **471**, 33–50.

Clennell, M. B. 1997 Tortuosity: a guide through the maze. *Geol. Soc. Spec. Publ.* **122** (122), 299–344.

Cohen, R. M. & Mercer, J. W. 1993 DNAPL Site Evaluation. *Tech. Rep.*.

Comiti, J. & Renaud, M. 1989 A new model for determining mean structure parameters of fixed beds from pressure drop measurements: application to beds packed with parallelepipedal particles. *Chem. Eng. Sci.* **44** (7), 1539–1545.

Cowton, L. R., Neufeld, J. A., White, N. J., Bickle, M. J., White, J. C. & Chadwick, R. A. 2016 An inverse method for estimating thickness and volume with time of a thin CO_2-filled layer at the Sleipner Field, North Sea. *J. Geophys. Res. Solid Earth* **121** (7), 5068–5085.

Cushman, J. H., Tartakovsky, D. M. & Delleur, J. W. 2016 *Elementary Groundwater Flow and Transport Processes*.

De Loubens, R. & Ramakrishnan, T. S. 2011 Analysis and computation of gravity-induced migration in porous media. *J. Fluid Mech.* **675**, 60–86.

Delgado, J. M. P. Q. 2007 Longitudinal and transverse dispersion in porous media. *Chem. Eng. Res. Des.* **85** (9 A), 1245–1252.

Dong, W. & Selvadurai, A. P. S. 2006 Image processing technique for determining the concentration of a chemical in a fluid-saturated porous medium. *Geotech. Test. J.* **29** (5), 385–391.

Dullien, F. A. L. 1979 *Porous media: Fluid transport and pore structure*. Academic Press, Inc.

Emam, E. A. 2015 GAS flaring in industry: An overview. *Pet. Coal* **57** (5), 532–555.

Espinoza, D. N. & Santamarina, J. C. 2017 CO_2 breakthrough—Caprock sealing efficiency and integrity for carbon geological storage. *Int. J. Greenh. Gas Control* **66** (September), 218–229.

European Commission 2015 *The Role of Gas Storage in Internal Market and in Ensuring Security of Supply*.

Farcas, A. & Woods, A. W. 2009 The effect of drainage on the capillary retention of CO_2 in a layered permeable rock. *J. Fluid Mech.* **618**, 349–359.

Farcas, A. & Woods, A. W. 2013 Three-dimensional buoyancy-driven flow along a fractured boundary. *J. Fluid Mech.* **728**, 279–305.

Feldmann, F., Hagemann, B., Ganzer, L. & Panfilov, M. 2016 Numerical simulation of hydrodynamic and gas mixing processes in underground hydrogen storages. *Environ. Earth Sci.* **75** (16), 1–15.

Fitts, C. R. 2013 *Groundwater Contamination.*

Fitts, J. P. & Peters, C. A. 2013 Caprock fracture dissolution and CO_2 leakage. *Rev. Mineral. Geochemistry* **77** (1), 459–479.

Flett, M. A., Gurton, R. M. & Taggart, I. J. 2005 Heterogeneous saline formations: Long-term benefits for geo-sequestration of greenhouse gases. In *Greenh. Gas Control Technol. 7* (ed. E. S. Rubin, D. W. Keith, C. F. Gilboy, M. Wilson, T. Morris, J. Gale & K. Thambimuthu), pp. 501–509. Oxford: Elsevier Science Ltd.

Freeze, A. R. & Cherry, J. A. 1979 *Groundwater*. Prentice-Hall, Inc.

Ghanbarian, B., Hunt, A. G., Ewing, R. P. & Sahimi, M. 2013 Tortuosity in Porous Media: A Critical Review. *Soil Sci. Soc. Am. J.* **77** (5), 1461–1477.

Goda, T. & Sato, K. 2011 Gravity currents of carbon dioxide with residual gas trapping in a two-layered porous medium. *J. Fluid Mech.* **673**, 60–79.

Golding, M. J., Neufeld, J. A., Hesse, M. A. & Huppert, H. E. 2011 Two-phase gravity currents in porous media. *J. Fluid Mech.* **678**, 248–270.

Hagemann, B., Panfilov, M. & Ganzer, L. 2016 Multicomponent gas rising through water with dissolution in stratified porous reservoirs - Application to underground storage of H_2 and CO_2. *J. Nat. Gas Sci. Eng.* **31**, 198–213.

Happel, J. & Brenner, H. 1983 *Low Reynolds number hydrodynamics, 1965*.

Heinemann, N., Alcalde, J., Miocic, J. M., Hangx, S. J., Kallmeyer, J., Ostertag-Henning, C., Hassanpouryouzband, A., Thaysen, E. M., Strobel, G. J., Schmidt-Hattenberger, C., Edlmann, K., Wilkinson, M., Bentham, M., Stuart Haszeldine, R., Carbonell, R. & Rudloff, A. 2021 Enabling large-scale hydrogen storage in porous media-the scientific challenges. *Energy Environ. Sci.* **14** (2), 853–864.

Hesse, M. A. & Woods, A. W. 2010 Buoyant dispersal of CO_2 during geological storage. *Geophys. Res. Lett.* **37** (1), 1–5.

Hewitt, D. R., Neufeld, J. A. & Lister, J. R. 2014 High Rayleigh number convection in a porous medium containing a thin low-permeability layer. *J. Fluid Mech.* **756** (6), 844–869.

Hewitt, D. R., Peng, G. G. & Lister, J. R. 2020 Buoyancy-driven plumes in a layered porous medium. *J. Fluid Mech.* **883**.

Homsy, G. M. 1987 Viscous Fingering in Porous Media. *Annu. Rev. Fluid Mech.* **19** (1987), 271–311.

Hughes, G. O. & Griffiths, R. W. 2006 A simple convective model of the global overturning circulation, including effects of entrainment into sinking regions. *Ocean Model.* **12** (1-2), 46–79.

Huling, S. G. & Weaver, J. W. 1991 Ground water issue: Dense nonaqueous phase liquids. *United States Environ. Prot. Agency* pp. 1–21.

Huppert, H. E. & Neufeld, J. A. 2014 The Fluid Mechanics of Carbon Dioxide Sequestration. *Annu. Rev. Fluid Mech.* **46** (1), 255–272.

Huppert, H. E. & Woods, A. W. 1995 Gravity-Driven Flows in Porous Layers. *J. Fluid Mech.* **292**, 55–69.

Ibrahim, D. & Rosen, M. A. 2010 *Thermal Energy Storage: Systems and Applications*. John Wiley & Sons, Ltd.

Jing, J., Yang, Y., Tang, Z. & Wang, F. 2019 Impacts of salinity on CO_2 spatial distribution and storage amount in the formation with different dip angles. *Environ. Sci. Pollut. Res.* **26** (22), 22173–22188.

Kamath, R., Connor, J. A., McHugh, T. E., Nemir, A., Le, M. P. & Ryan, A. J. 2012 Use of Long-Term Monitoring Data to Evaluate Benzene, MTBE, and TBA Plume Behavior in Groundwater at Retail Gasoline Sites. *J. Environ. Eng.* **138** (4), 458–469.

Khondaker, A. N., Al-Layla, R. I. & Husain, T. 1990 Groundwater Contamination Studies — The State-of-the-Art. *Crit. Rev. Environ. Control* **20** (4), 231–256.

Kohl, A. L. & Nielsen, R. B. 1997 Sulfur Recovery Processes. *Gas Purif.* pp. 670–730.

Krevor, S., Blunt, M. J., Benson, S. M., Pentland, C. H., Reynolds, C., Al-Menhali, A. & Niu, B. 2015 Capillary trapping for geologic carbon dioxide storage - From pore scale physics to field scale implications. *Int. J. Greenh. Gas Control* **40**, 221–237.

Lackner, K. S. 2003 A Guide to CO_2 Sequestration. *Science (80-.).* **300** (June), 1677–1678.

Lee, J. H. W. & Chu, V. H. 2003 Inclined Buoyant Jet in Stagnant Environment. In *Turbul. Jets Plumes*, chap. 4, pp. 103–133. Boston, MA: Kluwer Academic Publisher.

Lee, K. S. 2013 *Green Energy and Technology*, 1st edn. Springer-Verlag London.

Lewis, R. & Roberts, P. M. 1984 *The Finite Element Method in Porous Media Flow*, nato asi s edn., , vol. 82. Springer, Dordrecht.

Liu, G. R. & Quek, S. S. 2003 *The Finite Element Method*. Oxford: Butterworth-Heinemann.

Lyle, S., Huppert, H. E., Hallworth, M., Bicle, M. & Chadwick, A. 2005 Axisymmetric gravity currents in a porous medium. *J. Fluid Mech.* **543**, 293–302.

MacKay, J. C. D. 2009 *Sustainable energy - Without the hot air*. UIT Cambridge Ltd.

MacMinn, C. W. & Juanes, R. 2013 Buoyant currents arrested by convective dissolution. *Geophys. Res. Lett.* **40** (10), 2017–2022.

MacMinn, C. W., Szulczewski, M. L. & Juanes, R. 2010 CO_2 migration in saline aquifers. Part 1. Capillary trapping under slope and groundwater flow. *J. Fluid Mech.* **662**, 329–351.

Manins, P. 1979 Turbulent buoyant convection from a source in a confined region. *J. Fluid Mech.* **91**, 765–781.

Mauret, E. & Renaud, M. 1997 Transport phenomena in multi-particle systems - I. Limits of applicability of capillary model in high voidage beds-application to fixed beds of fibers and fluidized beds of spheres. *Chem. Eng. Sci.* **52** (11), 1807–1817.

McPherson, B. & Matthews, V. 2013 A Ten Step Protocol and Plan for CCS Site Characterization, Based on an Analysis of the Rocky Mountain Region, USA. *Tech. Rep.*. University of Utah.

Metz, B., Davidson, O., de Coninck, H., Loos, M. & Meyer, L. 2005 *Special Report on Carbon Dioxide Capture and Storage*.

Michael, K., Golab, A., Shulakova, V., Ennis-King, J., Allinson, G., Sharma, S. & Aiken, T. 2010 Geological storage of CO_2 in saline aquifers-A review of the experience from existing storage operations. *Int. J. Greenh. Gas Control* **4** (4), 659–667.

Morgan, C. W., Kent, G. M., Seitz, G. G. & Novak, M. 2008 Glaciolacustrine stratigraphy, aquifer characterization and contaminant transport: A case study in South Lake Tahoe, California, USA. *Hydrogeol. J.* **16** (5), 981–994.

Morgan, K., Lewis, R. W. & Roberts, P. M. 1984 Solution of two-phase flow problems in porous media via an alternating-direction finite element method. *Appl. Math. Model.* **8** (6), 391–396.

Mouche, E., Hayek, M. & Mügler, C. 2010 Upscaling of CO_2 vertical migration through a periodic layered porous medium: The capillary-free and capillary-dominant cases. *Adv. Water Resour.* **33** (9), 1164–1175.

National Energy Technology Laboratory 2010 Carbon sequestration atlas of the United States and Canada - Third edition. *Tech. Rep.*.

Neufeld, J. A. & Huppert, H. E. 2009 Modelling carbon dioxide sequestration in layered strata. *J. Fluid Mech.* **625**, 353–370.

Neufeld, J. A., Vella, D. & Huppert, H. E. 2009 The effect of a fissure on storage in a porous medium. *J. Fluid Mech.* **639**, 239–259.

Neufeld, J. A., Vella, D., Huppert, H. E. & Lister, J. R. 2011 Leakage from gravity currents in a porous medium. Part 1. A localized sink. *J. Fluid Mech.* **666**, 391–413.

Nordbotten, J. M. & Celia, M. A. 2006 Similarity solutions for fluid injection into confined aquifers. *J. Fluid Mech.* **561**, 307–327.

Nordbotten, J. M., Kavetski, D., Celia, M. A. & Bachu, S. 2009 Model for CO_2 leakage including multiple geological layers and multiple leaky wells. *Environ. Sci. Technol.* **43** (3), 743–749.

Paksoy, H. & Beyhan, B. 2014 *Thermal energy storage (TES) systems for greenhouse technology*. Woodhead Publishing Limited.

Parker, M. E., Northrop, S., Valencia, J. A., Foglesong, R. E. & Duncan, W. T. 2011 CO_2 management at ExxonMobil's LaBarge field, Wyoming, USA. *Energy Procedia* **4**, 5455–5470.

Paterson, L. 1983 The implications of fingering in underground hydrogen storage. *Int. J. Hydrogen Energy* **8** (1), 53–59.

Pegler, S. S., Huppert, H. E. & Neufeld, J. A. 2016 Stratified gravity currents in porous media. *J. Fluid Mech.* **791**, 329–357.

Perkins, T. K. & Johnston, O. C. 1963 A Review of Diffusion and Dispersion in Porous Media. *Soc. Pet. Eng. J.* **3** (01), 70–84.

Perkins, T. K., Johnston, O. C. & Hoffman, R. N. 1965 Mechanics of Viscous Fingering in Miscible Systems. *Soc. Pet. Eng. J.* **5** (04), 301–317.

Phillips, O. M. 1991 *Flow and Reactions in Permeable Rocks*. Cambridge University Press.

Pritchard, D., Woods, A. W. & Hogg, A. J. 2001 On the slow draining of a gravity current moving through a layered permeable medium. *J. Fluid Mech.* **444**, 23–47.

Rayward-Smith, W. J. & Woods, A. W. 2011 Dispersal of buoyancy-driven flow in porous media with inclined baffles. *J. Fluid Mech.* **689**, 517–528.

Roes, M. A. 2014 Buoyancy-driven convection in a ventilated porous medium. *Tech. Rep.*. M.Sc. thesis, University of Alberta, Edmonton.

Rutqvist, J. 2012 The geomechanics of CO_2 storage in deep sedimentary formations. *Geotech. Geol. Eng.* **30** (3), 525–551.

Saffman, P. G. & Taylor, S. G. 1958 The penetration of a fluid into a porous medium or Hele-Shaw cell containing a more viscous liquid. *Proc. R. Soc. Lond. A.* **245** (1242), 312–329.

Sahu, C. K. & Flynn, M. R. 2015 Filling box flows in porous media. *J. Fluid Mech.* **782** (2015), 455–478.

Sahu, C. K. & Flynn, M. R. 2016 Filling Box Flows in an Axisymmetric Porous Medium. *Transp. Porous Media* **112** (3), 619–635.

Sahu, C. K. & Flynn, M. R. 2017 The Effect of Sudden Permeability Changes in Porous Media Filling Box Flows. *Transp. Porous Media* **119** (1), 95–118.

Sahu, C. K. & Neufeld, J. A. 2020 Dispersive entrainment into gravity currents in porous media. *J. Fluid Mech.* **886**, A5–1 – A5–21.

Sainz-Garcia, A. 2017 Dynamics of underground gas storage. Insights from numerical models for carbon dioxide and hydrogen. PhD thesis.

Speer, K. & Tziperman, E. 1990 Convection from a Source in an Ocean Basin. *Deep. Res.* **37**, 431–446.

Steelman, C. M., Meyer, J. R., Wanner, P., Swanson, B. J., Conway-White, O. & Parker, B. L. 2020 The importance of transects for characterizing aged organic contaminant plumes in groundwater. *J. Contam. Hydrol.* **235** (September).

Szulczewski, M. L. 2013 The Subsurface Fluid Mechanics of Geologic Carbon Dioxide Storage by. PhD thesis, Massachusetts Institute of Technology,.

Szulczewski, M. L. & Juanes, R. 2013 The evolution of miscible gravity currents in horizontal porous layers. *J. Fluid Mech.* **719**, 82–96.

Tang, Y., Yang, R. & Bian, X. 2014 A review of CO_2 sequestration projects and application in China. *Sci. World J.* **2014**, 1–11.

Tarkowski, R. 2019 Underground hydrogen storage: Characteristics and prospects. *Renew. Sustain. Energy Rev.* **105** (January), 86–94.

Torp, T. A. & Gale, J. 2004 Demonstrating storage of CO_2 in geological reservoirs: The Sleipner and SACS projects. *Energy* **29** (9-10), 1361–1369.

Van Stempvoort, D. R., Roy, J. W., Grabuski, J., Brown, S. J., Bickerton, G. & Sverko, E. 2013 An artificial sweetener and pharmaceutical compounds as co-tracers of urban wastewater in groundwater. *Sci. Total Environ.* **461-462**, 348–3359.

Vella, D. & Huppert, H. E. 2006*a* Gravity currents in a porous medium at an inclined plane. *J. Fluid Mech.* **555**, 353–362.

Vella, D. & Huppert, H. E. 2006*b* Gravity currents in a porous medium at an inclined plane. *J. Fluid Mech.* **555**, 353–362.

Vella, D., Neufeld, J. A., Huppert, H. E. & Lister, J. R. 2011 Leakage from gravity currents in a porous medium. Part 2. A line sink. *J. Fluid Mech.* **666**, 414–427.

Weaver, W. W. & Wilson, T. W. 2000 Diving Plumes and Vertical Hydrocarbon Release Sites. *LUSTLine Bull. 36* (November), 12–15.

Wooding, R. A. 1963 Convection in a saturated porous medium at large Rayleigh number or Peclet number. *J. Fluid Mech.* **15** (1961), 527–544.

Woods, A. W. 2014 *Flow in Porous Rocks Energy and Environmental Applications. In Flow in Porous Rocks: Energy and Environmental Applications*. Cambridge University Press.

Woods, A. W. & Farcas, A. 2009 Capillary entry pressure and the leakage of gravity currents through a sloping layered permeable rock. *J. Fluid Mech.* **618**, 361–379.

Woods, A. W. & Mason, R. 2000 The dynamics of two-layer gravity-driven flows in permeable rock. *J. Fluid Mech.* **421**, 83–114.

Wu, Y. & Carroll, J. J. 2011 *Acid Gas Injection and Related Technologies*. Scrivener Publishing LLC.

Yu, Y. E., Zheng, Z. & Stone, H. A. 2017 Flow of a gravity current in a porous medium accounting for drainage from a permeable substrate and an edge. *Phys. Rev. Fluids* **2** (7), 26.

Zheng, Z., Guo, B., Christov, I. C., Celia, M. A. & Stone, H. A. 2015 Flow regimes for fluid injection into a confined porous medium. *J. Fluid Mech.* **767**, 881–909.

Zheng, Z., Soh, B., Huppert, H. E. & Stone, H. A. 2013 Fluid drainage from the edge of a porous reservoir. *J. Fluid Mech.* **718**, 558–568.

Appendix A: Theory and experimental details

A.1 Derivation of the evolution equation for l

The contaminated fluid region is continuously fed by the draining of gravity current fluid along the permeability jump and also the ambient fluid entering across the contaminated-ambient fluid interface – see figure 2.2. The time rate of change in the mass of contaminated fluid is expressed mathematically as

$$\frac{\mathrm{d}}{\mathrm{d}t}\left(\bar{\rho_d}\int_{-x_{N_u}}^{x_{N_d}} \phi\, l \,\mathrm{d}x\right) = -\Big(\bar{\rho_c}\int_{-x_{N_u}}^{x_{N_d}} w_{\text{drain}}\,\mathrm{d}x + \rho_o\, q_{\text{entr}}\Big) \tag{A.1}$$

Expanding the time derivative term on the left-hand side of the above expression gives

$$\bar{\rho_d}\,\frac{\mathrm{d}}{\mathrm{d}t}\int_{-x_{N_u}}^{x_{N_d}} \phi\, l\,\mathrm{d}x + \frac{\mathrm{d}\bar{\rho_d}}{\mathrm{d}t}\int_{-x_{N_u}}^{x_{N_d}} \phi\, l\,\mathrm{d}x = -\Big(\bar{\rho_c}\int_{-x_{N_u}}^{x_{N_d}} w_{\text{drain}}\,\mathrm{d}x + \rho_o\, q_{\text{entr}}\Big) \tag{A.2}$$

For the conditions relevant to our analysis, the latter term from the left-hand side is three orders of magnitude smaller than the former term and can therefore be neglected. Applying Leibniz's rule in conjunction with the boundary conditions specified by (2.18) allows us to write

$$\bar{\rho_d}\int_{-x_{N_u}}^{x_{N_d}} \phi\,\frac{\partial l}{\partial t}\,\mathrm{d}x = -\Big(\bar{\rho_c}\int_{-x_{N_u}}^{x_{N_d}} w_{\text{drain}}\,\mathrm{d}x + \rho_o\, q_{\text{entr}}\Big) \tag{A.3}$$

Meanwhile if (A.1) is integrated in time,

$$\bar{\rho_d}\int_{-x_{N_u}}^{x_{N_d}} \phi\, l\,\mathrm{d}x = -\int_0^t \Big(\bar{\rho_c}\int_{-x_{N_u}}^{x_{N_d}} w_{\text{drain}}\,\mathrm{d}x\Big)\mathrm{d}t - \int_0^t \rho_o\, q_{\text{entr}}\,\mathrm{d}t \tag{A.4}$$

Note, however that the left-hand side of (A.4) denotes the total volume of contmainated fluid and can therefore be written as

$$\int_{-x_{N_u}}^{x_{N_d}} \phi\, l \,\mathrm{d}x = -\int_0^t \Big(\int_{-x_{N_u}}^{x_{N_d}} w_{\mathrm{drain}} \,\mathrm{d}x + q_{\mathrm{entr}} \Big) \mathrm{d}t \tag{A.5}$$

Substituting (A.5) in (A.4), we get

$$-\bar{\rho_d} \int_0^t \Big(\int_{-x_{N_u}}^{x_{N_d}} w_{\mathrm{drain}} \,\mathrm{d}x + q_{\mathrm{entr}} \Big) \mathrm{d}t = -\int_0^t \Big(\bar{\rho_c} \int_{-x_{N_u}}^{x_{N_d}} w_{\mathrm{drain}} \mathrm{d}x \Big) \mathrm{d}t - \int_0^t \rho_o \, q_{\mathrm{entr}} \,\mathrm{d}t \tag{A.6}$$

Consistent with the previous argument it is appropriate to regard the time variation of $\bar{\rho_d}$ as small whereby

$$\int_0^t \Big[-\bar{\rho_d} \Big(\int_{-x_{N_u}}^{x_{N_d}} w_{\mathrm{drain}} \,\mathrm{d}x + q_{\mathrm{entr}} \Big) + \bar{\rho_c} \int_{-x_{N_u}}^{x_{N_d}} w_{\mathrm{drain}} \,\mathrm{d}x + \rho_o \, q_{\mathrm{entr}} \Big] \mathrm{d}t = 0 \tag{A.7}$$

Because this results is valid for arbitrary t,

$$\bar{\rho_d} \Big(\int_{-x_{N_u}}^{x_{N_d}} w_{\mathrm{drain}} \,\mathrm{d}x + q_{\mathrm{entr}} \Big) = \bar{\rho_c} \int_{-x_{N_u}}^{x_{N_d}} w_{\mathrm{drain}} \,\mathrm{d}x + \rho_o \, q_{\mathrm{entr}} \tag{A.8}$$

Rearranging the terms in (A.8) and expressing q_{entr} in terms of w_{drain} yields

$$q_{\mathrm{entr}} = \frac{\Delta\bar{\rho_c} - \Delta\bar{\rho_d}}{\Delta\bar{\rho_d}} \int_{-x_{N_u}}^{x_{N_d}} w_{\mathrm{drain}} \,\mathrm{d}x \tag{A.9}$$

Combining this result with (A.3), we obtain the desired result, namely

$$\phi \frac{\partial l}{\partial t} = -\frac{\Delta\bar{\rho_c}}{\Delta\bar{\rho_d}} \, w_{\mathrm{drain}} \tag{A.10}$$

This last equation is, of course, the same as (2.10).

A.2 Method of solution

An explicit finite-difference algorithm is used to discretize (2.23-2.27). The variables corresponding to updip flow are denoted by a subscript u while those corresponding to downdip flow downdip are denoted by d. Thus equations (2.23-2.27) may be rewritten in discrete form as

$$\begin{aligned} h^{*\,n+1}_{ui} = h^{*\,n}_{ui} + \Big(\frac{1 - \delta h^{*\,n}_{u1} \cos\theta}{1 - \delta \cos\theta} \Big)^{-\frac{1}{4}} \Big[& \frac{\Delta t^* \cos\theta}{2\Delta x^{*2}} \big({h^{*\,n}_{ui-1}}^2 - 2h^{*\,n2}_{ui} + {h^{*\,n}_{ui+1}}^2 \big) \\ & + \frac{\Delta t^* \sin\theta}{2\Delta x^*} \big(h^{*\,n}_{ui-1} - h^{*\,n}_{ui+1} \big) - KG' \Big(1 + \frac{h^{*\,n}_{ui}}{l^{*\,n}_{ui}} \cos\theta \Big) \Delta t^* \Big] \end{aligned} \tag{A.11a}$$

$$l_{ui}^{*n+1} = l_{ui}^{*n} + \Big(\frac{1-\delta h_{u1}^{*n}\cos\theta}{1-\delta\cos\theta}\Big)^{-\frac{1}{4}} K\Big(1 + \frac{h_{ui}^{*n}}{l_{ui}^{*n}}\cos\theta\Big)\Delta t^* \tag{A.11b}$$

where n and i are non-negative integers, denoting the number of time-steps and the index of the discretized elements, respectively. Similarly, the discretized equations on the downdip side read

$$\begin{aligned} h_{di}^{*n+1} = h_{di}^{*n} + \Big(\frac{1-\delta h_{d1}^{*n}\cos\theta}{1-\delta\cos\theta}\Big)^{-\frac{1}{4}} \Big[\frac{\Delta t^*\cos\theta}{2\Delta x^{*2}}({h_{di-1}^{*n}}^2 - 2h_{di}^{*n2} + {h_{di+1}^{*n}}^2) \\ - \frac{\Delta t^*\sin\theta}{2\Delta x^*}(h_{di-1}^{*n} - h_{di+1}^{*n}) - KG'\Big(1 + \frac{h_{di}^{*n}}{l_{di}^{*n}}\cos\theta\Big)\Delta t^*\Big] \end{aligned} \tag{A.12a}$$

$$l_{di}^{*n+1} = l_{di}^{*n} + \Big(\frac{1-\delta h_{d1}^{*n}\cos\theta}{1-\delta\cos\theta}\Big)^{-\frac{1}{4}} K\Big(1 + \frac{h_{di}^{*n}}{l_{di}^{*n}}\cos\theta\Big)\Delta t^* \tag{A.12b}$$

For pragmatic reasons, and to avoid the appearance of unphysical singularities, we do not allow l_{ui}^{*n} and l_{di}^{*n} to be identically zero, but rather initialize with some small value.

The expressions in (A.11) and (A.12) apply for $i \geq 1$. When $i = 1$, h_{u0}^{*n} and h_{d0}^{*n} are resolved with reference to the influx boundary condition in (2.25), such that

$$(h_{u0}^{*n})^2 = (h_{u2}^{*n})^2 + 4\Delta x^* h_{u1}^{*n}\tan\theta + \Big[\frac{4\Delta x^*(1-f_d)}{\cos\theta}\Big](1-\delta h_{u1}^{*n}\cos\theta) \tag{A.13a}$$

$$(h_{d0}^{*n})^2 = (h_{d2}^{*n})^2 - 4\Delta x^* h_{d1}^{*n}\tan\theta + \Big(\frac{4\Delta x^* f_d}{\cos\theta}\Big)(1-\delta h_{d1}^{*n}\cos\theta) \tag{A.13b}$$

Analogously, (2.26) becomes

$$h_{u1}^{*n} = h_{d1}^{*n} \tag{A.14}$$

Finally for $i = N_u$ and N_d, the nose positions up- and downdip in (2.27), we require that

$$h_{uN_u}^{*n} = h_{dN_d}^{*n} = 0 \tag{A.15a}$$

$$l_{uN_u}^{*n} = l_{dN_d}^{*n} = 0 \tag{A.15b}$$

Here, Δx^* and Δt^* denote the grid spacing and the time step, respectively. The values of Δx^* and Δt^* were respectively chosen as 2.5×10^{-2} and 0.5×10^{-3}. Grid independence checks were performed to ensure that the solutions were insensitive to

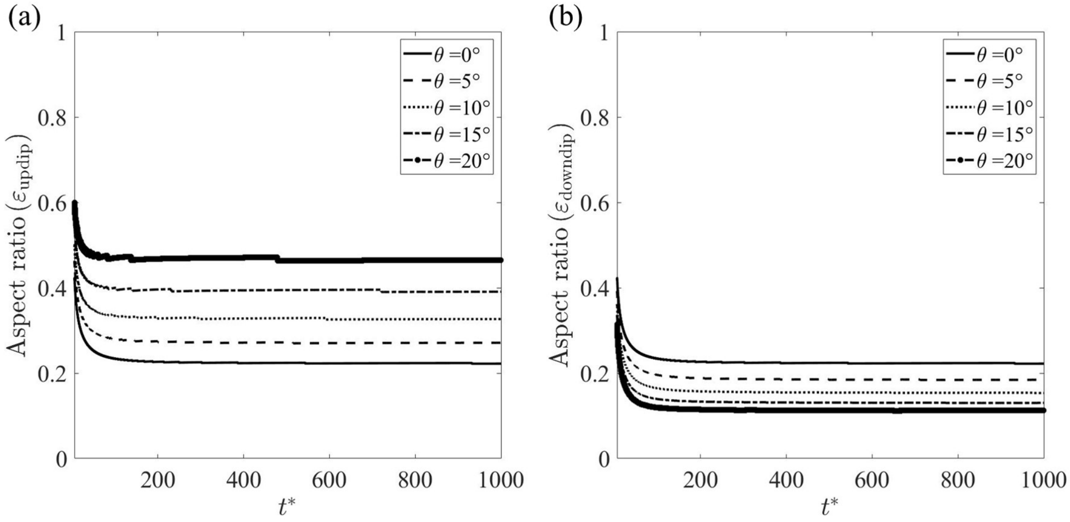

Figure A.1: Time variation of the gravity current aspect ratio on the (a) Updip side (left panel), and (b) Downdip side (right panel). Results are derived using (2.23) and assume $\delta = 0.1$, $K = 0.1$ and $G' = 0.4$.

the magnitude of Δx^*. For purposes of validating our numerical code, we confirmed that, in all cases, the prediction for up- and downdip runout lengths match those anticipated from (2.23) and (2.24) with $\partial h^*/\partial t^* = 0$. Results were also compared with those of Sahu & Flynn (2017) for the special case $\theta = 0°$.

A.3 Validation of Dupuit's approximation

Measured in the $x - z$ coordinate system of figure 2.2, the slopes of the up- and downdip gravity currents are found to be spatially uniform – see e.g. figure 2.3a. The gravity current slopes therefore prescribe the aspect ratios; symbolically, $\varepsilon = \partial h^*/\partial x^*$. In figure A.1, we plot these aspect ratios vs. time for various permeability jump angles, θ. The values of ε are found to be smaller than unity, i.e. they vary, in the long-time limit, between 0.22 and 0.46 on the updip side, and between 0.11 and 0.22 on the downdip side. Note that larger values for ε are realized at early times; however, this limit is of comparatively lesser significance of the context of self-similar models of the type described by our (2.23). Note also that for $\theta > 0°$, aspect ratios are larger updip because the nose travels a comparatively shorter distance before becoming arrested at runout.

The results of figure A.1 suggest that, in general, it is appropriate to consider the gravity currents as long and thin such that the along-jump component of velocity remains notably smaller than its across-jump counterpart. Under these circumstances, Dupuit's approximation can be considered to be valid such that pressure gradients can be considered hydrostatic as in (2.2).

A.4 Dye calibration and estimation of reduced gravities

A.4.1 Dye calibration procedure

The concentration of dye to be mixed into the source fluid was inferred from calibration experiments conducted in the general manner of Dong & Selvadurai (2006). These were performed to determine the correlation between the dye concentration and the pixel intensity. Separate correlations were, of course, derived for the upper and lower layers, which are comprised of glass beads of different diameters, and which therefore transmit a different fraction of the light from the overhead projector located behind the box of figure 2.7. Calibration experiments were carried out by completely filling the heterogeneous porous medium with dyed (fresh) water of known concentration after which images were collected using the Canon Rebel EOS T2i 18.0 PM camera. This process was repeated for various dye concentrations ranging from 0 to 0.14 g/L. The resulting data were used to construct calibration curves. We observe that, due to the smaller permeability of the lower layer, the pixel intensity saturates comparatively quickly. The dye concentration in all our experiments was therefore set by the shape of the lower layer calibration curve. Note finally that different calibration curves were constructed for different θ.

A.4.2 Estimation of reduced gravities

To determine values for $\bar{g'}_c$ and $\bar{g'}_d$, we defined two interrogation windows within experimental snapshot images, one each for the upper and lower layers. These windows could either encompass fluid within the bulk phase or within the dispersed phase. However, and when computing the value of G', we had to be consistent with the sharp interface assumption applied in section 2.3. As such, the interrogation windows in both the upper and lower layers were defined so that they enclosed only fluid within the bulk phase. Once the windows were defined, we then computed the pixel intensity averaged over area. The averaged values so obtained were compared with the corresponding calibration curves for the upper and lower layers. These calibration curves were obtained using the procedure described in appendix A.4.1 but were constructed specifically with reference to the above interrogation windows. In this fashion, we were able to convert from an average pixel intensity to an average dye concentration and then finally to an average salt concentration and fluid density, dye and salt having been mixed into the source fluid in fixed proportion. An implicit assumption in this latter step is that salt and dye are transported at roughly equal speeds, which is justified given the large Péclet numbers of interest here (Sahu & Flynn, 2017). By this procedure, we thereby estimate the average reduced gravities in the upper and lower layers separately.

A.5 Scaling of reduced gravitiy, g'_s

Realizing that expressing g'_s in dimensional form in the results is not always a good practise, we attempt to non-dimensionalize g'_s using the scaling term, $Q_s^2/A_{nozzle}^{5/2}$, where Q_s is the source flow rate and A_{nozzle} is the area of the nozzle whose value is $2.8\,\mathrm{cm}^2$. From the plot in figure A.2, even though g'_s scales differently for $Q_s = 1\,\mathrm{cm}^3/\mathrm{s}$ and $0.5\,\mathrm{cm}^3/\mathrm{s}$, we observe an approximately linear variation of G' with g'^*_s, with slightly different slopes for the flow rates considered. In the region of overlap between

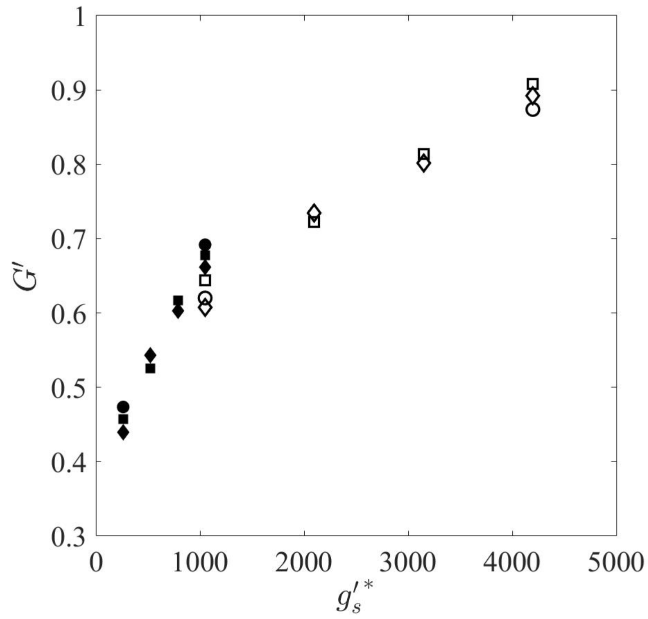

Figure A.2: Reduced gravity ratio G' vs. the source reduced gravity $g_s'^*$. The open symbols correspond to a source flow rate of $0.5\,\mathrm{cm}^3/\mathrm{s}$ while the solid symbols consider $1\,\mathrm{cm}^3/\mathrm{s}$. The square, circle and diamond symbols show $\theta = 0°$, $5°$ and $15°$, respectively.

the closed and open symbols, there is some offset between one and the other dataset. It remains to probe this offset in future experimental work e.g. by extending the closed symbols rightward or the open symbols leftward.

Appendix B: Experimental details

B.1 List of experiments

A summary of the laboratory experiments performed as part of this study is given in tabular form below.

Table B.1: List of laboratory experiments.

Expt.	θ (deg)	$Q_s \pm 0.02$ (cm^3/s)	$g'_s \pm 0.9$ (cm/s^2)	X_s^* $= X_s/L$	H_{lower}^* $= H_{\text{lower}}/H$	Filling mode (downdip)
E1	0	0.51	20.1	0.25	0.45	Sequential
E2	0	0.51	40.1	0.25	0.45	Sequential
E3	0	0.51	60.1	0.25	0.45	Sequential
E4	0	0.51	80.1	0.25	0.45	Sequential
E5	0	1.01	20.1	0.25	0.45	Simultaneous
E6	0	1.01	20.1	0.5	0.45	Simultaneous
E7	0	1.01	20.1	0.75	0.45	Simultaneous
E8	0	1.01	40.1	0.25	0.45	Simultaneous
E9	0	1.01	60.1	0.25	0.45	Simultaneous
E10	0	1.01	80.1	0.25	0.45	Sequential
E11	0	1.01	80.1	0.5	0.45	Sequential
E12	0	1.01	80.1	0.75	0.45	Simultaneous
E13	5	0.51	20.1	0.25	0.5	Sequential
E14	5	0.51	20.1	0.5	0.45	Sequential
E15	5	0.51	20.1	0.75	0.4	Simultaneous

continued on next page....

Table B.1 – continued from previous page

Expt.	θ (deg)	$Q_s \pm 0.02$ (cm^3/s)	$g_s' \pm 0.9$ (cm/s^2)	$X_s^* = X_s/L$	$H_{\text{lower}}^* = H_{\text{lower}}/H$	Filling mode (downdip)
E16	5	0.51	80.1	0.25	0.5	Sequential
E17	5	0.51	80.1	0.5	0.45	Sequential
E18	5	0.51	80.1	0.75	0.4	Simultaneous
E19	5	1.01	20.1	0.25	0.5	Simultaneous
E20	5	1.01	20.1	0.5	0.45	Simultaneous
E21	5	1.01	20.1	0.75	0.4	Simultaneous
E22	5	1.01	40.1	0.25	0.5	Simultaneous
E23	5	1.01	40.1	0.5	0.45	Simultaneous
E24	5	1.01	40.1	0.75	0.4	Simultaneous
E25	5	1.01	60.1	0.25	0.5	Simultaneous
E26	5	1.01	60.1	0.5	0.45	Simultaneous
E27	5	1.01	60.1	0.75	0.4	Simultaneous
E28	5	1.01	80.1	0.25	0.5	Sequential
E29	5	1.01	80.1	0.5	0.45	Simultaneous
E30	5	1.01	80.1	0.75	0.4	Simultaneous
E31	10	0.51	20.1	0.25	0.55	Sequential
E32	10	0.51	20.1	0.5	0.45	Sequential
E33	10	0.51	20.1	0.75	0.35	Simultaneous
E34	10	0.51	80.1	0.25	0.55	Sequential
E35	10	0.51	80.1	0.5	0.45	Sequential
E36	10	0.51	80.1	0.75	0.35	Simultaneous
E37	10	1.01	20.1	0.25	0.55	Simultaneous
E38	10	1.01	20.1	0.5	0.45	Simultaneous
E39	10	1.01	20.1	0.75	0.35	Simultaneous
E40	10	1.01	80.1	0.25	0.55	Sequential
E41	10	1.01	80.1	0.5	0.45	Simultaneous

continued on next page....

Table B.1 – continued from previous page

Expt.	θ (deg)	$Q_s \pm 0.02$ (cm^3/s)	$g'_s \pm 0.9$ (cm/s^2)	$X_s^* = X_s/L$	$H_{\text{lower}}^* = H_{\text{lower}}/H$	Filling mode (downdip)
E42	10	1.01	80.1	0.75	0.35	Simultaneous
E43	15	0.51	20.1	0.25	0.6	Sequential
E44	15	0.51	20.1	0.5	0.45	Simultaneous
E45	15	0.51	20.1	0.75	0.36	Simultaneous
E46	15	0.51	80.1	0.25	0.6	Sequential
E47	15	0.51	80.1	0.5	0.45	Simultaneous
E48	15	0.51	80.1	0.75	0.3	Simultaneous
E49[†]	15	1.01	20.1	0.125	0.7	–
E50	15	1.01	20.1	0.25	0.6	Simultaneous
E51[†]	15	1.01	20.1	0.32	0.55	–
E52[†]	15	1.01	20.1	0.38	0.51	–
E53	15	1.01	20.1	0.5	0.45	Simultaneous
E54	15	1.01	20.1	0.75	0.3	Simultaneous
E55	15	1.01	40.1	0.25	0.6	Simultaneous
E56	15	1.01	60.1	0.25	0.6	Simultaneous
E57[†]	15	1.01	50.1	0.25	0.6	–
E58	15	1.01	80.1	0.25	0.6	Sequential
E59	15	1.01	80.1	0.5	0.45	Simultaneous
E60	15	1.01	80.1	0.75	0.3	Simultaneous

[†] Experiment was deliberately terminated before an assessment of the filling mode could be ascertained.

B.2 Dye calibration procedure

The amount of dye to be mixed into the source fluid was determined from the methodology of Dong & Selvadurai (2006). Accordingly, correlations between the dye con-

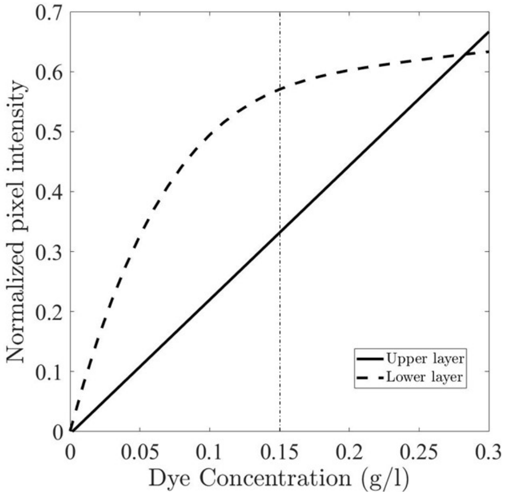

Figure B1: Dye calibration curves.

centration and normalized pixel intensity were obtained then plotted as in figure B1. Two separate calibration curves, one corresponding to the upper layer and other to the lower layer, were generated. Such a duplication is necessary because the two layers are comprised of glass beads of different diameters. As such, the layers do not transmit the same fraction of (background) light with the lower layer appearing darker than the upper layer, c.f. figure 3.1 b. Calibration curves such as those shown in figure B1 were obtained by completely filling the heterogeneous porous medium with (fresh) water of known dye concentration then capturing images using the Canon Rebel EOS T2i 18.0 PM camera. Multiple images were collected and the dye concentration varied from 0 to 0.3 g/L. Images were then processed using MATLAB to obtain the calibration curves. We observe from figure B1 that, due to the smaller permeability of the lower layer, the pixel intensity saturates comparatively quickly. Therefore, the dye concentration used in all of our experiments was set by the lower layer calibration curve, which demanded, in turn, that we limit the dye concentration to 0.15 g/L.

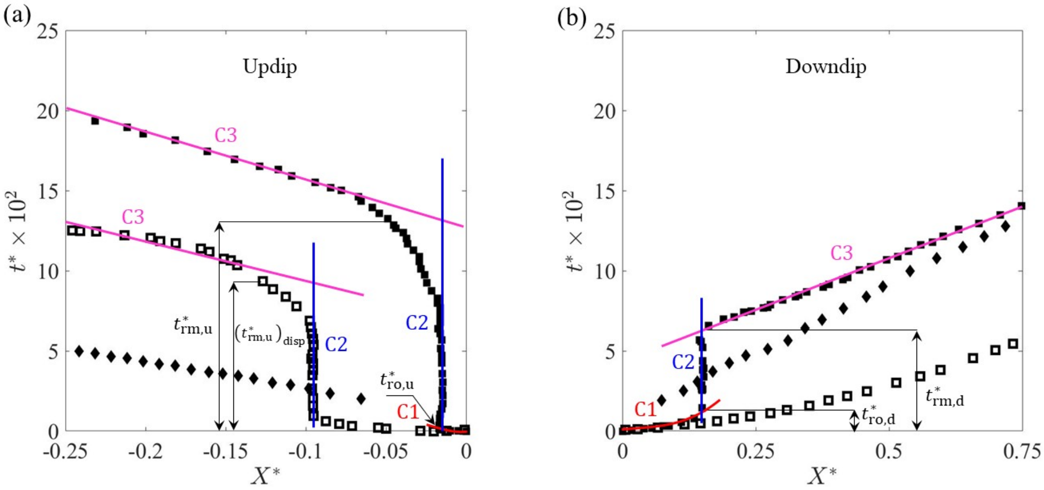

Figure B2: [Color] Method to determine, for the primary gravity currents, the time to runout, $t^*_{\rm ro}$, and the time for remobilization, $t^*_{\rm rm}$. Panels (a) and (b) respectively consider the up- and downdip sides. C1, C2 and C3 indicate curve fits for data points corresponding to different stages of motion, i.e. initial propagation, runout and remobilization. C1 is a third-degree polynomial, whereas for C2 and C3 the fitted curve is a first-degree polynomial.

B.3 Method for determining $t^*_{\rm ro}$ and $t^*_{\rm rm}$

To demonstrate the method for identifying the time to runout and the time to remobilization, we consider the downdip propagation of the primary gravity current for the case illustrated in figures 3.5 a,b. The evolution of the nose is divided into three time periods, which are curve-fitted by polynomial curves C1, C2 and C3 in figure B2. The point of intersection of C1 with C2 specifies the time to runout. Conversely, the point of intersection of C2 and C3 gives the time for remobilization.

B.4 Method for identifying simultaneous vs. sequential filling

Consider figure B3, whose panels a and b show snapshot images of experiments E19 and E28, respectively. In both cases $\theta = 5^\circ$, $Q_s = 1.01 \pm 0.02\,\mathrm{cm^3/s}$ and the plume nozzle is located at $X^*_s = 0.25$. However, in figure B3 a, $g'_s = 20.1 \pm 0.9\,\mathrm{cm/s^2}$ and the filling mode is simultaneous. By contrast, in figure B3 b, $g_s' = 80.1 \pm 0.9\,\mathrm{cm/s}^2$ and the filling mode is sequential. In making these assessments, reference is made to the surface plots of figures B3 c,d. These surface plots are generated by stacking in the vertical coordinate, $Z^* = Z/H$, contour lines derived from a horizontal time series analysis that follows from the procedure outlined in section 3.3.3. The surfaces therefore indicate, for prescribed X^* and Z^*, the moment in time when the pixel intensity first obtains a nontrivial value. This is, of course, the same instant when discharged plume/contaminated fluid is first detected at the location in question. The surfaces span the entire depth of the porous medium i.e. they draw data from the upper and lower layers. However, the surfaces pertain only to the downdip side of the nozzle. Analogue surface plots corresponding to the updip side are straightforward to construct but are not shown here. For illustrative purposes, it is also helpful to consider the shape of some of the contour lines that constitute the surfaces of figures B3 c,d. To this end, figures B3 e,f correspond to figures B3 c,d, respectively. In both line plots, data points falling on contour lines corresponding to $0.005 \le Z^* \le 0.3$ lie completely within the lower layer. Data points falling on the contour line labelled ($Z^* =$) 0.4 span both the upper and lower layers. Finally, data points falling on the contour line labelled ($Z^* =$) 0.99 lie completely within the upper layer. In either of figures B3 e,f, and except for the curve labelled ($Z^* =$) 0.99, the general trend of each curve is increasing. However, and as we explain below, it is the rate of increase between those curves labelled e.g. as ($Z^* =$) 0.005 and ($Z^* =$) 0.4 that is especially significant when distinguishing between simultaneous vs. sequential filling.

When $g_s' = 20.1 \pm 0.9\,\mathrm{cm/s}^2$, the snapshot of figure B3 a confirms that, on the downdip side, the upper layer begins to fill with dispersed fluid before the lower layer. This behavior is more clearly illustrated in figure B3 c, whose surface exhibits a vertical dip (highlighted by the vertical arrow) just below the permeability jump and for sufficiently large X^*. The dip reflects the fact that dispersed fluid from the primary gravity current reaches the sidewall boundary at relatively early times.

Thereafter, the dispersed fluid in question either drains (slowly) into the lower layer or else accumulates in a steadily thickening layer at the base of the upper layer. By contrast, the secondary gravity current forms later and so the base of the lower layer in the neighborhood of $X^* = 0.75$ begins filling with contaminated fluid only after the upper layer is, in effect, completely-filled. This latter conclusion is supported by figure B3 e. Contrasting the curves labelled 0.005 and 0.99 in the limit of large X^*, we note that contaminated fluid is observed in the neighborhood of the top of the box at an earlier time than contaminated fluid is noted in the neighborhood of the bottom of the box. For those pixels along $Z^* = 0.005$, filling is associated with the horizontal advection of the secondary gravity current, thus the nearly linear increase of the curve labelled 0.005 in figure B3 e. Such linear behavior disappears when $Z^* = 0.25$ or 0.3, because at these larger elevations, the intrusion of contaminated fluid stems from the combination of the secondary gravity current and basal draining from the overlying primary gravity current. In contrast to figure B3 a, figure B3 b considers $g_s' = 80.1 \pm 0.9\,\mathrm{cm/s^2}$ and shows an example of sequential filling. The right hand side edge of the surface from figure B3 d corresponds to $X^* = 0.75$ and shows a monotone (and nearly linear) variation as highlighted by the long black arrow. In like fashion, the curves from figure B3 f show, for sufficiently large X^*, a progressive increase from small to intermediate to large values of Z^*.

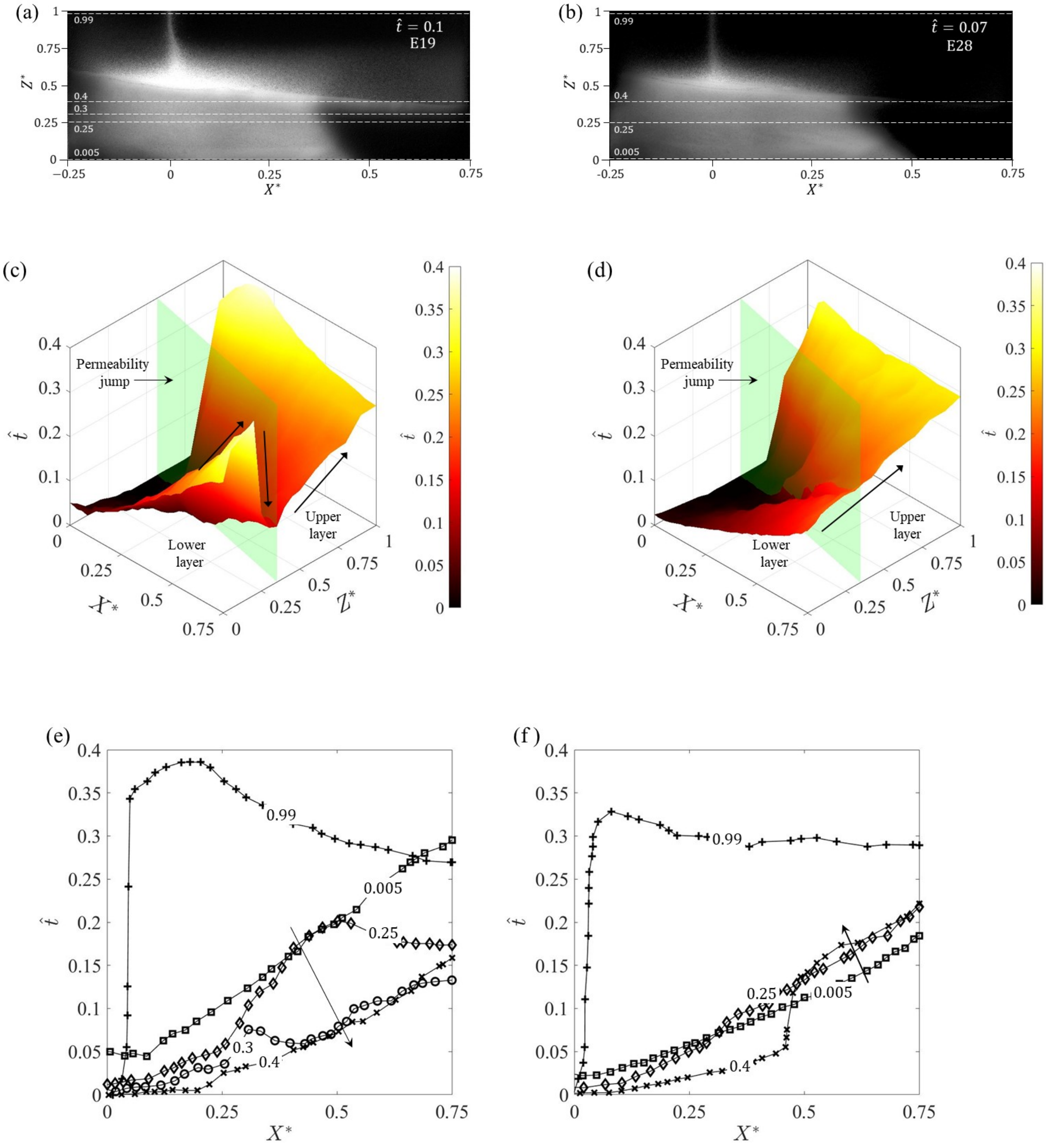

Figure B3: [Color] False-color snapshot images in (a) and (b), surface plots in (c) and (d), and line plots in (e) and (f), for simultaneous (left panels, $g_s' = 20.1 \pm 0.9\,\mathrm{cm/s^2}$) and sequential filling (right panels, $g_s' = 80.1 \pm 0.9\,\mathrm{cm/s^2}$). The vertical locations of the curves, i.e. $Z^* = 0.005$, 0.25, 0.3, 0.4 and 0.99, exhibited in (e) and (f) are indicated in the snapshot images (a) and (b) by the dashed horizontal lines. Also, the arrows in (e) and (f) point in the direction of increasing Z^*. In panels c and d, the position of the permeability jump is indicated by the vertical plane (green). Here $\theta = 5°$ and $Q_s = 1.01 \pm 0.02\,\mathrm{cm^3/s}$.

Appendix C: COMSOL simulation details

C.1 Random order of permeabilities: $k_1 > k_3 < k_2 > k_4 > k_5$

In Chapter 4, we investigated the flow pattern formed in a multi-layered porous media for layer configurations, starting from the source of injection, arranged in their decreasing order of permeabilities. In this appendix, we relax the assumption of layer configuration and consider a scenario in which low permeability layer exists on top of a higher permeability layer.

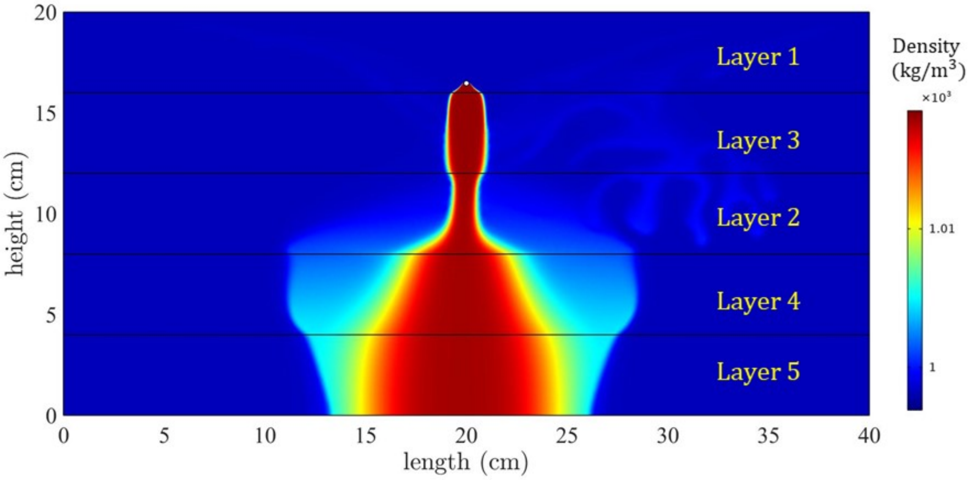

Figure C1: [Color] As in figure 4.7 d but with Layers 2 and 3 interchanged.

Whereas figure 4.7 d considers a case in which the layer permeabilities follow a descending order with $k_1 > k_2 > k_3 > k_4 > k_5$, figure C1 examines a situation in which two of the intermediate layers are interchanged. The numerical simulation in question allows us to explore a situation in which dense contaminated fluid, originating from the source, drains into a lower layer of higher, rather than lower, permeability. We observe from figure C1 that there is no outflow of contaminated fluid along the permeability jump between Layers 2 and 3. Rather all of the contaminated fluid drains straightaway into Layer 2. In contrast to the observations in figures 4.7-4.9 where the width of the draining fluid continuously increases in each successive layer, figure C1 indicates that the fluid draining into Layer 2 experiences a decrease in its width. This is because the fluid enters from a layer of higher resistance (Layer 3) into the layer of lower resistance (Layer 2), consequently, the fluid experiences an increase in its velocity. And in order to satisfy the conservation of mass, the overall width of the fluid has to contract. In contrast, our theoretical model assumes that the fluid always drains from a more permeable layer into a less permeable layer, and in such cases, the fluid experiences a flow resistance due to which the draining velocity decreases. Therefore, we treat the flow exhibited in figure C1 as a special case and do not compare with our theory predictions.

C.2 Method for determining runouts in COMSOL simulation

To demonstrate the method for determining runout lengths along a permeability jump, we consider, for illustrative purposes, the permeability jump corresponding to case shown in figure 4.7 a. The variation in density is plotted vs. the horizontal coordinate in figure C2. The data in question are fit with a variety of straight lines, which we label as C1, C2, C3, C4 and C5. Of particular interest are the points of intersection of adjacent lines, i.e. the intersections between the line pairs C1/C2 and C2/C3. We define as the left runout distance the midpoint between these two intersections points. A similar procedure is applied to the right where the consider the points of intersection of the line pairs C3/C4 and C4/C5. Following this approach (and also extending it to cases where $\theta > 0$) gives an objective and accurate means of estimating runout lengths along any given permeability jump.

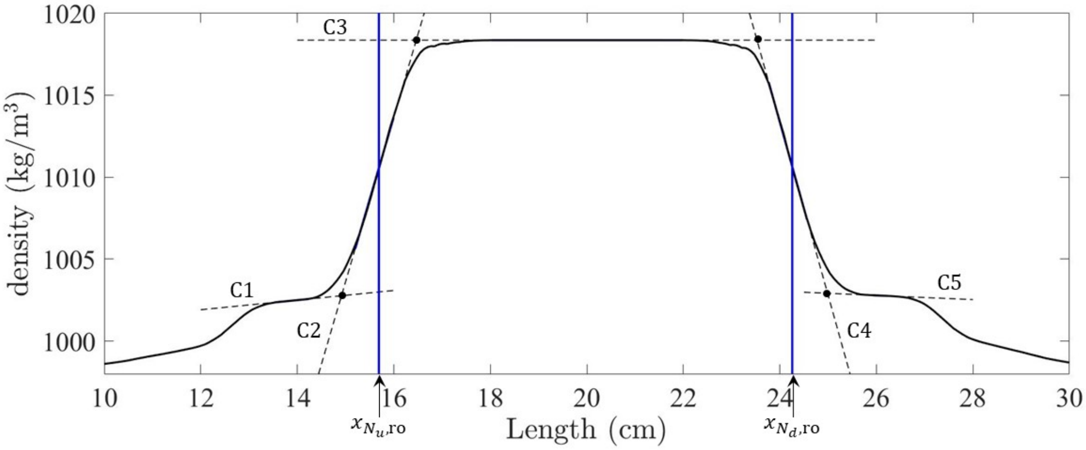

Figure C2: Variation of density along a (horizontal) permeability jump. The linear curve fits, C1, C2, C3, C4 and C5, are shown as dashed lines. The vertical lines in blue indicate the runout distances.